

**DOT/FAA/TC-12/43**

Federal Aviation Administration  
William J. Hughes Technical Center  
Aviation Research Division  
Atlantic City International Airport  
New Jersey 08405

# **Crash Simulation of Transport Aircraft for Predicting Fuel Release**

## **First Phase—Simulation of the Lockheed Constellation Model L-1649 Full-Scale Crash Test**

October 2012

Final Report

This document is available to the U.S. public through the National Technical Information Services (NTIS), Springfield, Virginia 22161.

This document is also available from the Federal Aviation Administration William J. Hughes Technical Center at [actlibrary.tc.faa.gov](http://actlibrary.tc.faa.gov)



U.S. Department of Transportation  
**Federal Aviation Administration**

## NOTICE

This document is disseminated under the sponsorship of the U.S. Department of Transportation in the interest of information exchange. The United States Government assumes no liability for the contents or use thereof. The United States Government does not endorse products or manufacturers. Trade or manufacturer's names appear herein solely because they are considered essential to the objective of this report. The findings and conclusions in this report are those of the author(s) and do not necessarily represent the views of the funding agency. This document does not constitute FAA policy. Consult the FAA sponsoring organization listed on the Technical Documentation page as to its use.

This report is available at the Federal Aviation Administration William J. Hughes Technical Center's Full-Text Technical Reports page: [actlibrary.tc.faa.gov](http://actlibrary.tc.faa.gov) in Adobe Acrobat portable document format (PDF).

1. Report No. DOT/FAA/TC-12/43		2. Government Accession No.		3. Recipient's Catalog No.	
4. Title and Subtitle CRASH SIMULATION OF TRANSPORT AIRCRAFT FOR PREDICTING FUEL RELEASE FIRST PHASE—SIMULATION OF THE LOCKHEED CONSTELLATION MODEL L-1649 FULL-SCALE CRASH TEST				5. Report Date October 2012	
				6. Performing Organization Code	
7. Author(s) R.T. Bocchieri, R.M. MacNeill, C.N. Northrup, and D.S. Dierdorf				8. Performing Organization Report No.	
9. Performing Organization Name and Address Applied Research Associates, Inc. 2672 Bayshore Parkway, Suite 1035 Mountain View, CA 94043				10. Work Unit No. (TRAIS)	
				11. Contract or Grant No. DTFACT-06-X-0007	
12. Sponsoring Agency Name and Address Federal Aviation Administration Airport Safety and Operations Division (AAS-300) 800 Independence Avenue SW Washington, DC 20591				13. Type of Report and Period Covered  Final Report	
				14. Sponsoring Agency Code AAS-300	
15. Supplementary Notes  The Federal Aviation Administration Airport and Aircraft Safety R&D Division COR was Keith Bagot.					
16. Abstract For nearly 40 years, the National Fire Protection Association, the Federal Aviation Administration, and the International Civil Aviation Organization have used mathematical models, such as the Theoretical Critical Area and Practical Critical Area (TCA/PCA) method, to determine Aircraft Rescue and Firefighting (ARFF) requirements at commercial airports throughout the world. These models used the length and width of the aircraft fuselage to determine a rectangular area in which extinguishing the fire was critical to safely evacuate passengers. They do not consider the plausible amount of fuel that could be released in survivable crash events.  There has been growing concern that the ARFF requirements may not be sufficient for modern aircraft designs that include larger fuel capacities and varied crashworthiness. This research program is being conducted to establish an alternative methodology for evaluating the quantity of fuel dispersed during various types of survivable aircraft accidents and ultimately to contribute to the development of an alternative to the TCA/PCA method. The approach is to simulate survivable crashes using high-fidelity nonlinear dynamic finite element analysis of these events with fuel explicitly modeled in the wing tanks. The simulated, time-dependent fuel distribution will serve as input to fire modeling efforts for determining ARFF requirements.  This research is being conducted in multiple phases. The first phase is a methodology validation phase in which a full-scale crash test of a Lockheed Constellation Model L-1649 is simulated. The objective of this phase was to demonstrate that this modeling approach can produce accurate results. Subsequent phases will implement the validated methodology for assessing fuel dispersal from two different transport aircraft.  This report describes the analysis methodologies and results of the first phase of the research program. The analyses successfully demonstrated that accurate predictions for fuel release in survivable accidents can be achieved by using high-fidelity nonlinear dynamic finite element analysis of these events. Overall, simulated and test results for the liquid released are in good agreement. Refinements of modeling methods to more accurately simulate full-scale crashes of modern transport aircraft for predicting fuel release were also determined.					
17. Key Words Aircraft crashworthiness, Firefighting, Aircraft rescue, Fuel dispersion, Finite element analysis			18. Distribution Statement This document is available to the U.S. public through the National Technical Information Service (NTIS), Springfield, Virginia 22161. This document is also available from the Federal Aviation Administration William J. Hughes Technical Center at <a href="http://actlibrary.tc.faa.gov">actlibrary.tc.faa.gov</a>		
19. Security Classif. (of this report) Unclassified		20. Security Classif. (of this page) Unclassified		21. No. of Pages 97	22. Price

## ACKNOWLEDGEMENTS

Support from Harold Robertson for providing the original Lockheed Constellation Model L-1649 crash tests high-speed films and the Lockheed Martin Legacy Aircraft Support Group for providing the Lockheed Constellation Model L-1649 airframe engineering design drawings are gratefully acknowledged.



## TABLE OF CONTENTS

	Page
EXECUTIVE SUMMARY	xi
1. INTRODUCTION	1
2. TECHNICAL APPROACH	2
2.1 First Phase: Methodology Validation Against Full-Scale Crash Tests	3
2.2 Subsequent Phases: Evaluate Fuel Dispersal for Modern Transport Aircraft	5
3. DEVELOPMENT OF FINITE ELEMENT MODELS	6
3.1 The L-1649 LS-DYNA Finite Element Model	6
3.2 Water and Gel Models	10
3.3 Material Constitutive Behavior	12
3.4 Connection Modeling	14
3.5 Modeling Embrittlement of Perforated Plates	16
3.6 Ground and Barrier Models	19
3.7 Contact Modeling	21
3.8 Model Evaluation	22
4. UNCERTAINTY ANALYSIS	22
5. CRASH SIMULATION	25
5.1 Comparison With Crash Test	28
5.2 Overall Comparison	28
5.3 Structural Damage	60
5.3.1 Liquid Release—Tank 1 (Outboard Port Tank)	66
5.3.2 Liquid Release—Tank 2 (Mid-Wing Port Tank)	66
5.3.3 Liquid Release—Tank 5 (Inboard Port Tank)	68
5.3.4 Liquid Release—Tank 6 (Inboard Starboard Tank)	69
5.3.5 Liquid Release—Tank 3 (Mid-Wing Starboard Tank)	71
5.3.6 Liquid Release—Tank 4 (Outboard Starboard Tank)	76
6. SUMMARY	80
7. REFERENCES	83

## LIST OF FIGURES

Figure		Page
1	Definition of Minimum Agent Quantity Calculation Variables	1
2	Plan View of L-1649 Crash Test Site	3
3	Fuel Spillage Occurring 2.24 Seconds After Impact With Main Gear Barriers	4
4	The L-1649 LS-DYNA Finite Element Model	7
5	Simplified Engine Model Attached to the Engine Nacelle	7
6	Accelerometer Wing Installations	8
7	Comparison of L-1649 and L-749 Aircraft	9
8	The L-1649 Wing Structural Model	9
9	Various Rib Type Models	10
10	Fuselage Structural Model	10
11	Modeled Distribution of Dyed Water and Gel in the Integral Wing Fuel Tanks	11
12	Engineering Stress-Strain Data for the Extruded and Sheet Aluminum Alloy in the L-1649	13
13	True-Stress-True-Plastic Strain Fits for the Extruded and Sheet Aluminum Alloy in the L-1649	14
14	The CPPR Experimental Results	16
15	Contact Softening Behavior Using the Maximum Stress Criterion (no softening) and Linear Softening	16
16	Unit Cell Model of a Plate With Uniformly Spaced Holes	18
17	Effective Stress-Strain of a Homogenized 1-in.-Square Element With a Hole Compared to the Base Material	19
18	Aerial View of the Crash Test Site	20
19	Ground and Barrier Model With Aircraft in its Initial Simulated Location	21
20	The L-1649 Deformation Under Gravity Loading	22
21	The L-1649 Model in its Initial State for Crash Simulation	26

22	Video Footage of Engine Impact With the Wing's Leading Edge at Tank 5	27
23	Crash Test Comparison of Telephone Pole Impacts (front view)—Time = 1.018 s	30
24	Crash Test Comparison of Telephone Pole Impacts (front view)—Time = 1.041 s	31
25	Crash Test Comparison of Telephone Pole Impacts (front view)—Time = 1.086 s	32
26	Crash Test Comparison of Telephone Pole Impacts (front view)—Time = 1.215 s	33
27	Crash Test Comparison of Telephone Pole Impacts (front view)—Time = 1.274 s	34
28	Crash Test Comparison of Telephone Pole Impacts (front view)—Time = 1.427 s	35
29	Crash Test Comparison of Telephone Pole Impacts (front view)—Time = 1.585 s	36
30	Crash Test Comparison of Telephone Pole Impacts (side view)—Time = 1.041 s	37
31	Crash Test Comparison of Telephone Pole Impacts (side view)—Time = 1.131 s	38
32	Crash Test Comparison of Telephone Pole Impacts (side view)—Time = 1.230 s	39
33	Crash Test Comparison of Telephone Pole Impacts (side view)—Time = 1.379 s	40
34	Crash Test Comparison of Telephone Pole Impacts (side view)—Time = 1.460 s	41
35	Crash Test Comparison (front view)—Time = 1.045 s	42
36	Crash Test Comparison (front view)—Time = 1.220 s	43
37	Crash Test Comparison (front view)—Time = 1.589 s	44
38	Crash Test Comparison (front view)—Time = 1.904 s	45
39	Crash Test Comparison (front view)—Time = 2.417 s	46
40	Crash Test Comparison (front view)—Time = 2.808 s	47
41	Comparison of the Velocity-Time History at the Aircraft's Center of Gravity	48
42	The L-1649 Final Resting State	49
43	Sketches of Fuel Spillage Documented From High-Speed Photography of the L-1649 Full-Scale Crash Test	51
44	Fuel Spillage—Time = 1.25 s (Runs 1-4)	52
45	Fuel Spillage—Time = 1.25 s (Runs 5-8)	53
46	Fuel Spillage—Time = 1.39 s (Runs 1-4)	54

47	Fuel Spillage—Time = 1.39 s (Runs 5-8)	55
48	Fuel Spillage—Time = 2.49 s (Runs 1-4)	56
49	Fuel Spillage—Time = 2.49 s (Runs 5-8)	57
50	Fuel Spillage—Time = 2.90 s (Runs 1-4)	58
51	Fuel Spillage—Time = 2.90 s (Runs 5-8)	59
52	The L-1649 Wreckage (aerial view)	60
53	The L-1649 Wreckage (rear view)	61
54	Main Effects Plot—Tank 2 Liquid Release at 1.79 s	68
55	Video Footage of Engine Impact With the Wing Leading Edge at Tank 5	69
56	Main Effects Plot—Tank 5 Liquid Release at end of 6° Slope	69
57	Main Effects Plot—Tank 6 Liquid Release at end of 6° Slope	70
58	Main Effects Plot—Tank 6 Liquid Release at end of 6° Slope, Including Release Into Tank 7	71
59	Main Effects Plot—Tank 3 Liquid Release at end of 6° Slope	72
60	Simulated Damage From Inboard Telephone Pole Impact—Time = 1.250 s (view of wing leading edge with engine removed from view)	73
61	Impact of Telephone Pole 1 With Tank 4 (Run 1)—the 6° Slope was Hidden From View	77
62	Impact of Telephone Pole 1 With Tank 4 (top view) at 1.10 s	78
63	Main Effects Plot—Tank 4 at 1.10 s	79
64	Main Effects Plot—Tank 4 at 1.30 s	79
65	Wing Tank Diagram	83

## LIST OF TABLES

Table		Page
1	Aircraft Incidents	2
2	Transport Aircraft Candidate Impact-Survivable Crash Scenarios	6
3	The L-1649 Component Weight Estimates	8
4	Fuel Tank Contents	11
5	Water and Gel Properties	12
6	Uncertainty Parameters in Modeling the L-1649 Crash Test	23
7	Fractional Factorial $2^{6-3}$ Experimental Design for the L-1649 Crash Test Analysis	23
8	The L-1649 Crash Test Sequence	25
9	Damage to Left (port) Wing—Runs 1-4	62
10	Damage to Left (port) Wing—Runs 5-8	63
11	Damage to Right (starboard) Wing—Runs 1-4	64
12	Damage to Right (starboard) Wing—Runs 5-8	65
13	Evolution of Damage to Tank 2	67
14	Evolution of Damage to Tank 3—Runs 1-4	74
15	Evolution of Damage to Tank 3—Runs 5-8	75

## LIST OF ACRONYMS

AFRL	Air Force Research Laboratory
ARFF	Aircraft Rescue and Firefighting
CPPR	Coach peel pop rivet
FAA	Federal Aviation Administration
ID	Identification
ILS	Instrument landing system
L	Length
MSD	Multiple Site Damage
NFPA	National Fire Protection Association
NLL	Net Ligament Loss
SPH	Smoothed Particle Hydrodynamics
TCA/PCA	Theoretical Critical Area/Practical Critical Area
W	Width
WTC	World Trade Center

## EXECUTIVE SUMMARY

For nearly 40 years, the National Fire Protection Association, the Federal Aviation Administration, and the International Civil Aviation Organization have used mathematical models, such as the Theoretical Critical Area and Practical Critical Area (TCA/PCA) method, to determine Aircraft Rescue and Firefighting (ARFF) requirements at commercial airports throughout the world. These models used the length and width of the aircraft fuselage to determine a rectangular area in which extinguishing the fire was critical to safely evacuate passengers. They do not consider the plausible amount of fuel that could be released in survivable crash events.

There has been growing concern that the ARFF requirements may not be sufficient for modern aircraft designs that include larger fuel capacities and varied crashworthiness. This research program is being conducted to establish an alternative methodology for evaluating the quantity of fuel dispersed during various types of survivable aircraft accidents and ultimately to contribute to the development of an alternative to the TCA/PCA method. The approach is to simulate survivable crashes using high-fidelity nonlinear dynamic finite element analysis of these events with fuel explicitly modeled in the wing tanks. The simulated, time-dependent fuel distribution will serve as input to fire modeling efforts for determining ARFF requirements and specifically to modify the existing methodology for determining the amount of fire-extinguishing agent required at an airport.

This research is being performed in multiple phases. The objective of the first phase, which is the subject of this report, was to validate the methodology, refine the modeling methods and demonstrating that accurate results are achievable. Subsequent phases will implement the validated methodology for assessing fuel dispersal from two different transport aircraft. The simulated, time-dependent fuel distribution from these phases will serve as input to the fire modeling efforts currently being conducted by the Air Force Research Laboratory and their subcontractors. The LS-DYNA finite element code is being used to simulate the aircraft incidents.

In the first phase, a well-controlled, full-scale crash test was simulated, which focused on determining fuel dispersal. The FAA conducted full-scale crash tests in 1964 using a Lockheed Constellation Model L-1649. These test programs were designed to simulate typical crash conditions during survivable takeoff and landing accidents in which dyed water was used in lieu of fuel so that the damage was due solely to the impact events.

As in performing simulations of any test,, there are uncertainties in the various input parameters in the model and in the experiment itself. It is important to understand and quantify the effect these uncertainties have on the predicted outcome. This will allow the development of bounds on the potential variability of the predicted result. In this case, the focus is on the fluid's release from the fuel tanks.

A fractional factorial experimental design was developed to perform screening of critical modeling parameters that affects the simulated performance of the L-1649 crash test and to bound the uncertainties on the conditions leading to the fuel release. Eight full-scale crash

simulations were performed by varying the model parameters. A detailed comparison of the crash test results and the simulation results was made.

First, an overall evaluation of the crash sequence was made by comparing high-speed photography taken from various angles, which focused on the quantity of liquid released. Then, the overall deceleration of the aircraft was compared with data taken at the aircraft's center of gravity via onboard instrumentation. Structural damage of the wings when the aircraft came to rest was compared. Finally, the liquid release from each tank was assessed by examining the significant parameters that affected the release.

The range of simulated responses bound that of the crash test in terms of overall aircraft motion, structural breakup of the wings, and release of liquid from the integral tanks. The most significant differences appear to occur due to the unknown severity of engine impact with the wings. Simulated responses varied from no damage to complete destruction of the wing at the point of impact, depending on the relative velocity of the engine. This appears to be an artifact of the simplistic engine modeling and is not realistic.

Another difference between the simulations and the crash test is that the simulated aircraft deceleration was slightly higher than the crash test, even for the lower bound for ground friction used. Interaction with the ground is important because the aircraft's deceleration affects the release of uncontained liquid from any compromised fuel tank. Also, the engines' interaction with the ground greatly affected how severe the resulting secondary engine impacts were on the wings.

Several key aspects of the aircraft modeling methodology were identified to improve the performance of the crash simulations planned for current transport aircraft in subsequent phases and to reduce the uncertainty in the results:

- Modeling the ductility of the connections in the wing structure is important to achieve a realistic response. The degree of ductility had a significant effect on liquid release for several fuel tanks in the L-1649 crash test. Reducing the uncertainty in this behavior will tighten the bounds on predicted fuel release in subsequent phases.
- Reducing the uncertainty in actual connection strength will tighten the bounds on predicted fuel release in subsequent phases.
- Incorporating structural embrittlement of the perforated plates from connections is essential in simulating realistic degrees of damage.
- Interaction of the aircraft and its components with the ground must be carefully modeled in subsequent work (e.g., pavement, soil, etc.). This will affect how the aircraft components are stripped away from the wing, the severity of the engine's impact with the wing, and the aircraft's deceleration.
- High-fidelity engine modeling is needed to achieve realistic impact responses when impacting against the wings and the ground.



# 1. INTRODUCTION.

For nearly 40 years, the National Fire Protection Association, the Federal Aviation Administration, and the International Civil Aviation Organization have used mathematical models, such as the Theoretical Critical Area and Practical Critical Area (TCA/PCA) method, to determine Aircraft Rescue and Firefighting (ARFF) requirements at commercial airports throughout the world. These models used the length and width of the aircraft fuselage to determine a rectangular area in which extinguishing the fire was critical to safely evacuate passengers. They do not consider the plausible amount of fuel that could be released in survivable crash events.

Currently, the required level of protection for fixed-wing aircraft is based on the fuselage length (L) and width (W), among other factors, as shown in figure 1. This methodology provides only for variation of fuselage length and width and fails to accommodate modern designs, such as multiple decks or differences in structural crashworthiness. For example, comparing the Airbus A380 to the Boeing 777-300ER yields roughly the same agent requirement (A380: L = 73 m and W = 7.15 m, 777-300ER: L = 73.9 m and W = 6.2 m). However, the A380 carries about 80% more fuel and 55% more passengers. The A380 clearly has the potential for requiring more extinguishing agent and more fire fighters in the initial response vehicles, but it is not clear what the required difference should be. Additional technological changes, including composite fuselages, will further increase the need for science- and engineering-based methodologies for determining fire protection requirements.\*

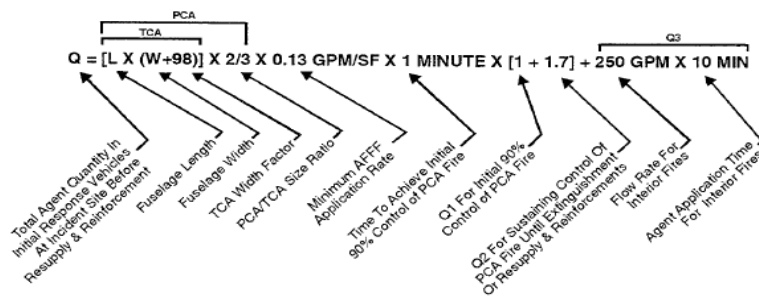


Figure 1. Definition of Minimum Agent Quantity Calculation Variables (U.S. Units) [1]

This research program is being conducted to establish an alternative methodology for evaluating the quantity of fuel dispersed during various types of survivable aircraft accidents and ultimately to contribute to the development of an alternative to the TCA/PCA method. The approach is to simulate survivable crashes using high-fidelity nonlinear dynamic finite element analysis of these events with fuel explicitly modeled in the wing tanks. The simulated, time-dependent fuel distribution will serve as input to fire modeling efforts for determining ARFF requirements and specifically to modify the existing methodology for determining the amount of fire-extinguishing agent required at an airport.

\*Press reports of the recent B-2 mishap on Guam indicate that 83,000 of AFFF solution were required to extinguish the post-crash fire. This is more than 10 times the amount of agent indicated by calculations based on NFPA 403 (including all replenishment requirements).

Although there are many plausible events that could lead to a fire, a review of aircraft accident reports of potentially survivable events indicate that there are generally three types of events:

- Fuel tank puncture from uncontained engine failure fragments.
- High-impact landing (hard landing).
- Ground collision with another structure.

These types of events occurred in the specific accidents listed in table 1, some of which are considered fire incident milestones. For the purpose of this research, efforts were focused on assessing incidents of these types when determining bounds for the quantity of fuel dispersed, the subsequent impact of fire on passenger survivability, and the requirement for crash rescue and firefighting capability.

Table 1. Aircraft Incidents

Incident Aircraft	Date and Accident Report	Location	Crash Details
Boeing 737-236	August 22, 1985 AAIB 8/88 <sup>†</sup>	Manchester Int. Airport, England	Engine fragment penetrated fuel panel.
Boeing 727-232	August 31, 1988 AAR-89-04 <sup>††</sup>	Dallas-Fort Worth Airport, TX	Struck instrument landing system (ILS) at takeoff.
Douglas DC-10	July 19, 1989 AAR-90-06 <sup>††</sup>	Sioux City, IA	Engine fragment destroyed all hydraulic systems. Right wing tip, main landing gear, and engine nacelle contacted runway at touchdown causing tumbling.
Boeing 737-300	February 1, 1991 AAR-91-08 <sup>††</sup>	Los Angeles International Airport, CA	Impacted a Fairchild Metro III turbo-prop on runway after touchdown.
Lockheed L-1011	July 30, 1992 AAR-93-04 <sup>††</sup>	John F. Kennedy International Airport, NY	Hard landing on right main landing gear causing failure of wing spar.

<sup>†</sup> UK Air Accidents Investigation Branch (AAIB) Aircraft Incident Report

<sup>††</sup> U.S. National Transportation Safety Board (NTSB) Aircraft Accident Report

## 2. TECHNICAL APPROACH.

Because of the unacceptable expense of performing full-scale crash tests of large transport aircraft, high-fidelity computational modeling of crash events are being performed to provide bounds on the quantity of fuel dispersed during various types of aircraft incidents. A similar approach was taken in reconstructing the World Trade Center (WTC) aircraft impact events of September 11, 2001 [2]. The simulated, time-dependent fuel distribution will serve as input to fire modeling efforts currently being conducted by the Air Force Research Laboratory (AFRL) and their subcontractors. The ARFF vehicle and agent requirements can then be defined using the experimental data developed in the Fire Extinguishing Effectiveness Test program at AFRL [3 and 4].

The LS-DYNA (Version 971) finite element code was used to perform simulations of aircraft incidents. LS-DYNA is a commercially available, nonlinear explicit finite element code for the dynamic analysis of structures. LS-DYNA has several unique capabilities for this project, such as the Smoothed Particle Hydrodynamics (SPH) algorithms that can be applied to the analyses of

fluid-structure interaction and large-scale fracture and fragmentation of structures. These capabilities are critical for the analyses of the fuel tank breakup and fuel dispersion. The presence of fuel in the integral wing tanks has a significant effect on both the impacted structure and on the wing structure breakup. This is clearly observed in the impact response of a Boeing 767 wing segment with the external panels of the WTC towers [2].

This research is being performed in multiple phases. The objective of the first phase, which is the subject of this report, was to validate the methodology by refining the modeling methods and demonstrating that accurate results are achievable. Subsequent phases will implement the validated methodology for assessing fuel dispersal from two different transport aircraft.

## 2.1 FIRST PHASE: METHODOLOGY VALIDATION AGAINST FULL-SCALE CRASH TESTS.

In the first phase, the modeling methodology was validated by comparing actual and simulated full-scale crash events. A simulation of real crash incidents was also considered. However, the difficulty with these incidents is that the initial conditions are not well known, the structural damage from impact is not understood well enough for a comparison (final damage from the subsequent fire typically leads to much greater damage), and there is limited detailed documentation of the event (such as from videographic sources or onboard accelerometers).

Fortunately, the FAA conducted full-scale crash tests in 1964 using commercial transport aircraft, specifically a Douglas Corporation DC-7 and a Lockheed Constellation Model L-1649 [5]. These were well-controlled, full-scale crash tests that focused on determining fuel dispersal. These test programs were designed to simulate typical crash conditions during survivable takeoff and landing accidents and collected considerable data on crash loads, accelerations, and fuel containment. Dyed water was used in lieu of fuel so that the damage was due solely to the impact events and not a subsequent fire. A plan view of the crash test site is shown in figure 2.

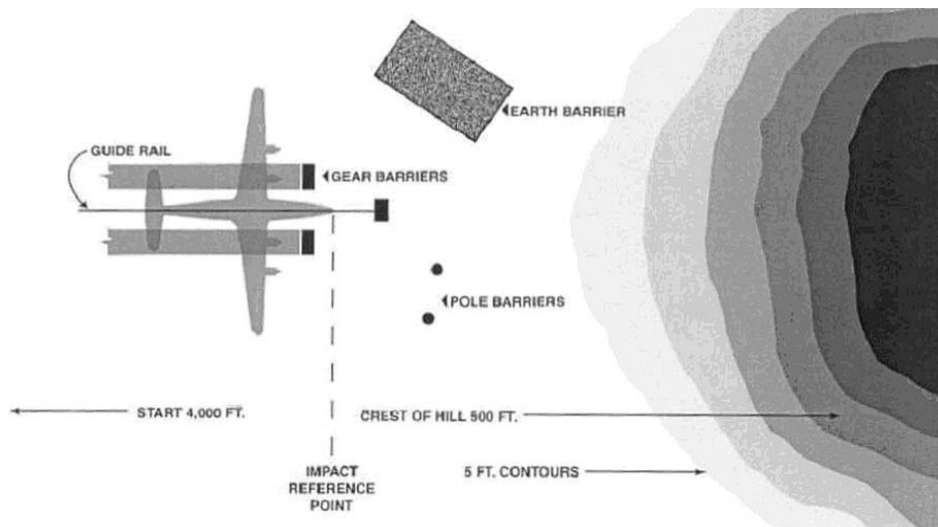


Figure 2. Plan View of L-1649 Crash Test Site [5]

The L-1649 test was the best choice for this research because it was made from higher-strength, low-elongation aluminum similar to modern aircraft. The DC-7 used an older design of relatively lower-strength, ductile skin. Accelerometer data, photographic and high-speed video documentation of the crash event, and the rate of fuel dispersal are available for comparison with the simulations. Modeling methodologies developed and validated in this phase will be used in subsequent phases to evaluate aircraft of interest.

Initial impacts removed the landing gear, causing the aircraft to be airborne. Once airborne, the left inboard engine broke loose and impacted the wing, the left wing struck an earthen barrier, and the right wing struck two vertical telephone poles. The resulting spill patterns of each wing tank were well documented in the test, as shown for example, in figure 3. The L-1649 had only integral wing fuel tanks and no bladder tanks.

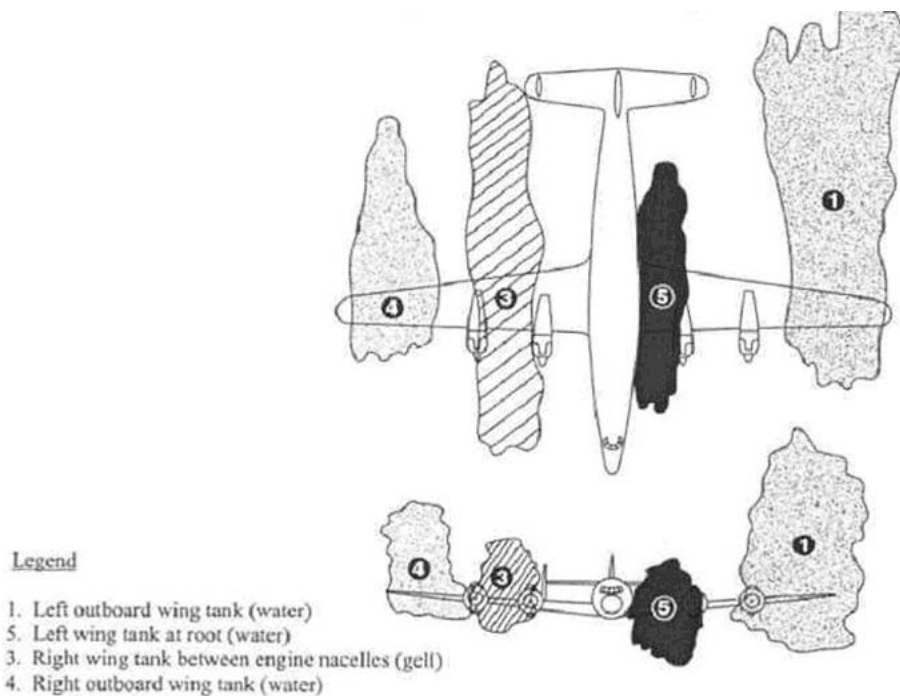


Figure 3. Fuel Spillage Occurring 2.24 Seconds After Impact With Main Gear Barriers [5]

An LS-DYNA finite element model of the L-1649 was constructed using information from structural repair manuals, Lockheed Martin design drawings, airline data, and existing three-dimensional geometric models available in electronic format. To minimize the cost of model development, and because the fuel is contained in the integral wing tanks, emphasis was focused on modeling the wing structures in detail. Using the Lagrangian method, the fuselage and empennage were modeled only in sufficient detail to capture their inertial and stiffness characteristics. Dyed water, representing the fuel, was explicitly modeled in the integral wing tanks using the SPH methodology. SPH is a mesh-free Lagrangian computational method especially useful for simulating fluid flows.

As in performing simulations of any test, there are uncertainties in the various input parameters in the model developed and in the experiment itself. It is important to understand and quantify

the effect of these uncertainties on the predicted outcome in order to develop bounds on the variability of the expected result. In this case, the main focus is on the fluid's release from the fuel tanks. An uncertainty analysis was performed using a fractional factorial experimental design to screen the critical modeling parameters and to bound the simulated fuel release. The results from this analysis will be used to guide the modeling approach used in the subsequent phases.

## 2.2 SUBSEQUENT PHASES: EVALUATE FUEL DISPERSAL FOR MODERN TRANSPORT AIRCRAFT.

The subsequent phases will implement the methodologies developed in the first phase for assessing fuel dispersal from various modern transport aircraft. The focus will be on determining the rate of fuel dispersal for three crash scenarios:

- Fuel tank puncture from an uncontained engine fragment.
- High-impact landing (hard landing).
- Ground collision with another structure.

The latter two scenarios are consistent with the impact-survivable accident scenarios developed by following the Special Aviation Fire and Explosion Reduction (SAFER) Advisory Committee recommendations for future crashworthiness research and development efforts, as shown in table 2 [6]. These scenarios were developed by examining in-depth transport accident data prior to 1980.

Analysis of hard landings should include both symmetric and single-gear landings to determine the greatest amount of fuel dispersal. Detailed models of the wing and landing gear structures will need to be developed for these analyses. The fuselage, empennage, and engines will be modeled only in sufficient detail to capture their inertial and stiffness characteristics to limit the cost of model development. The focus will be on the damage to the integral wing tanks. It is recommended that crash simulations that include the fuselage fuel tanks be performed as part of future work, but fuselage structures will need to be modeled in greater detail for such an analysis.

In the case of collisions with ground hazards, there are many potential hazards as outlined in table 2, including other aircraft. Two hazards will be selected in coordination with the FAA and AFRL. Impact with two very different types of hazards is recommended to examine the range of possible responses. Two examples might be impact with an instrument landing system, as shown in table 1, and impact between the wings of two comparable aircraft.

Analyses of hard landings and ground hazard impacts will be conducted by varying parameters that affect the amount of damage to the aircraft and, therefore, the rate of fuel dispersal. Such parameters include, among others, (1) aircraft speed, (2) ratio of descent rate to forward motion, (3) aircraft weight at time of landing, and (4) fuel load at landing. The variations in crash conditions will be limited to impact-survivable events and aircraft operational requirements, using the impact conditions shown in table 2 as a guide. Final bounds will be established in coordination with the FAA and AFRL. Worst-case rates of fuel dispersal within these bounds on flight conditions will be determined based on these analyses.

To evaluate an aircraft with composite wings, such as the Boeing 787, additional modeling methodologies and validation efforts should be part of a separate effort.

Table 2. Transport Aircraft Candidate Impact-Survivable Crash Scenarios [6]

Candidate Scenario	Operational Phase	Impact Conditions					
		Distance from Airport	Forward Velocity (kts)	Sink Rate	Airplane Configuration/ Impact Conditions	Terrain	Hazard
Ground to Ground (Overrun)	Takeoff abort/landing overrun	On runway or within 3000 ft. of end runway	60-100	< 5 fps	Gear extended. Symmetrical.	Runway Hard Ground	Ditches Trees Mounds Light Stanchions
Air to Ground (Hard Landing)	Landing-hard Landing-undershoot	On runway or within 300 ft. of threshold	126-160	> 5 fps < 12 fps	Gear extended. Symmetrical.	Runway Soft Ground	None
Air to Ground (Impact)	Final Approach	On runway or between outer marker and missed approach point	> 126 kts	> 12 fps	Gear extended & retracted. Symmetrical & Unsymmetrical Pitch 0° to 5° Roll 5° to 45° Yaw 0° to 10° Flight Path -4° to -7°	Hard Ground Hilly Rocky	Trees Poles Slopes Ravines Buildings

### 3. DEVELOPMENT OF FINITE ELEMENT MODELS.

#### 3.1 THE L-1649 LS-DYNA FINITE ELEMENT MODEL.

The L-1649 LS-DYNA finite element model was developed from various data sources. A digital surface geometry of the aircraft was acquired from Digimation [7]. The computational mesh was projected to this geometry to define the exterior geometry of the aircraft structure. Detailed information regarding the aircraft structure was determined from the aircraft Structural Repair Manual [8] and selected design drawings provided by the Lockheed Martin Legacy Aircraft Support Group. These reference materials contained information on material types, thicknesses, and connection types needed to construct the model. Engine manuals for the Wright Cyclone R-3350-988TC-18EA-2 turbo-compound engines were used to develop the rigid-body models for the engines with the correct mass and geometric characteristics [9 and 10].

The full L-1649 finite element model is shown in figure 4. The model contains 1.21 million shell elements with a nominal mesh size of 1-in. square in the wings and 2.2-in. square in the fuselage. The truss ribs contain 8235 beam elements for the truss members. All major structural components were included in the wing, nacelle, and mid-plane fuselage. Several components of the aircraft were modeled as rigid bodies as they were thought to not significantly contribute to the breakup of the wing fuel tanks aside from contributing to the overall crash dynamics. These include the empennage, the engines (figure 5) and the landing gear. This simplified model was used to provide the needed support during model checkout simulations under gravity loading.

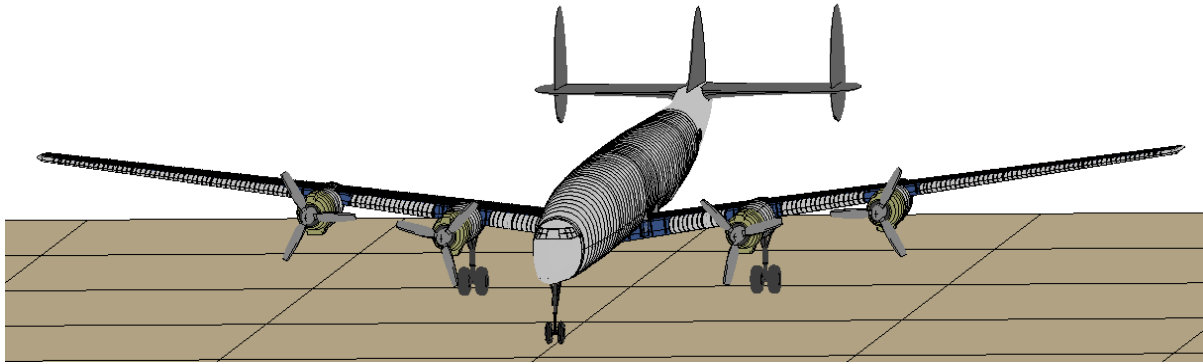


Figure 4. The L-1649 LS-DYNA Finite Element Model

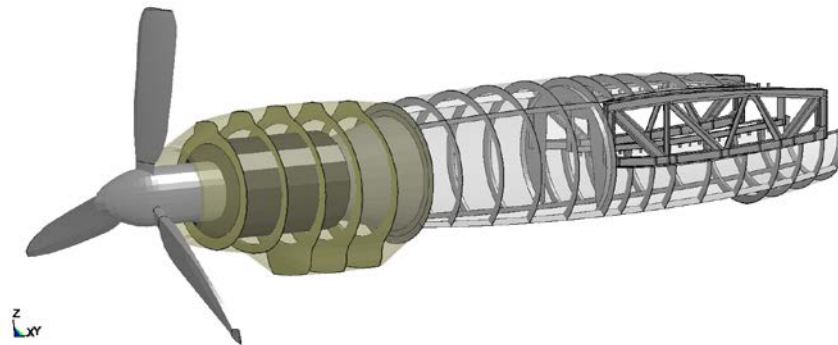


Figure 5. Simplified Engine Model Attached to the Engine Nacelle

Accelerometers were placed on the model wings at the locations shown in figure 6. This instrumentation was explicitly modeled so that the accelerometer data could be compared with the model response of each aircraft component during the crash.

Weights for each main component of the aircraft were estimated from known weight fractions of similar aircraft [11], as shown in table 3, as well as known weights for the engines, fuel onboard, and fixed equipment onboard. These estimates were used to scale each aircraft component in the model to the appropriate weight. This approach is needed since many nonstructural components of the aircraft (e.g., control wires, hydraulic lines, motors, and fasteners) were not explicitly modeled. The weight of these items were, therefore, added into the weight of the structure as is commonly done in developing finite element models of vehicles for crash analysis.

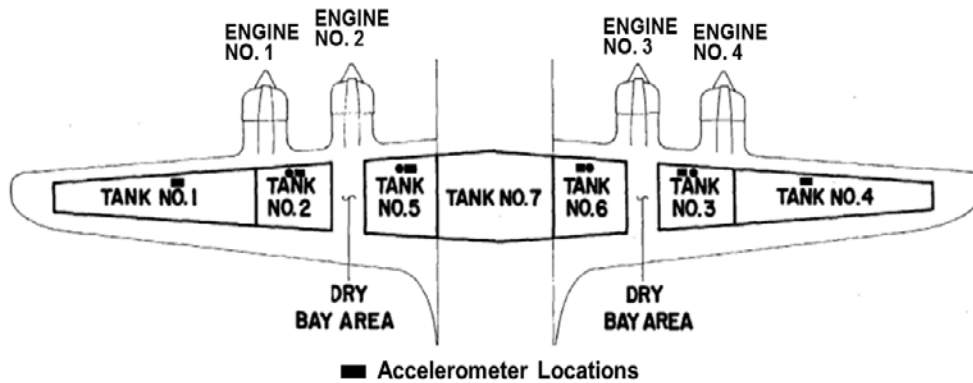
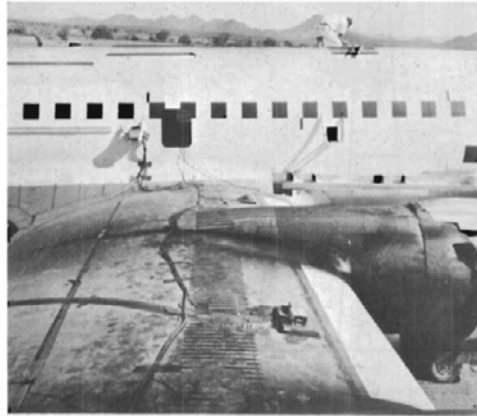


Figure 6. Accelerometer Wing Installations [5]

Table 3. The L-1649 Component Weight Estimates

Component	Lockheed C-69	Lockheed C-121A	Estimated L-1649	Estimated Weight (lb) L-1649
<b>Gross Weight (lb)</b>	82,000	132,800		159,131
	<b>Weight Fraction of Gross Weight</b>			
<b>Structure</b>	0.308	0.230	0.342	54,372
Wing Group	0.115	0.084	0.125	19,865
Empennage Group	0.025	0.016	0.024	3,740
Fuselage	0.083	0.064	0.096	15,226
Nacelle Group (w/o engines)	0.031	0.030	0.045	7,143
Landing Gear Group	0.055	0.036	0.053	8,399
<b>Power Plant</b>	0.191	0.118	0.127	20,210
Engines				14,980
Other PP				5,230
<b>Actual Fuel On Board</b>				48,900
<b>Fixed Equipment and Payload</b>				35,649



Geometric and component weight data were available for the Lockheed C-121A, the military version of the L-749. The L-1649 was developed from the L-749 design by extending the fuselage, expanding the wing area, and reinforcing the empennage. These aircraft are compared in figure 7. Masses for the L-1649 were scaled based on these modifications and an empty weight for the L-749 of 91,645 lb.

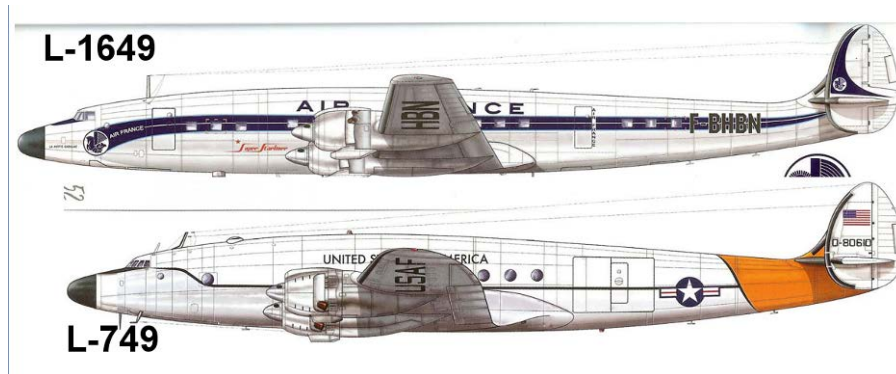


Figure 7. Comparison of L-1649 and L-749 Aircraft

Detailed finite element models were developed for the wing and parts of the fuselage structure. The highest fidelity was used for the wing ribs and spars and their attachments that make up the integral fuel tanks. These structures were made using shell elements with a typical element size of 1 in. The complete wing structural model is shown figure 8 and includes unique models for each type of rib, including three types of truss ribs and fuel tank ribs that contain the fuel in separate fuel compartments. Rib truss members were constructed using beam elements, as shown in figure 9. The skin of the wing, which is not shown in figure 8, was constructed with integral stiffening stringers. The skin panels were attached to the truss-type ribs using H-clips that are also shown in figure 9 along the top and bottom of the rib. The skin thickness was varied along the span as described in the design drawings.

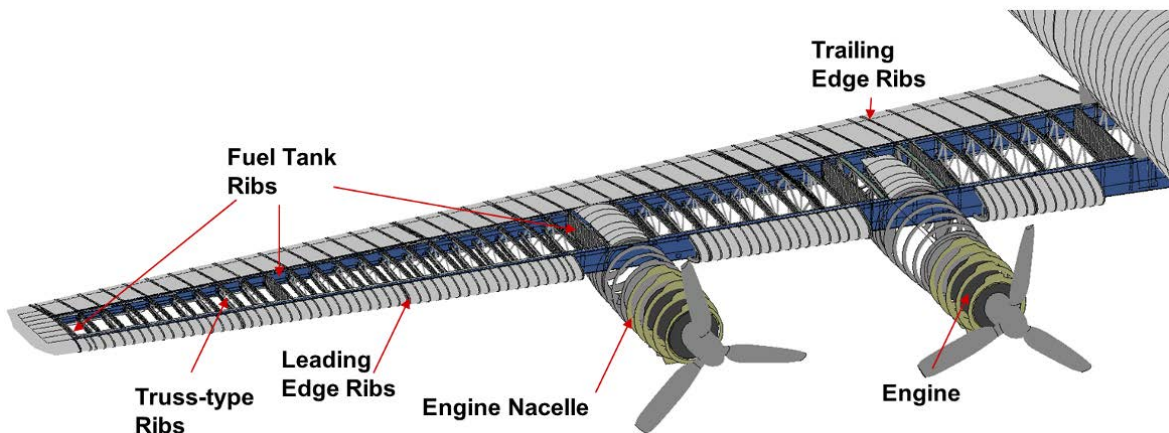


Figure 8. The L-1649 Wing Structural Model

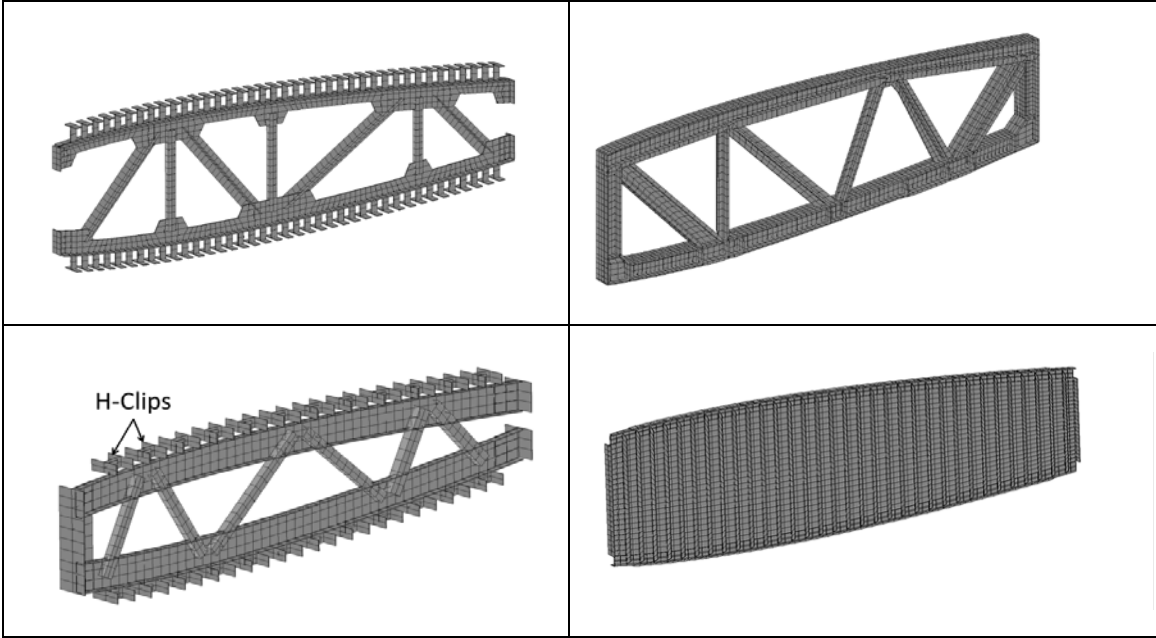


Figure 9. Various Rib Type Models

The mid-plane fuselage was modeled with a lower fidelity than the wing structure, but it included explicit models for the structural frames and flooring, as shown in figure 10. To reduce model size, an effective skin was used in place of the stringer-skin construction that is attached to the framing. The effective skin was given a thickness that produces that same bending stiffness as the stringer-skin construction in the longitudinal direction of the stringers. The density and yield stress was reduced to give the same weight per unit length and load-carrying capacity of the stringer-skin construction. A similar approach was used for the nose of the aircraft where just an effective skin was used to represent the complete stringer/frame/skin construction.

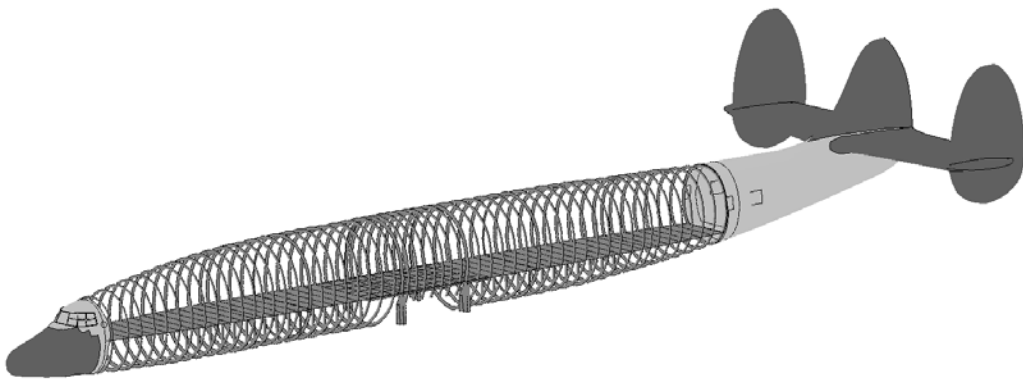


Figure 10. Fuselage Structural Model

### 3.2 WATER AND GEL MODELS.

The dyed water and gel used in lieu of fuel in the crash tests were explicitly modeled in the integral wing fuel tanks using 69,889 SPH particles with a spacing of 2.5 in., as shown in figure 11. The fluid weight placed in each tank is shown in table 4. The integral center fuel tank was

empty. Modeling these fluids with SPH particles captures important physical attributes of this event, including the fluid hydrodynamics and localized fluid pressurization of the structure due to impact loads. However, it neglects the fluids' interaction with the surrounding air once it is released from the tank. The SPH method was used despite this limitation since the main objective of this research was predicting fuel release from the tanks. To include the effect of aerodynamic drag on the fluid hydrodynamics and aerosolization would have required more computational time than was feasible for this program.

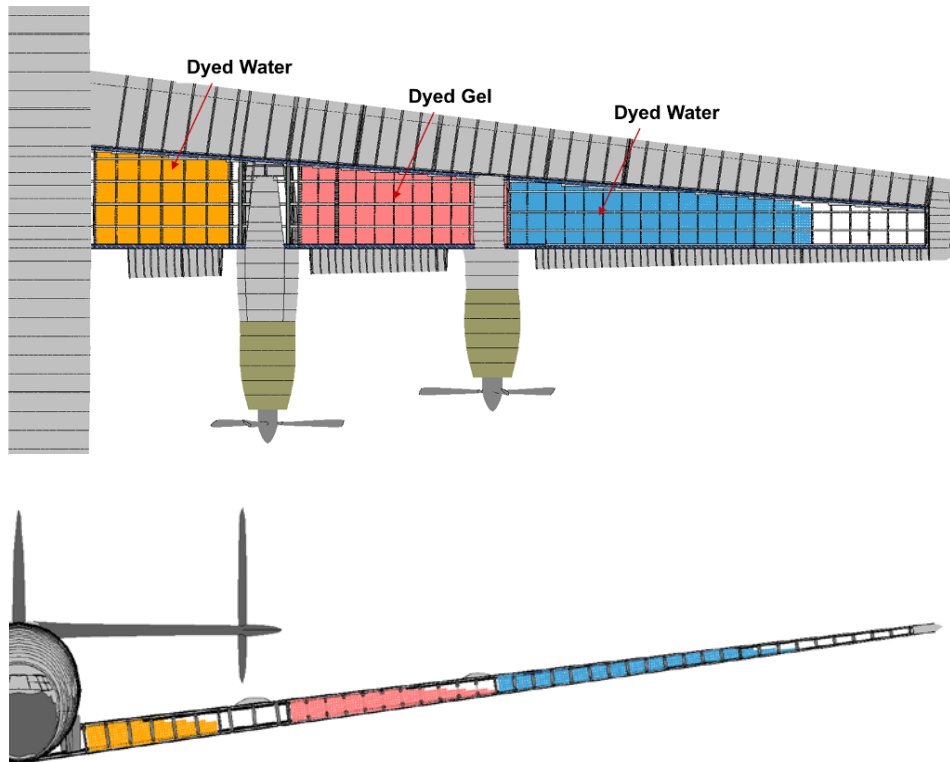


Figure 11. Modeled Distribution of Dyed Water and Gel in the Integral Wing Fuel Tanks

Table 4. Fuel Tank Contents

Tank No.	Contents	Weight (lb)
Left Side-Impacting Earth Barrier		
1	Water	8008
2	Gel	9102
5	Water	8217
Right Side-Impacting Telephone Poles		
4	Water	6256
3	Gel	9102
6	Water	8217

Contact was specified between the SPH particles and the spars, ribs, and skin that make up the integral wing tanks using the \*CONTACT\_NODES\_TO\_SURFACE algorithm. Contact with the internal ribs is important because the baffling effect of the truss-type ribs affects the fluid flow in each tank. Fluid levels in each tank were given an initial geometry equivalent to being level under gravity loading, as shown in figure 11.

Water and gel were modeled with the \*MAT\_NULL material model in LS-DYNA with the bulk linear modulus of 2200 MPa and defined with \*EOS\_LINEAR\_POLYNOMIAL. The density and viscosity for these fluids are given in table 5. The gel used in the tanks was comprised of a “gelled water mixture having approximately the consistency of applesauce” [5]. Using the Westco penetrometer test, the consistency of the gelled water mixture was measured at 50 mm. The gel’s density was calculated based on the known volume of water and gel in the tanks and their total weight.

Table 5. Water and Gel Properties

*MAT_NULL	
Water	
Density (kg/m <sup>3</sup> )	1000
Viscosity (kg/m-s)	8.94e-4
Gel	
Density (kg/m <sup>3</sup> )	1102
Viscosity (kg/m-s)	0.178

### 3.3 MATERIAL CONSTITUTIVE BEHAVIOR.

Material properties for the 2000 and 7000 series aluminum used in the L-1649 were derived from MIL-HDBK-5J [12] and the ASM International Atlas of Stress-Strain Curves [13]. The Piecewise Linear Plasticity (MAT 24) model in LS-DYNA was used to model material behavior for the extruded and sheet aluminum in the L-1649. This model requires a tabular nonlinear stress-strain curve. Engineering stress-strain data were collected from tensile tests of the aluminum alloys of interest, as shown in figure 12 [13]. Engineering stress is obtained by dividing the measured loads by the original cross-sectional area of the specimen. Similarly, engineering strain is obtained by dividing the change in the specimen gauge section length by the original length.

The constitutive model in the finite element analyses requires that the engineering data be converted to a true-stress and true-plastic strain. This conversion accounts for the changing cross section of the specimen as it was deformed. The specimen cross section changes (shrinks) significantly during the test, and the engineering stress does not yield the “true” stress in this cross section. Similarly, the engineering strain is not representative of the material behavior, especially when a general three-dimensional state of strain exists. As a result, the engineering stress decreases as some materials approach failure, implying a weakening of the material. In reality, the stress in the cross section is increasing due to the reduction in the cross-sectional area (i.e., necking).

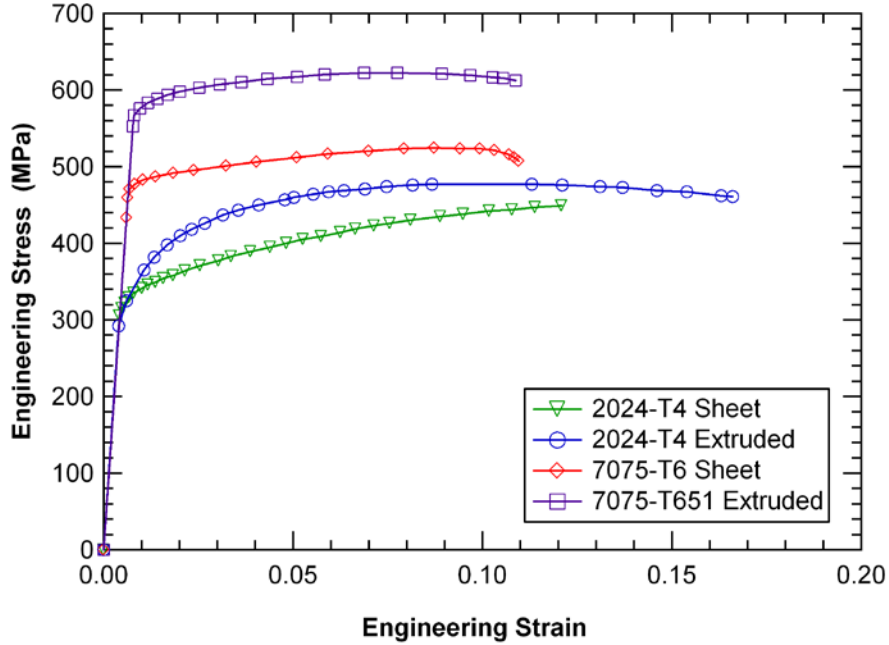


Figure 12. Engineering Stress-Strain Data for the Extruded and Sheet Aluminum Alloy in the L-1649 [13]

There are several different ways to measure stress and strain based on the coordinate system used. Some are based on material (Lagrangian) coordinates and some on spatial (Eulerian) coordinates. These give rise to terms such as “Green” and “Almansi” strain tensors. These are important in writing a computer code to solve large strain problems. An alternate approach is to define a “true” or “natural” stress and strain. The true stress is based on the load divided by the actual cross-sectional area of the specimen and is equal to the engineering stress multiplied by a term to correct for the change in cross section.

$$\sigma_T = \sigma_{eng} (1 + e) \quad (1)$$

where  $\sigma_T$  and  $\sigma_{eng}$  are the true and engineering stresses, respectively, and  $e$  is the engineering strain.

Prior to the onset of localization (necking), the natural or true strain,  $\varepsilon_T$ , is defined as

$$\varepsilon_T = \ln\left(\frac{l}{l_o}\right) = \ln(1 + e) \quad (2)$$

This definition comes about from defining the incremental true or “natural” strain as the current “change in length” divided by the current length, or

$$d\varepsilon_T = \frac{dl}{l} \quad (3)$$

This is in contrast with the definition of engineering strain that references the change in length,  $\Delta l$ , divided by the original length,  $l_0$ , or

$$e = \frac{\Delta l}{l_0} \quad (4)$$

After the onset of localization, the determination of the true strain in the necked region becomes more complex and requires measurement of the local neck geometry. True-plastic strain is calculated by subtracting the elastic strain.

The true-stress curves from the tests do not include a correction for the necking behavior. As a result, the correction is only valid up to the onset of necking at a true strain at the peak load shown in figure 12. The actual true-stress and true-strain curves for the material continue to strain harden throughout the loading if the effects of necking were corrected. An extrapolated true-stress curve that corrects for the effects of the necking behavior is used, resulting in the true-stress—true-plastic strain curves shown in figure 13. It is this extrapolated curve that is used in the material constitutive model.

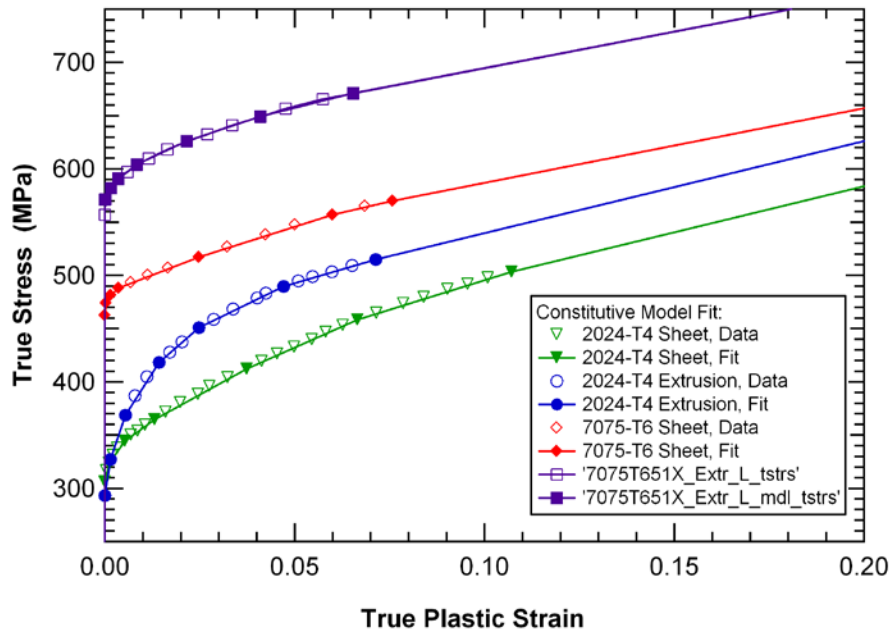


Figure 13. True-Stress-True-Plastic Strain Fits for the Extruded and Sheet Aluminum Alloy in the L-1649

### 3.4 CONNECTION MODELING.

Connections in the aircraft structure consisted of riveted and bolted joints. These were modeled using the \*CONTACT\_AUTOMATIC\_ONE\_WAY\_SURFACE\_TO\_SURFACE\_TIEBREAK contact algorithm, which behaves as a tied contact until certain criteria are met and as a sliding contact after failure. This approach distributes the load carried by the attachments across the

element areas prescribed in the contact algorithm. This algorithm has several options for prescribing under what conditions the tied contact fails. Refer to the LS-DYNA Keyword User's Manual for a more complete discussion on this algorithm [14].

Initial modeling implemented Option 2 of the tiebreak algorithm where a biaxial failure criterion was used. Failure is governed by the equation:

$$\left(\frac{\sigma_n}{\sigma_n^f}\right)^2 + \left(\frac{\sigma_s}{\sigma_s^f}\right)^2 \geq 1 \quad (5)$$

where  $\sigma_n$  and  $\sigma_s$  are the normal and shear stresses on an element, respectively. The  $\sigma^f$  are the corresponding magnitudes of the uniaxial normal and shear failure stresses. This functional form generally models the strength of riveted joints well [15 and 16], but displays very brittle failure behavior. Connections strengths were estimated by using the quasi-static normal and shear failure loads of the connections used in each joint of the structure, scaled by the number of fasteners used in each area. Quasi-static design values from MIL-HDBK-5J [12] were used for all connection types.

Preliminary simulations of the wing impacts with the telephone poles and the soil berm displayed widespread failure of many joint locations leading to an unrealistic amount of damage compared to the crash test. This is due to the brittle behavior of the tiebreak contact algorithm. These connections need to include joint ductility, which is consistent with the findings of other airframe structures modeling in crash applications [15].

These joints may display significant nonlinearity in their load-displacement response due to yielding of the fasteners themselves, local deformation of the adjoining metal sheets, and joint slippage [17]. Fastener deformation can contribute fractions of a millimeter to several millimeters of deformation [16 and 18]. Total deformation that includes the adjoining sheets largely depends on the joint configuration and can be in excess of 20 mm, as shown in figure 14 for coach peel pop rivet (CPPR) experiments in reference 19.

Modeling the detailed modes of damage growth displayed in these joints in a full aircraft analysis is not a tenable solution with current computational power. Instead, the \*CONTACT\_AUTOMATIC\_ONE\_WAY\_SURFACE\_TO\_SURFACE\_TIEBREAK algorithm with Option 11 was chosen to model the global load-displacement behavior of these joints. With this option, tiebreak is also active for nodes that are initially in contact. Failure stresses are defined in a similar fashion as for Option 2,

$$\left(\frac{\max(\sigma_n, 0)}{\sigma_n^f}\right)^2 + \left(\frac{\sigma_s}{\sigma_s^f(1 - \sin(\phi)\min(0, \sigma_n))}\right)^2 = 1 \quad (6)$$

where the  $\phi$  is the friction angle.

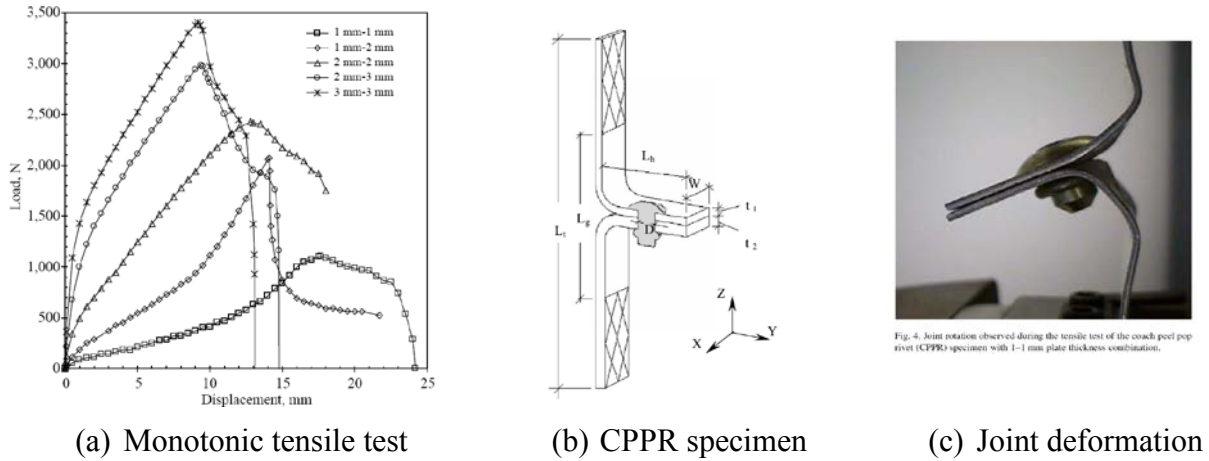


Figure 14. The CPPR Experimental Results [19]

Option 11 uses the Dyscoss Discrete Crack Model to represent the degradation in load-bearing capacity of the joint after the failure stress has been met [20]. After this failure stress is met, a damage variable, that is a linear function of the distance between points initially in contact, degrades the load capacity as shown in figure 15. After failure, this contact behaves as a surface-to-surface contact. A normal and shear energy release rate is specified to model the linear softening of the joint from the specified failure stress. These rates were calculated based on bounding the degree of displacement that occurs before the joint completely fails, as discussed in section 4.

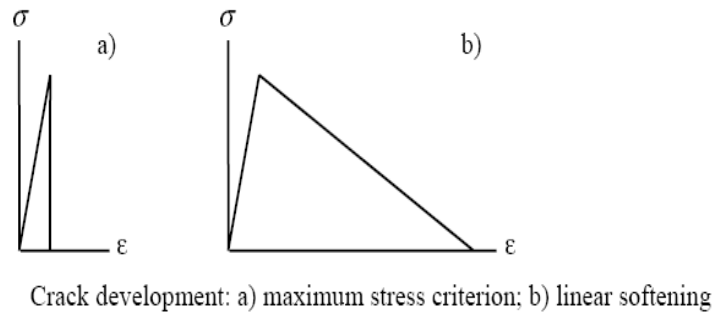


Figure 15. Contact Softening Behavior Using the (a) Maximum Stress Criterion (no softening) and (b) Linear Softening [20]

### 3.5 MODELING EMBRITTLEMENT OF PERFORATED PLATES.

Using fasteners can significantly embrittle and reduce the load capacity of attached plates due to the fastener holes in these plates. Riveted and bolted connections are typically designed with tightly spaced holes yielding high localized stresses between these holes. This effect can be made worse over time by the evolution of multiple site damage (MSD), that is fatigue cracks at the hole edges that is typical in aging aircraft.



Significant research has been conducted to determine the effect of MSD on the fatigue life and residual strength of aluminum plates [21]. Much of this research was focused on experimental testing and computational modeling of the plastic crack growth that occurs between these holes and its effect on residual strength and fatigue life. The numerical approaches developed for use in finite element codes are well-suited for this purpose in which small element sizes are feasible. Residual strength and loads for crack linkup work well for stiffened aluminum panels using a critical crack tip opening angle or maximum stress-intensity criteria [22-25]. They are not, however, as conducive with full-scale crash modeling due to element size restrictions.

Here, a simple approach has been used for estimating the residual strength of the aluminum plates in the aircraft structure that contain holes and potential MSD. The uncertainty in these behaviors were also quantified and used in performing the simulations to bound the variability in the simulated response in the crash event. The approach taken here is to homogenize the effect of uniformly distributed holes, with potential MSD, into the element nonlinear stress-strain behavior appropriate for the element size used in the model (approximately 1-in.-square shell elements). This is a similar approach to that proposed by Patronelli, et al. [26].

What is needed for this approach is an estimate for the stress-strain behavior to failure for a single element that represents material with a hole that is adjacent to other material with holes. The approach taken was to estimate the residual failure stress of the plate using simple analytical models and to perform finite element analyses of plates with holes to estimate the effective stress-strain response.

Cherry, et al. [27] evaluated various models for predicting the residual strength of unstiffened aluminum panels with holes and MSD, including the Net Ligament Loss (NLL) Criterion, the K-Apparent Criterion, Ligament Yield Criterion, and Average Displacement Criterion. The very simple NLL Criterion displayed good results for 2024-T3 thin aluminum plates with errors of less than 15%. This criterion estimates the residual strength by

$$P_{net} = \sigma_{ys} (W - 2a_2 - nd - 2nl)t \quad (7)$$

where

- $P_{net}$  = failure load
- $\sigma_{ys}$  = material yield stress (0.2% offset)
- $W$  = width of gauge section
- $a_2$  = half crack length of the central lead crack
- $n$  = number of holes
- $d$  = average diameter of holes
- $l$  = average half crack length of the MSD cracks
- $t$  = panel thickness

Because of the simplicity of applying this model to the many hole sizes and spacing in the aircraft structure, this method was adopted for estimating the residual strength.

Finite element analyses of plates with uniformly spaced holes were then performed for the various hole geometries used in the joints of the L-1649. A unit cell model of a plate with holes is shown in figure 16. The model shown has 0.125-in.-radius holes with a 1.0-in. hole spacing. Contours of effective plastic strain are shown in the figure at the failure load 15% higher than that predicted by the NLL Criterion. The average displacement and stress 0.5 in. above the hole centerline were extracted from the model and used to calculate an effective stress-strain response for a homogenized element of the same 1-in.-square dimension, as shown in figure 17.

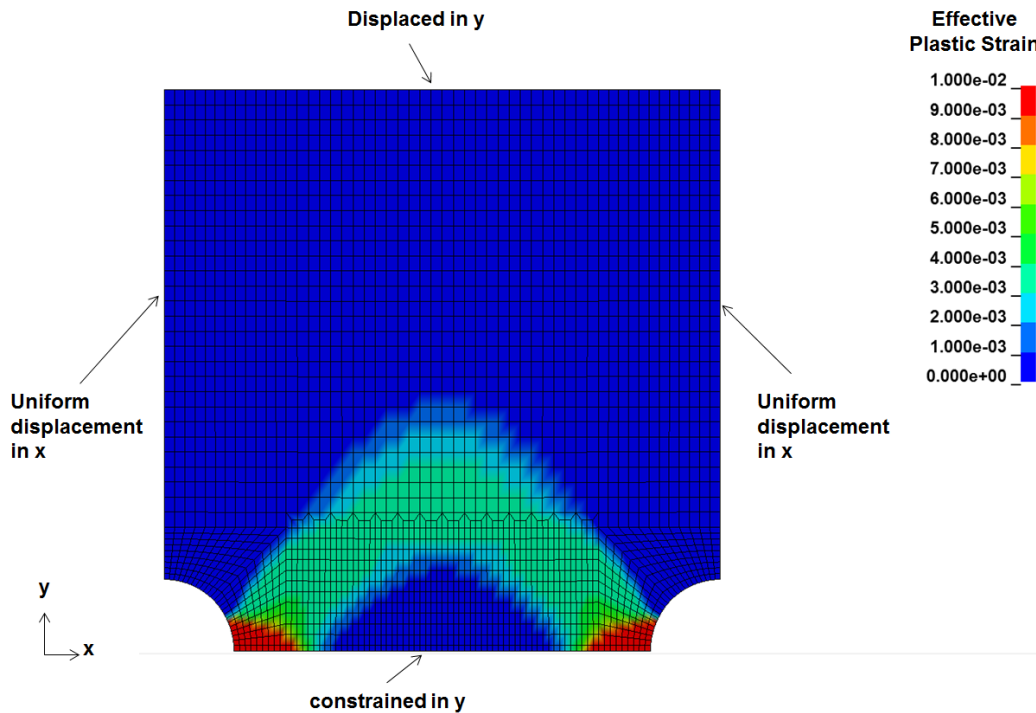


Figure 16. Unit Cell Model of a Plate With Uniformly Spaced Holes

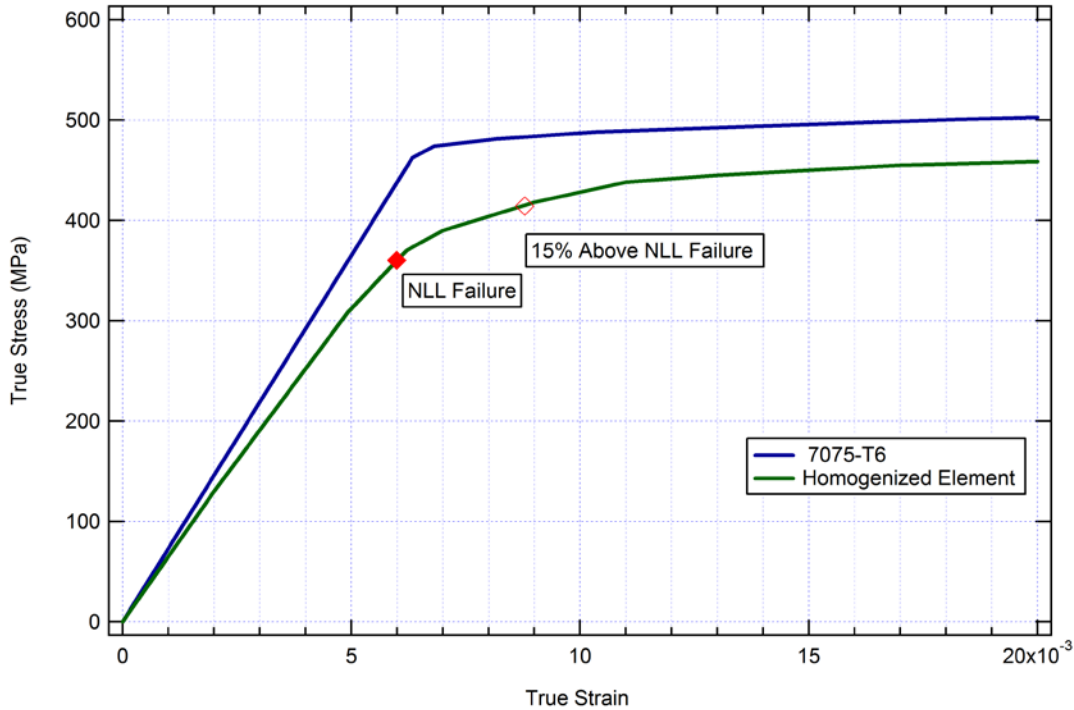


Figure 17. Effective Stress-Strain of a Homogenized 1-in.-Square Element With a Hole Compared to the Base Material

### 3.6 GROUND AND BARRIER MODELS.

Figure 18 shows an aerial view of the crash test site, including the location of the left-wing earthen barrier, the initial locations of the right-wing telephone pole barriers, the 6° slope, the 20° slope, as well as other details of the post-crash debris and fuel. Using photographs like this one, high-speed photography, and the written details in Reed, et al. [5], a model of the crash test site was created, as shown in figure 19. The ground, earthen barrier, and both slopes were modeled as rigid barriers with sliding contact defined between the aircraft and the soil obstacles.

The telephone pole barriers were modeled with single stress solid elements with a nominal dimension of 1-in. square in the impacted region of the telephone pole. These telephone poles were given a typical telephone pole dimension of 40 ft. tall and 10 in. in diameter. It was assumed that they were made of a wood commonly used for telephone poles, Southern Yellow Pine. Neither the type of wood nor the telephone pole dimensions were documented in the crash test report.

The LS-DYNA wood material model, \*MAT\_WOOD, was used to model the telephone poles' constitutive behavior. This model was created for the Federal Highway Administration for crash and impact applications. "This material model was developed specifically to predict the dynamic performance of wood components used in roadside safety structures when undergoing a collision by a motor vehicle." [28] Default values for Southern Yellow Pine contained in LS-DYNA were used in the simulations.

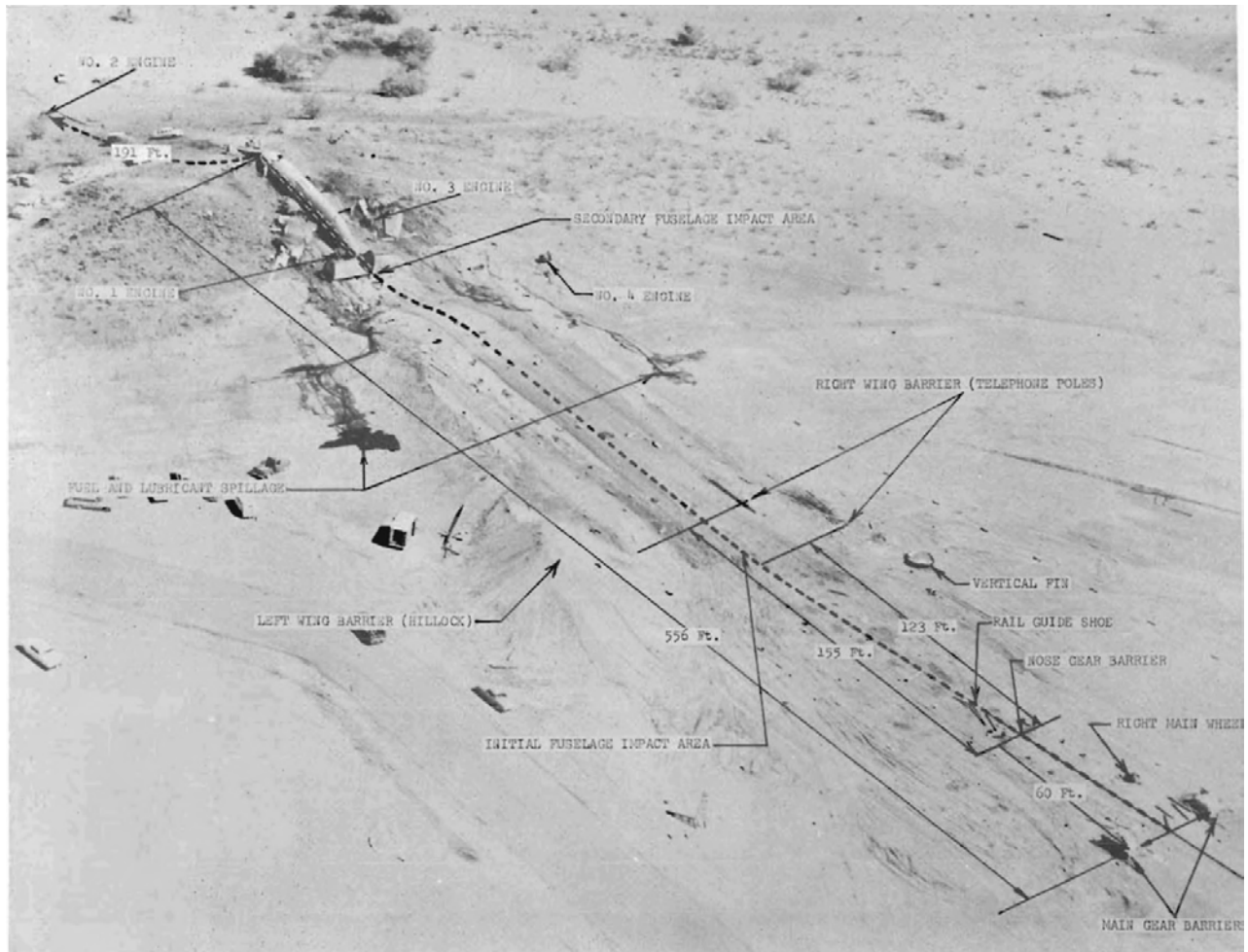


Figure 18. Aerial View of the Crash Test Site [5]

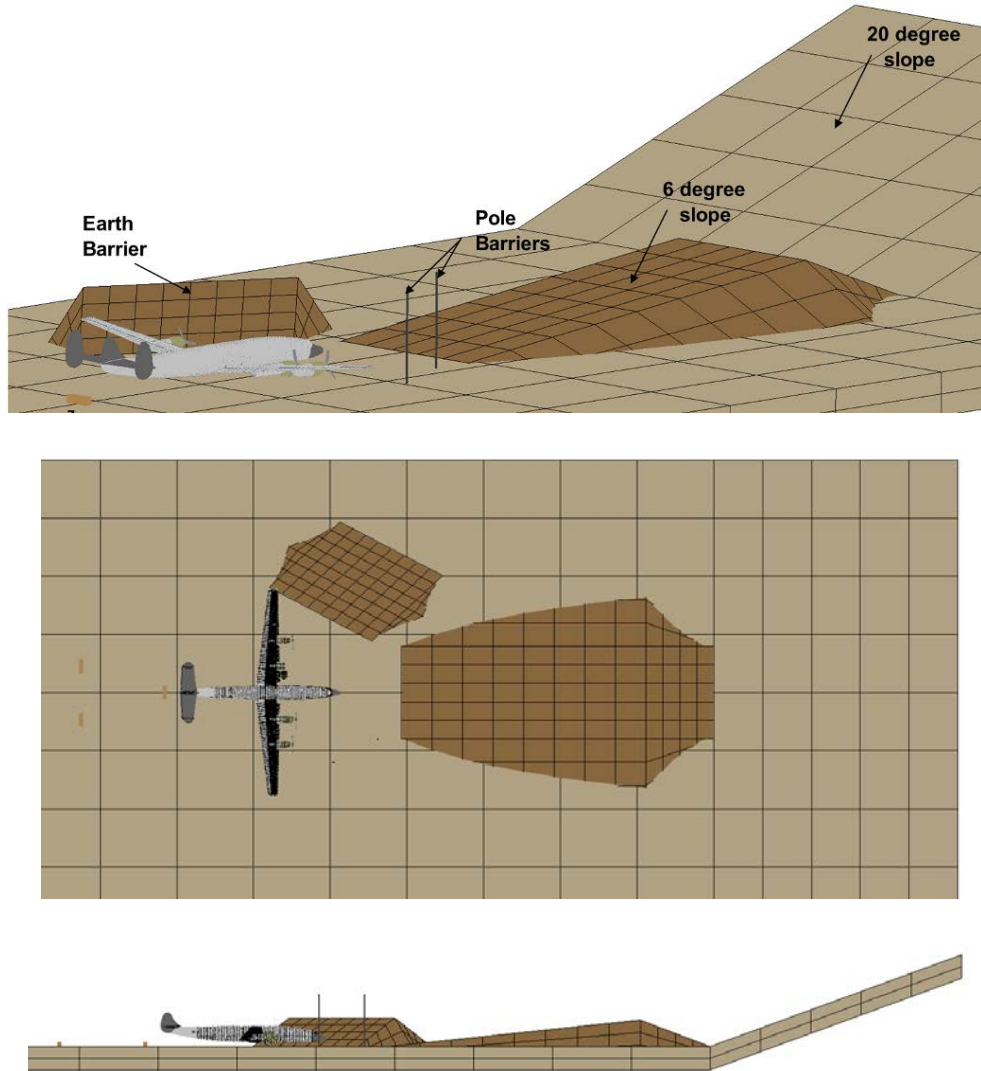


Figure 19. Ground and Barrier Model With Aircraft in its Initial Simulated Location

### 3.7 CONTACT MODELING.

Contact between components of the aircraft that were not part of a joint were defined using the `*CONTACT_AUTOMATIC_SINGLE_SURFACE` or the `*CONTACT_AUTOMATIC_SURFACE_TO_SURFACE` algorithm with a coefficient of friction of 1.0. The friction coefficient of aluminum to aluminum varies, depending on the surface condition in which dry surfaces can be as large as 1.35 and greasy surfaces 0.3 [29].

Contact between the aircraft and the ground and ground targets were defined with the `*CONTACT_AUTOMATIC_SURFACE_TO_SURFACE` algorithm. The coefficient of friction was varied as discussed in section 4. Contact between the wings and telephone poles were defined using the `*CONTACT_ERODING_SURFACE_TO_SURFACE` algorithm with a coefficient of friction of 0.4.

Water and gel contact with surrounding aircraft structures as well as the ground targets was defined using \*CONTACT\_NODES\_TO\_SURFACE\_ID. Contact with telephone pole targets were defined using \*CONTACT\_ERODING\_NODES\_TO\_SURFACE.

### 3.8 MODEL EVALUATION.

To perform an evaluation of the complete aircraft model and perform debugging, the aircraft was slowly initialized under gravity loading while on the ground. The L-1649 in the unloaded condition and under gravity loading, with the fuel tanks filled to the pretest condition, is shown in figure 20. Displacements under gravity loading are magnified by a factor of two in the figure. In the final model configuration, the model displayed no failure of connections or materials, as would be expected under gravity loading. Total vertical displacement of the wing tip was approximately 0.4 m.

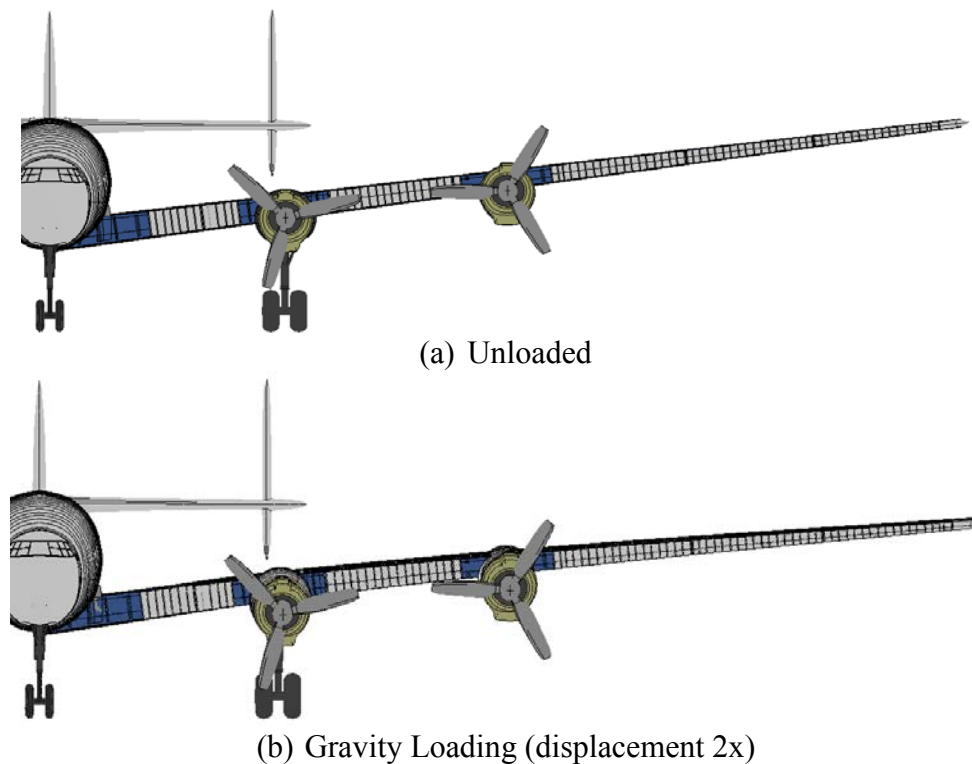


Figure 20. The L-1649 Deformation Under Gravity Loading

### 4. UNCERTAINTY ANALYSIS.

The objective of modeling the L-1649 crash test was to validate the modeling approaches used for full-scale crash simulation. As in performing any simulation, there are uncertainties in the various input parameters in the model developed and in the experiment itself. It is important to understand and quantify the effect of these uncertainties on the predicted outcome in order to develop bounds on the potential variability of the predicted result. In this case, the main focus is on the release of the fluid in the fuel tanks.

A fractional factorial experimental design [30] was developed to perform critical modeling parameter screenings that affect the simulated performance of the L-1649 crash test and to bound the variability in the simulated fuel release. The selected key modeling parameters are listed in table 6. Fractional factorial designs are two-level designs, run at high and low values for each variable. These designs require fewer than the usual  $2^k+1$  runs needed for a one at a time plus center point design. Variables are allowed to vary throughout the entire set of runs, each variable simultaneously in the presence of each other's variation. A  $2^{6-3}$  fractional factorial design was chosen for variable screening, as shown in table 7. The uncertainty factor identifications (ID) are listed across the top of the table with the run number on the left-hand side. Minimum and maximum cases from table 6 are shown by +1 and -1.

Table 6. Uncertainty Parameters in Modeling the L-1649 Crash Test

ID	Parameter	Low	High	
X1	Material Yield Stress	Allowable	125%	
X2	Material Failure Strain	7075-T6 Alum	3.4%	8.2%
		2024-T4 Alum	9.2%	12.4%
		Ebritt. Alum	NLL	115%
		17-7PH Steel	1.8%	2.2%
		AM350 Steel	3.0%	3.6%
X3	Connection Strength	Allowable	150%	
X4	Connection Ductility	2 mm	10 mm	
X5	Earth Barrier Location	+0.25 m	-0.25 m	
	Earth Barrier Angle (degrees)	-7.5	7.5	
	Pole Strength	low grade	structural grade	
X6	Ground Friction Coefficient	0.8	1.2	

Table 7. Fractional Factorial  $2^{6-3}$  Experimental Design for the L-1649 Crash Test Analysis

Parameter						
Run	X1	X2	X3	X4	X5	X6
1	-1	-1	-1	+1	+1	+1
2	+1	-1	-1	-1	-1	+1
3	-1	+1	-1	-1	+1	-1
4	+1	+1	-1	+1	-1	-1
5	-1	-1	+1	+1	-1	-1
6	+1	-1	+1	-1	+1	-1
7	-1	+1	+1	-1	-1	+1
8	+1	+1	+1	+1	+1	+1

The yield stress levels for both the 2024-T4 and 7075-T6 aluminum used in the aircraft structure were varied from the B-basis design allowable specified in MIL-HDBK-5J [11] to 125% of this value. By definition, the B-basis design value has a 90% probability with a 95% confidence that the yield stress will be at least this value. Since standard deviation of the data used to develop

these design allowables is not published, it was not possible to determine a mean or an upper value for the yield stress for these materials. The upper range of 125% of the allowable value is therefore an estimate. The nonlinear stress-strain curves from individual tests presented in section 3.3 were scaled to these yield values for the simulations.

Failure strains were estimated from published engineering failure strain data and scaled to account for element size. As part of the Federal Building and Fire Safety Investigation of the World Trade Center Disaster, simulations of aluminum wings impacting the WTC tower columns were used to investigate how to scale engineering failure strains based on element size [2]. Based on this study, a reduction of 20% is a good estimate for the 1-in. elements used in modeling the L-1649. So, for example, published data for 7075-T6 provides a B-basis allowable of 5% failure strain. The stress-strain data presented in section 3.3 shows failure at 11%. Scaling this number by 20% yield the 3.4% and 8.2% bounds presented in table 6.

Failure strains for the embrittled materials, discussed in section 3.5, were determined from the failure load determined from the NLL Criterion and the effective stress-strain response of a 1-in. element. Since this method tended to underestimate the experimental failure data by 10% to 15%, an upper bound of 115% of the NLL Criterion value was used.

There was considerable uncertainty accounted for in the connection strengths in the aircraft. For the lower bound, the failure load estimated from the B-basis design allowable connection strengths was used, as discussed in section 3.4. Since these values have, by definition, a 90% probability with a 95% confidence of being at least this value, using them as a lower bound is appropriate. In fact, MIL-HDBK-5J [11] states that the solid rivet joint values were calculated from the average ultimate test load divided by a factor of 1.15. Since the base materials used for the fasteners, aluminum and steel can show 25% to 30% variations in yield stress, it was estimated that the actual connections in the L-1649 could have been as much as 50% stronger.

Considerable uncertainty in the connection failure displacements were accounted for as well. As a lower bound, an estimate of 2 mm was used. As discussed in section 3.4, testing the fasteners themselves displayed roughly 1 mm of displacement at failure. This value was doubled to account for local deformation of the adjoining sheets that cannot be captured with the coarse 1-in. elements used in the model. An upper bound of 12 mm was estimated to account for the potential for large local deformation of the adjoining sheets.

The fifth modeling parameter (refer to table 6) accounted for uncertainty in the crash-test impact conditions. The low values represent a less significant impact condition than the high values. The low values have the wing impact the earthen barrier 0.5 m further outboard, the barrier turned away from the direction of travel by 15° and use the lower bound for the telephone pole strength. The barrier location and angle relative to the line of travel were estimated from photographs. The telephone pole strengths were taken from the defaults in the material model used for low grade and structural grade Southern Yellow Pine.

Friction between the aircraft components and the ground was varied between 0.8 and 1.2. The lower bound was estimated based on using a 35° to 40° friction angle for soil. The upper bound



was used to account for potential gouging into the soil, not modeled with the simple rigid surface used in the model that would increase the effective friction coefficient.

## 5. CRASH SIMULATION.

The general sequence and timing of the crash test sequence was derived from the test report [5], high-speed photography, and acceleration traces from the onboard instrumentation. This sequence is given in table 8. Note that the aircraft impacts the first telephone pole and the earthen barrier nearly simultaneously.

Table 8. The L-1649 Crash Test Sequence

Time (s)	Event
0.0	Impact with main landing gear barriers (as noted in test report [5]).
0.08	Impact with front landing gear barrier. The distance between the front and main gear barriers was 60 ft. However, the distance between the front landing gear and the main landing gear was 45.49 ft. Thus, the aircraft traveled 14.5 ft after impacting the main gear barriers and before hitting the front gear barrier; traveling at a speed of ~111.5 knots (as derived from the acceleration data).
1.0	Impact with earthen barrier (based on images and the acceleration peak at 0.8 s in the left-wing outboard vertical accelerometer).
1.0	Impact with telephone pole 1 (approximate time noted in the test report [5], referencing the acceleration data). Confirmed with acceleration trace data. These data stopped at 1.1 s. The telephone pole hit at an accelerometer position, indicating the time of impact. It took 0.01 s for the telephone pole to travel from the leading edge to the spar where the accelerometer was located.
1.05	Nose impact with the 6° slope (note the front of the aircraft is touching the ground). Estimated from report photographs (figure 19), cockpit acceleration traces (vertical acceleration started at ~1.08 s), and FAA video (stills captured from video).
1.18	Impact with telephone pole 2. The distance between the two telephone poles was 32 ft. Assuming the aircraft was traveling at 108 knots (from acceleration data), impact with telephone pole 2 occurred 0.18 s after impact with telephone pole 1.
3.0	Nose impact with the 20° slope (from high-speed photography).

The aircraft was initialized with a forward velocity of 112 knots (57.1 m/s) and a sink rate of 3.83 m/s, which was taken from high-speed photography at approximately 0.8 s after the main landing gear impacted the barriers. During the free-fall (the time between when the landing gear was removed to the time of first impact with the ground), the aircraft accelerated vertically at approximately 0.6 g. This indicated that there was some lift generated despite the aircraft control surfaces being set to generate minimum lift. A global vertical body force of 0.6 g was applied to the model during the free-fall stage of the simulation and increased to 1.0 g once the aircraft

impacted the ground. Under these conditions, the fuselage impacts the ground at approximately 4.9 m/s.

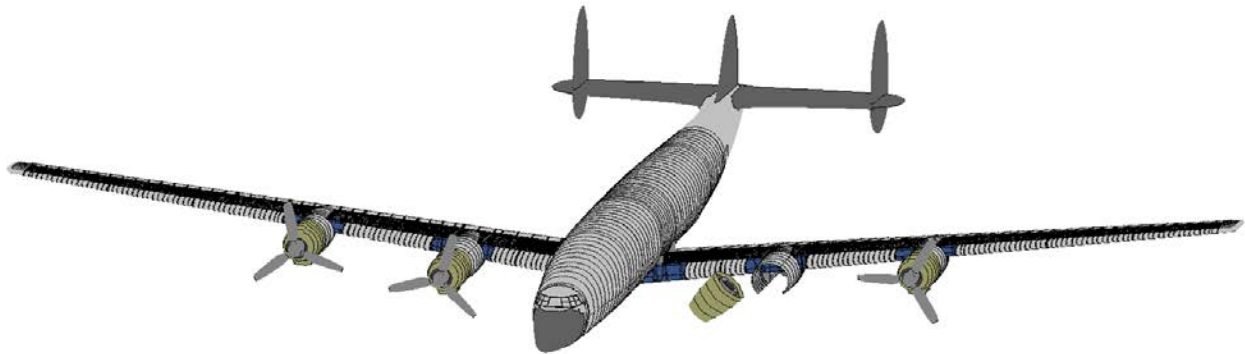


Figure 21. The L-1649 Model in its Initial State for Crash Simulation

Close inspection of the high-speed films shows that the inboard left engine separates from the nacelle due to the propeller impacting the main landing gear barrier. The engine then impacts the ground and tumbles into the leading edge of the wing about half way between the wing root and the inboard nacelle. It appears that liquid is released from the No.5 tank at the time of this impact. This sequence is shown in figure 22. This is also documented in reference 5: “At impact, both main landing gears were broken off. The left gear pulled the no. 2 engine nacelle downward as it failed, causing that engine to roll under the left wing.”

Since simulation of rotating propeller engines of the L-1649 was not of significant interest in the overall research, fairly simple models of these engines were developed without propeller rotation. Therefore, since the inboard port engine impact with the wing appears to be significant in the crash event, it was removed from the nacelle, rotated into the position seen in the video just before hitting the ground, and given the same initial velocities as the rest of the aircraft. The aircraft model with the engine in position at the beginning of the simulation is shown in figure 21.

The full-scale crash event, after the landing gear was removed, was essentially a collection of impact events.

- The right wing impacted with two telephone poles.
- The left wing impacted with the earth barrier.
- The left inboard engine impacted with the wing’s leading edge.
- The fuselage impacted with the ground.
- The engine and engine nacelle impacted with the ground.
- The subsequent potential impacts of tumbling engines with the wing.

All the impact event simulations were performed with the MPP version of LS-DYNA 971.R5.1 using 32 processors on an SGI Altix ICE 8200LX, which is a single-plane DDR 4X InfiniBand hypercube supercluster. Typical run times for each simulation were approximately 2 months.

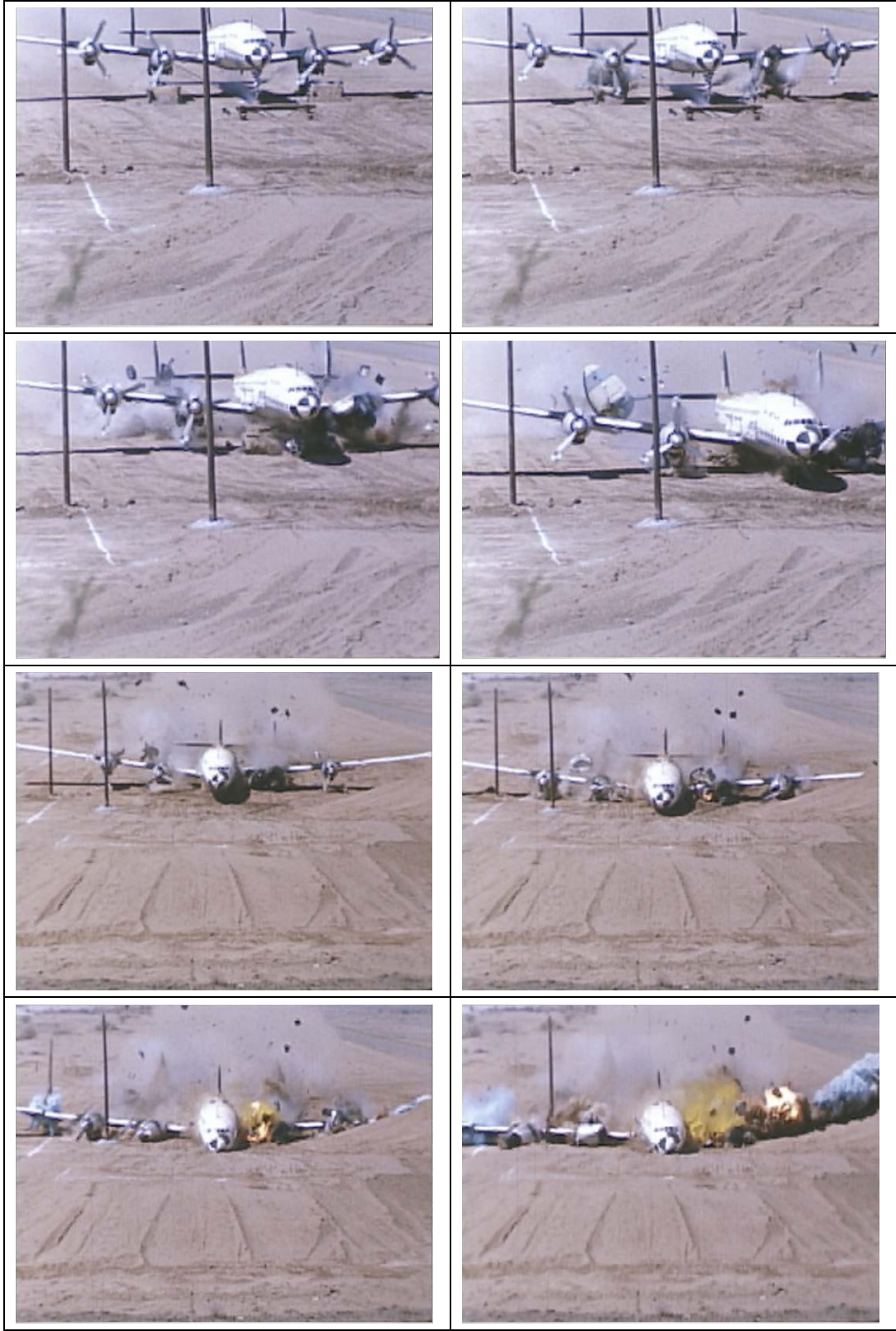


Figure 22. Video Footage of Engine Impact With the Wing's Leading Edge at Tank 5

## 5.1 COMPARISON WITH CRASH TEST.

This section provides a detailed comparison of the crash test results with the simulation. First, an overall evaluation of the crash sequence was made by comparing high-speed photography taken from various angles, focusing on the quantity of liquid released. Then the overall aircraft deceleration was compared with the data taken at the aircraft's center of gravity with onboard instrumentation. Structural damage of the wings after the aircraft came to rest was compared. Finally, the liquid released from each tank was assessed and the significant parameters that affected the release were examined.

To evaluate the relative effect of the modeling parameters considered in the uncertainty analysis, main effects plots were generated for the quantity of liquid released from each tank at various points in the crash sequence. To generate these plots, all responses at the minimum and maximum cases for an input parameter (i.e., material yield strength, connection ductility, etc.) were averaged and denoted as the “-” and “+” values for a parameter.

## 5.2 OVERALL COMPARISON.

High-speed photography was taken from various angles during the crash test. Using these photographs, a detailed visual comparison was made between the simulated and test results for the telephone pole impacts on the right wing (front view) (see figures 23 through 29), for the telephone pole impacts on the right wing (side view) (see figures 30 through 34), and, from a front view, for the entire crash event (figures 35 through 40). Unfortunately, the camera showing the impact face of the soil barrier was obstructed with dust just before the wing impacted. Therefore, a comparison could not be made of this event, aside from the overall front view of the crash test. The fireball that developed around the right (starboard) engines was due to the small amount of fuel used to run the engines and not from fuel in the wing tanks.

The front view of the telephone pole impacts on the right wing shows an overall good agreement between the eight runs conducted and the videographic data. In many of the simulations at early times (1.018 to 1.086 s), the initial release of dyed water was consistent with the test data. In general, the release appears to be visually smaller than in the video because the water quickly aerosolized in the test and spread over a wider area. This was evident by the fine mist observed in the photography, particularly evident at the periphery of the plume of dyed water. Effects of aerosolization were not included in the simulation. Likewise, the fidelity of the particles used in the simulations (approximately 2.5 in.) was too coarse to capture the very small release of aerosolized liquid observed at the early time of 1.018 s. However, all simulations also showed front spar cracks, which was consistent with this small liquid release.

At later times (1.215 to 1.274 s), all runs also showed a large amount of liquid was released from Tank 4 (water dyed blue) beneath the wing as the bottom skin panel opened along the front spar. Much less liquid was observed above the wing. At the latest times (1.427 and 1.585 s), red gelled water was released from Tank 3 in most of the simulation runs, but not just from the telephone pole impact. The liquid was not released until later when the engine nacelle and wing hit the ground. This was also consistent with the simulations.

In the side view of the telephone pole impacts on the right (starboard) wing (figures 30 through 34), the bending and failure of telephone pole 1 (outboard pole) closely resembled the test footage just after impact (1.041 s). Best agreement was observed for the overall telephone pole deformation, failure, and kinematics for the runs with the higher bound for pole strength (Runs 1, 3, 6, and 8), indicating that the actual telephone pole strength was likely closer to the upper bound. The portion of the wing outboard of the telephone pole impact was observed to turn upward relative to the rest of the wing at 1.131 s, both in the crash test and in all simulations. The wing rotation and timing for when the wing tip impacted the ground varied by run after that. The same general conclusions regarding the dyed water release were observed in both the side and front views already discussed.

In the front view of the crash test (figures 35 through 40), the initiation of leakage from Tank 5 (water dyed yellow) is shown in the first figure and large plumes are released subsequently. The release of water at 1.045 s is only observed in the simulations when the inboard port engine impacts the wing in Runs 1, 2, 7, and 8 and is, therefore, the likely cause of the damage to the fuel tank. Note that in all cases, the blue dyed water was dramatically released from Tank 1 (outboard tank that impacts the soil barrier) as observed in the test. The fuselage yaw varied from run to run, but was, generally, in good agreement at 1.22 to 1.589 s when it first yawed to the port. Most cases then yawed to starboard in agreement with the test.

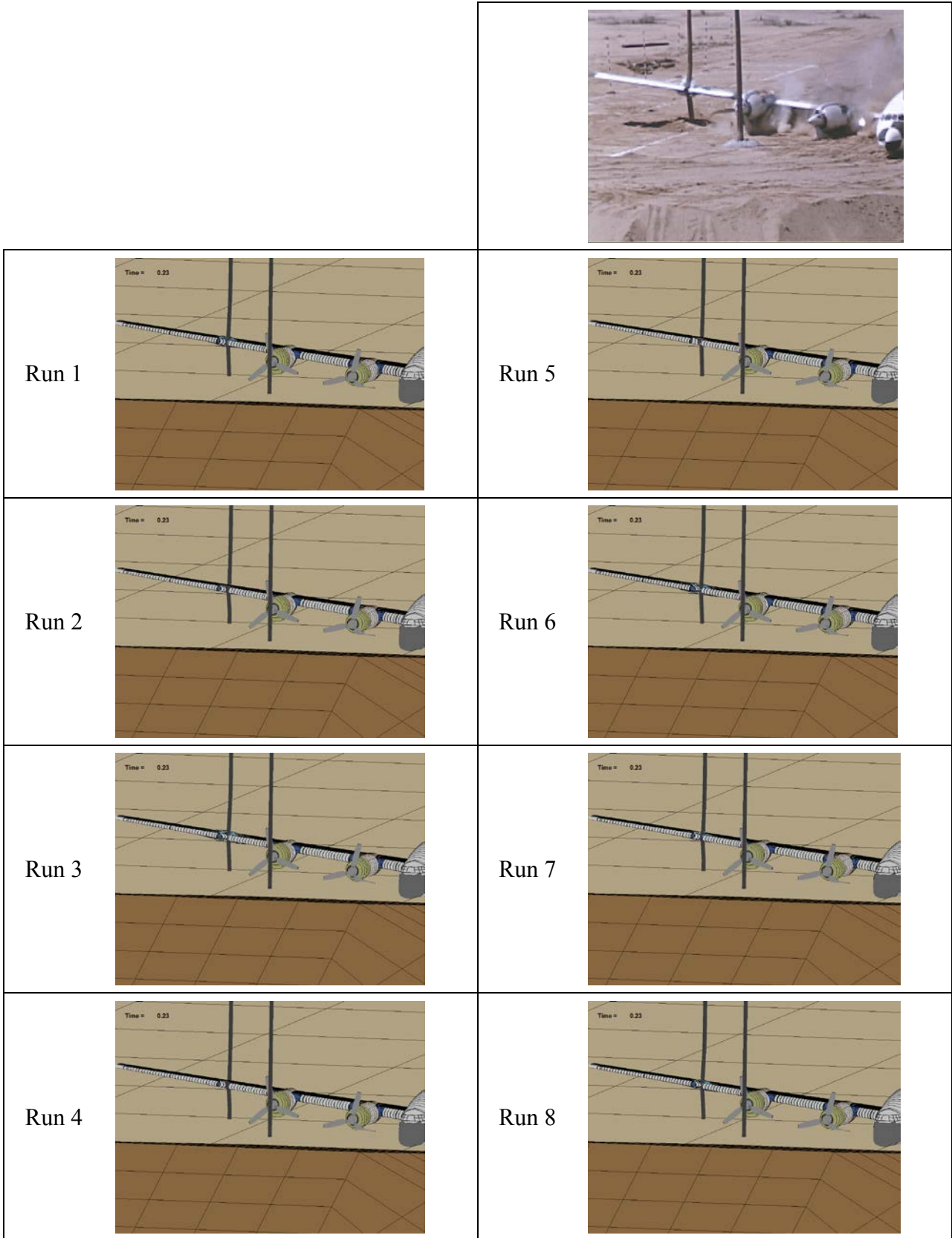


Figure 23. Crash Test Comparison of Telephone Pole Impacts (front view)—Time = 1.018 s



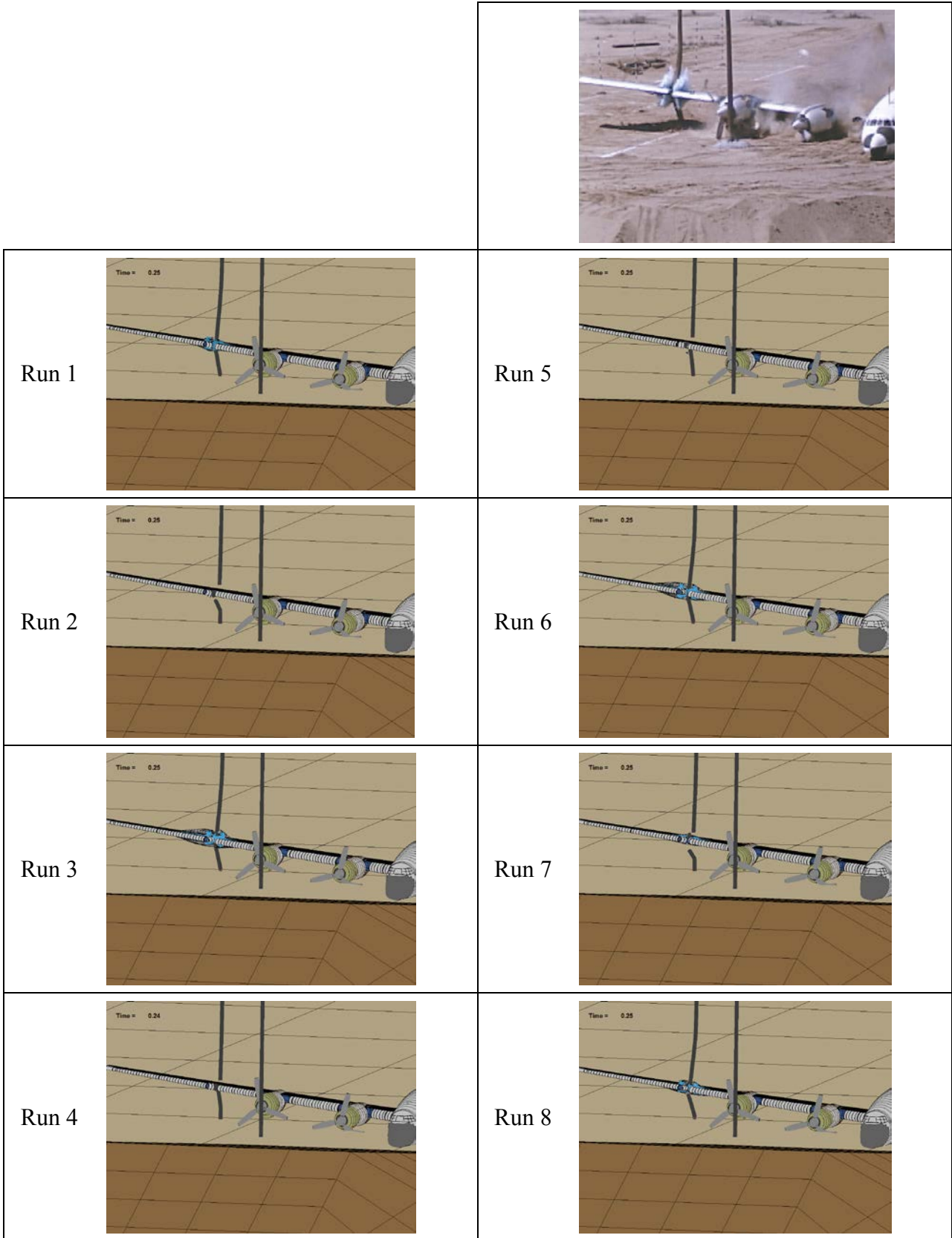


Figure 24. Crash Test Comparison of Telephone Pole Impacts (front view)—Time = 1.041 s

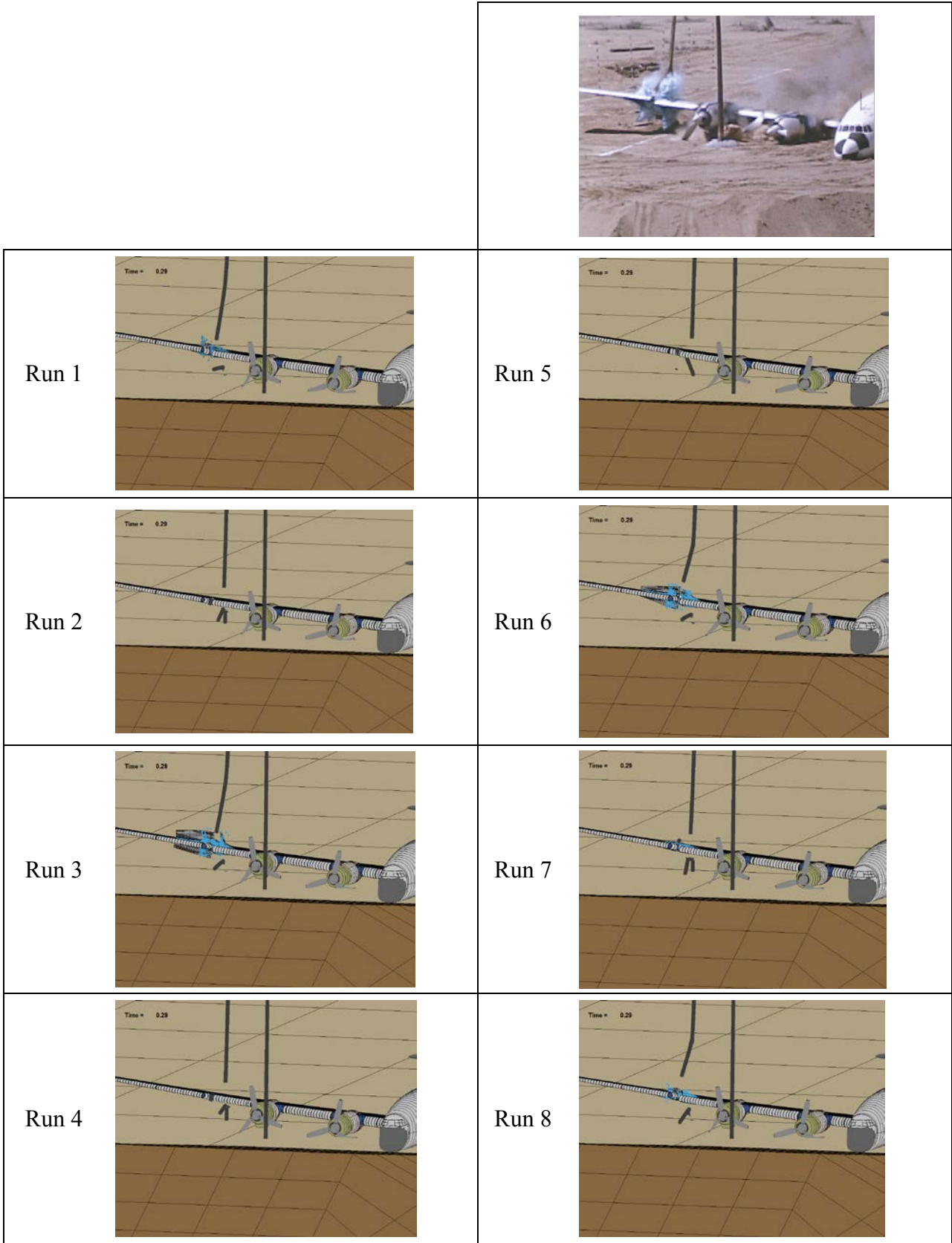


Figure 25. Crash Test Comparison of Telephone Pole Impacts (front view)—Time = 1.086 s



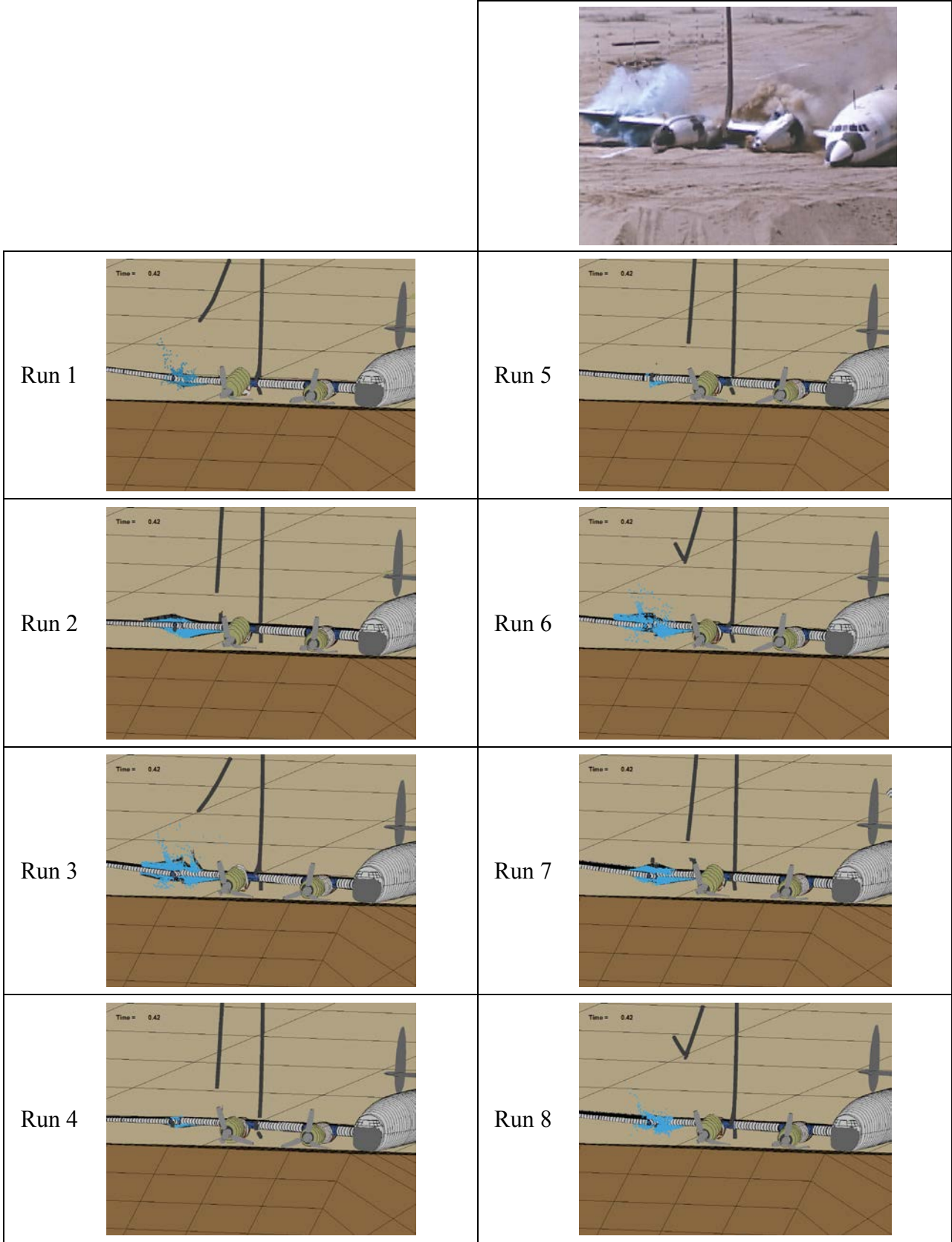


Figure 26. Crash Test Comparison of Telephone Pole Impacts (front view)—Time = 1.215 s

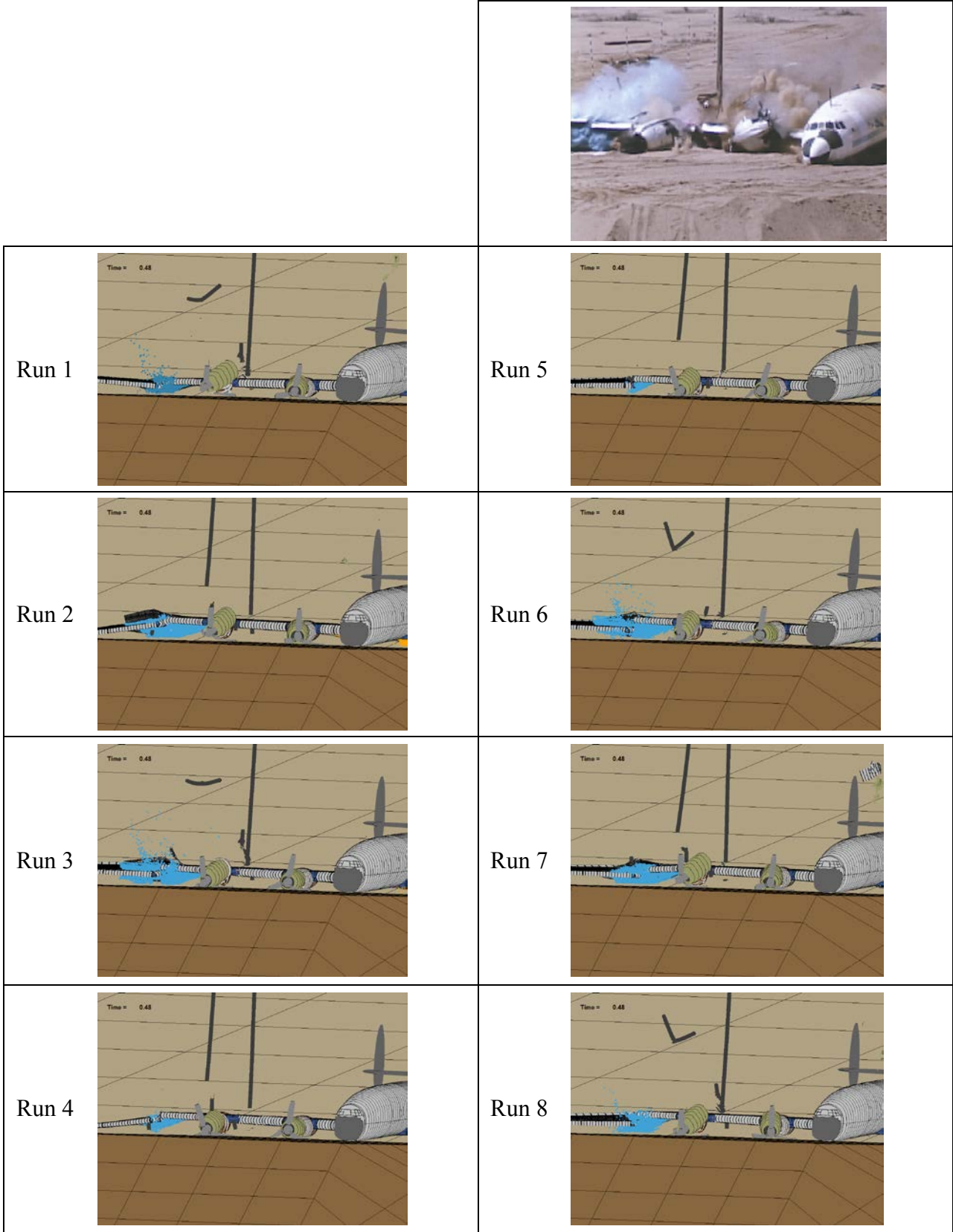


Figure 27. Crash Test Comparison of Telephone Pole Impacts (front view)—Time = 1.274 s

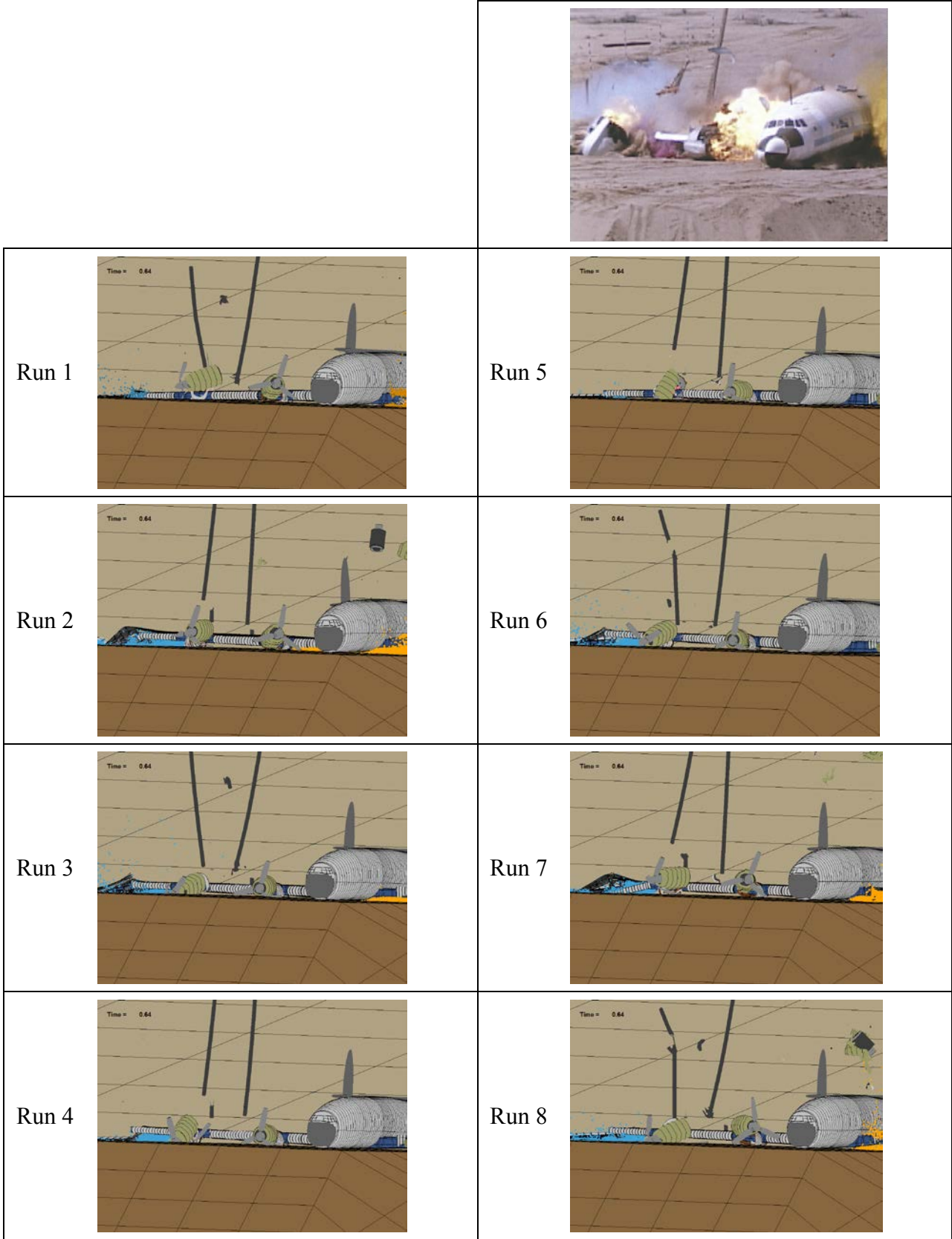


Figure 28. Crash Test Comparison of Telephone Pole Impacts (front view)—Time = 1.427 s

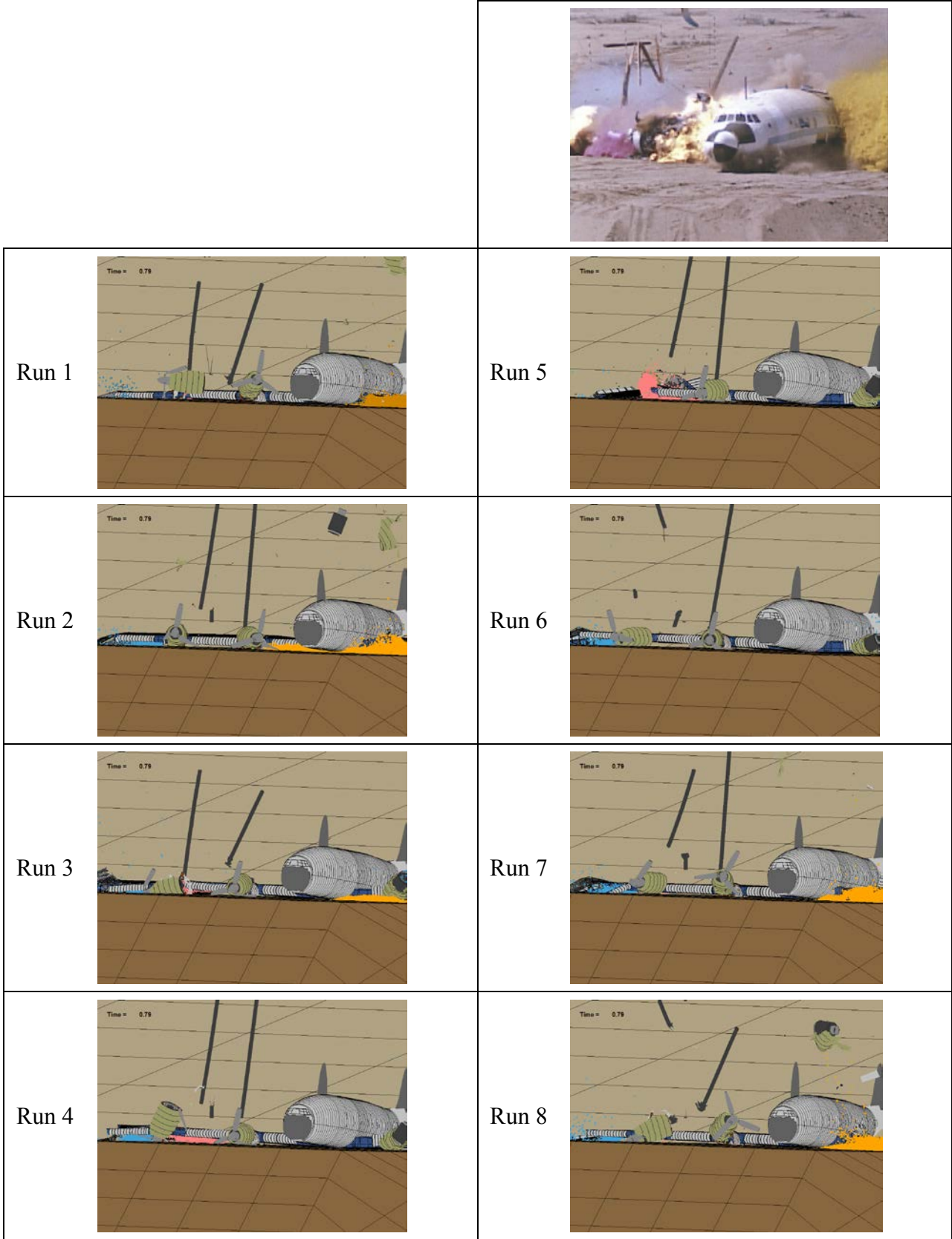


Figure 29. Crash Test Comparison of Telephone Pole Impacts (front view)—Time = 1.585 s



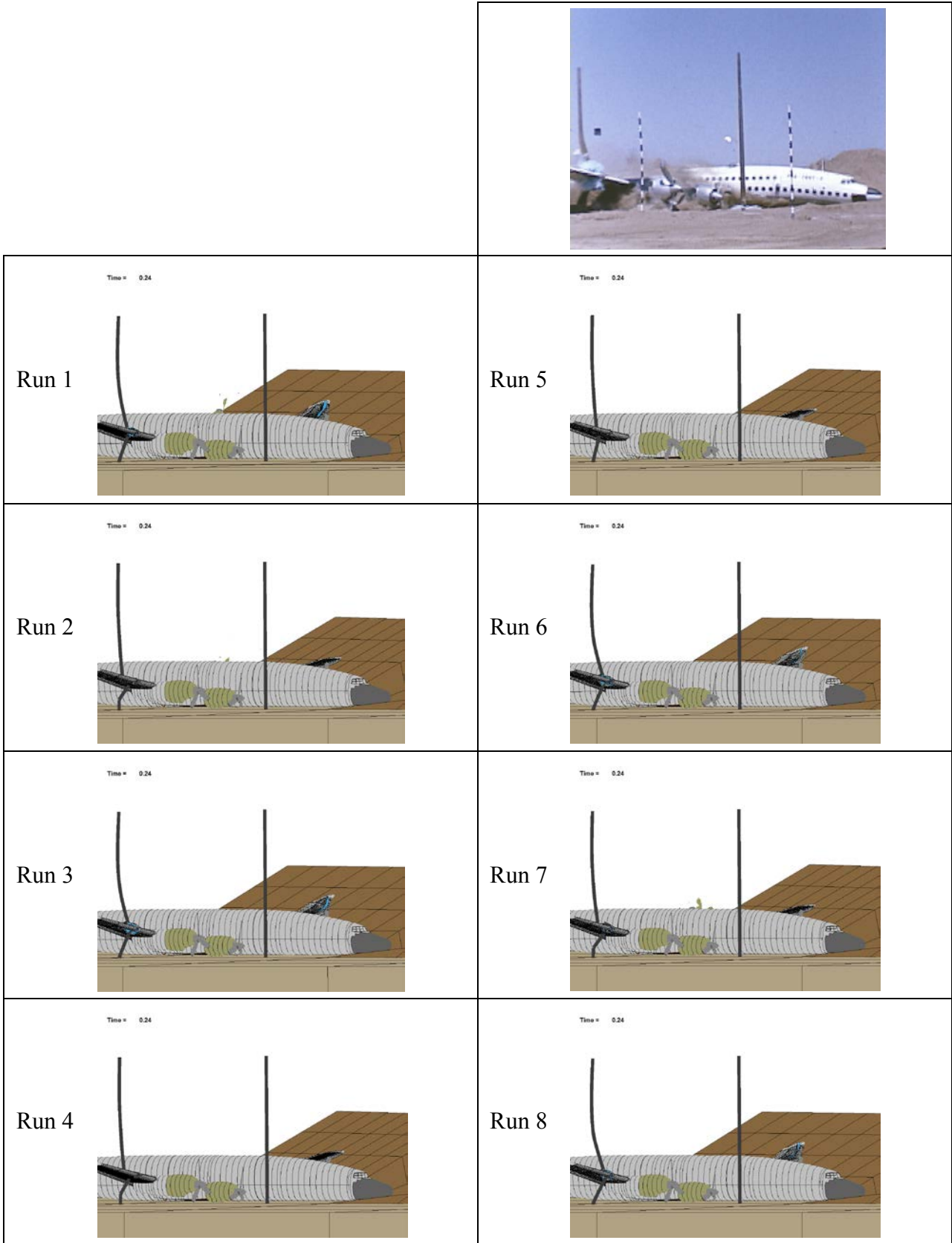


Figure 30. Crash Test Comparison of Telephone Pole Impacts (side view)—Time = 1.041 s

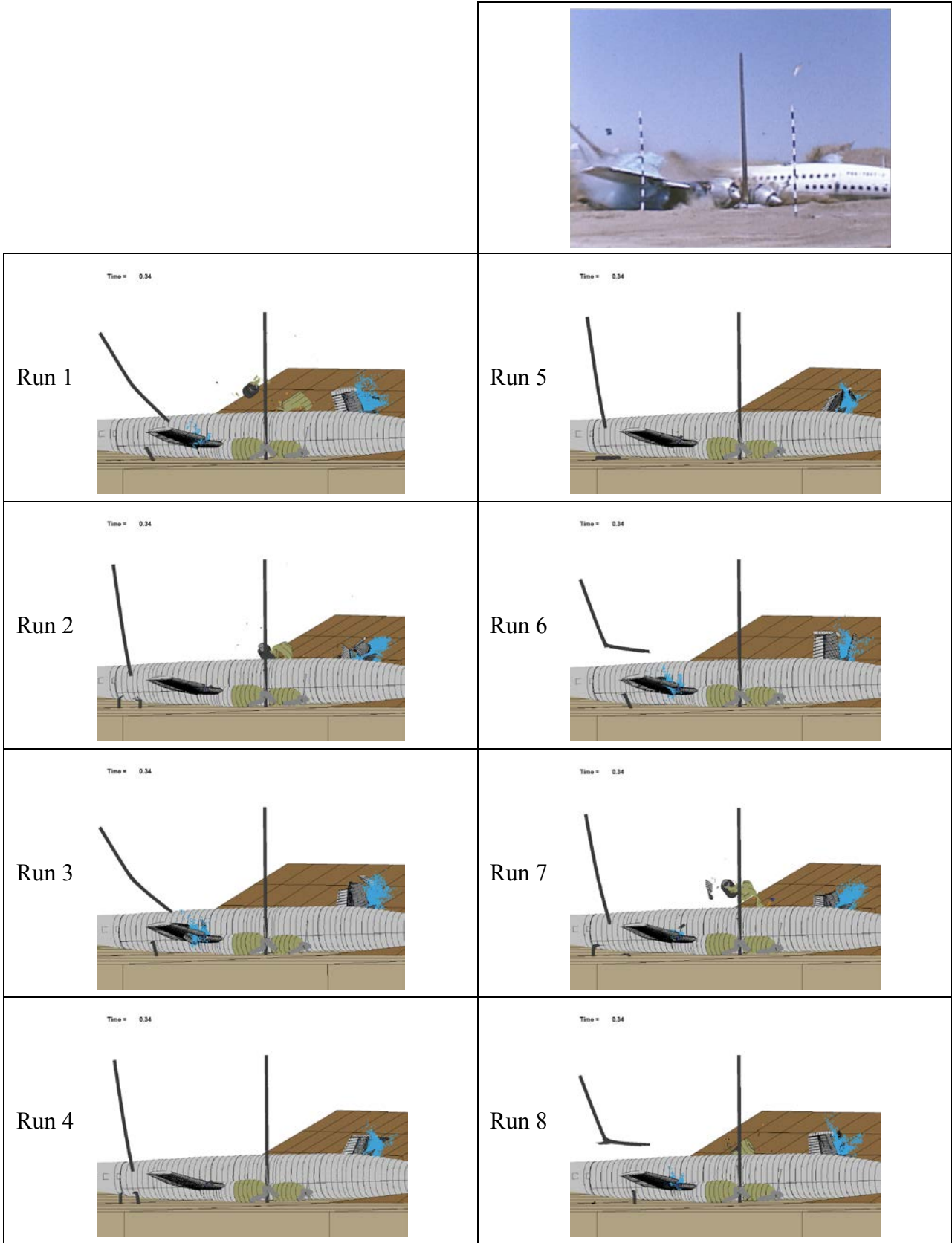


Figure 31. Crash Test Comparison of Telephone Pole Impacts (side view)—Time = 1.131 s

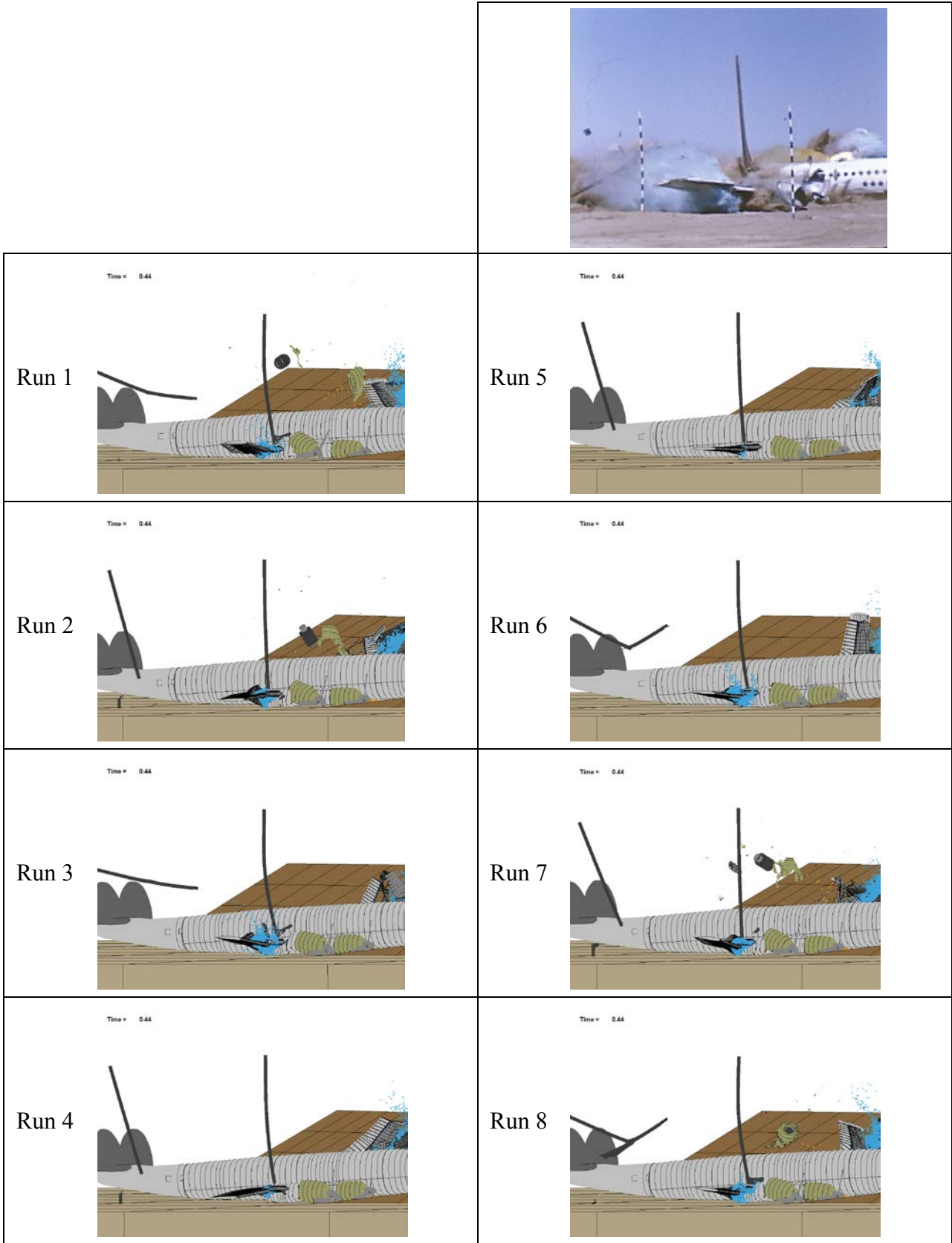


Figure 32. Crash Test Comparison of Telephone Pole Impacts (side view)—Time = 1.230 s

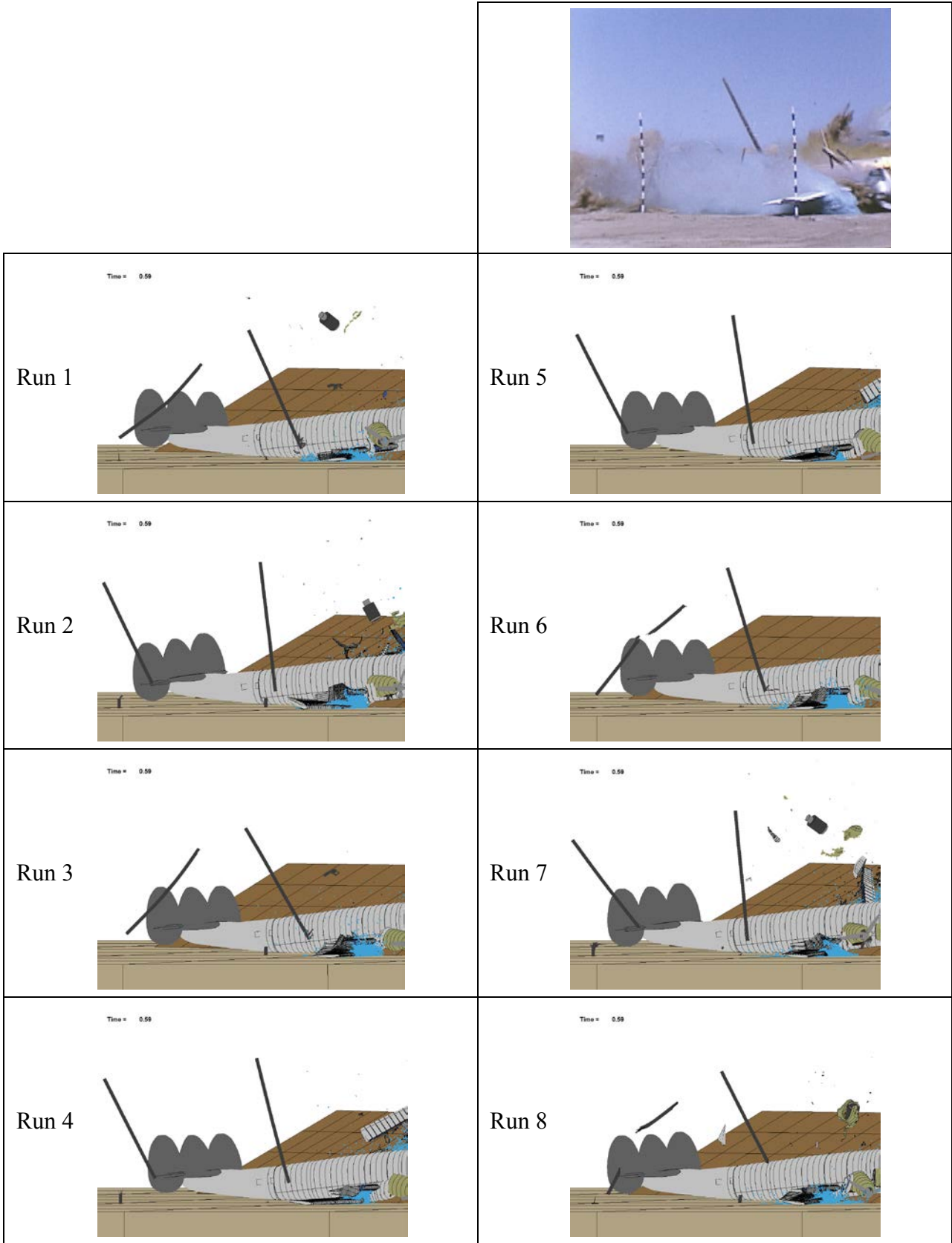


Figure 33. Crash Test Comparison of Telephone Pole Impacts (side view)—Time = 1.379 s



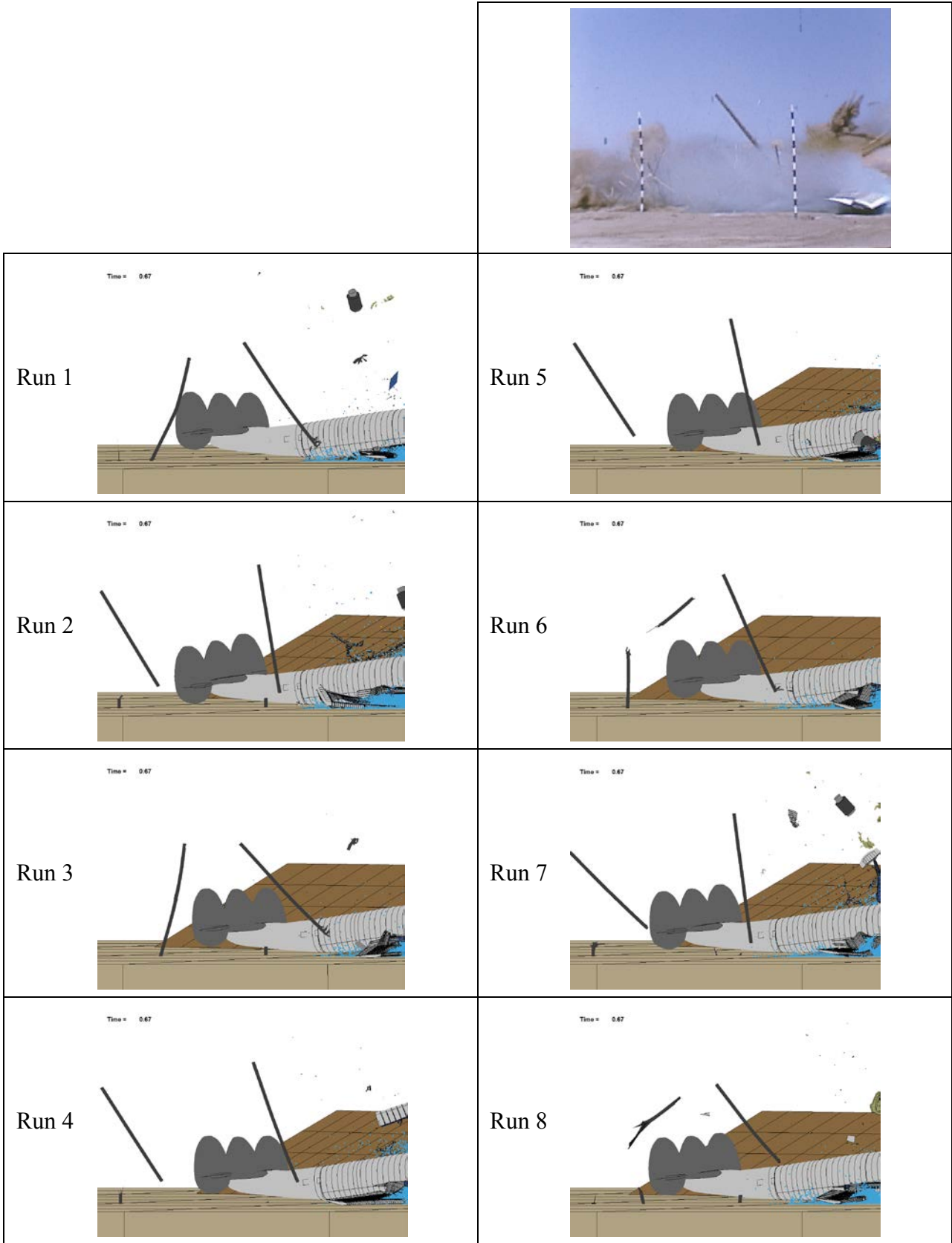


Figure 34. Crash Test Comparison of Telephone Pole Impacts (side view)—Time = 1.460 s

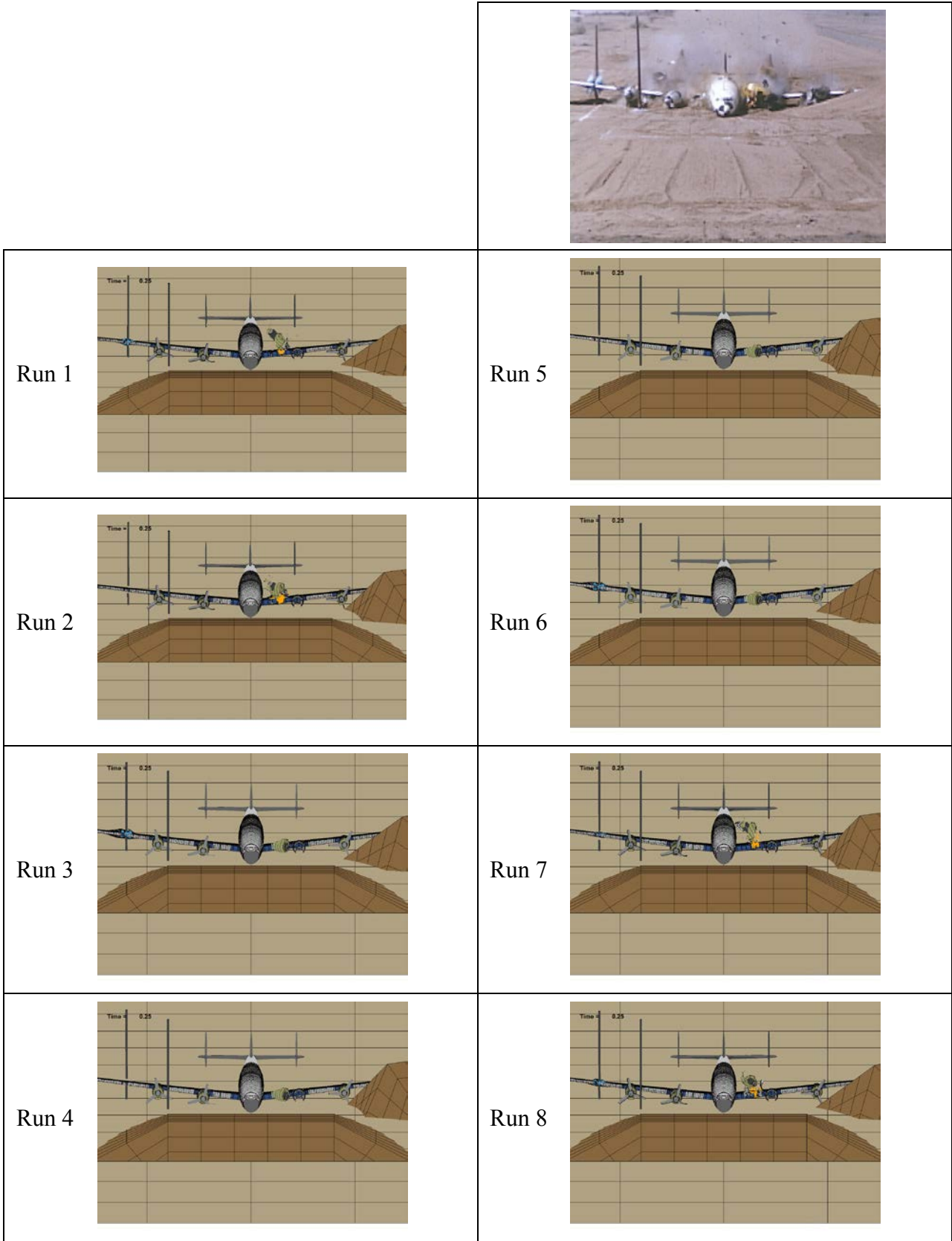


Figure 35. Crash Test Comparison (front view)—Time = 1.045 s

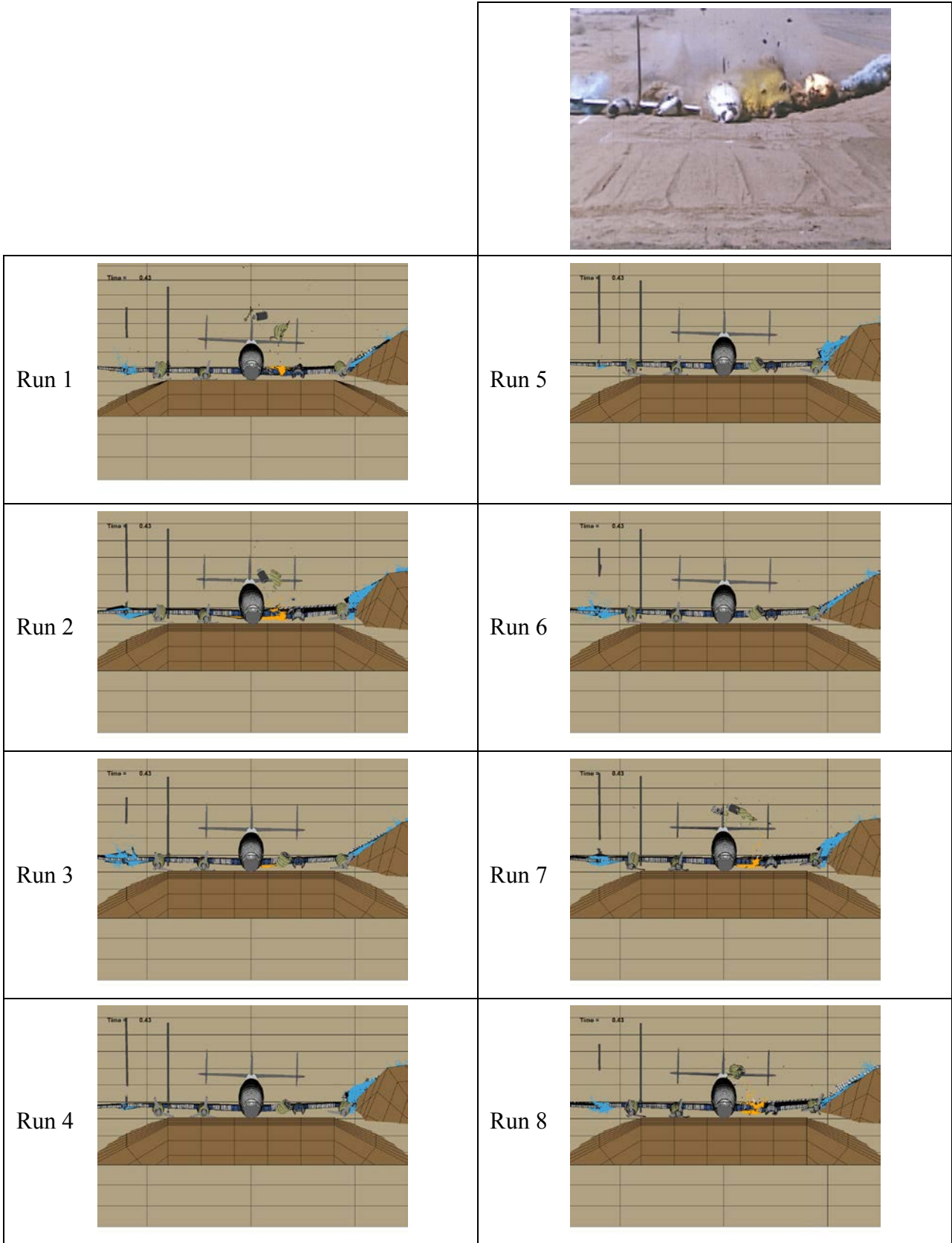


Figure 36. Crash Test Comparison (front view)—Time = 1.220 s

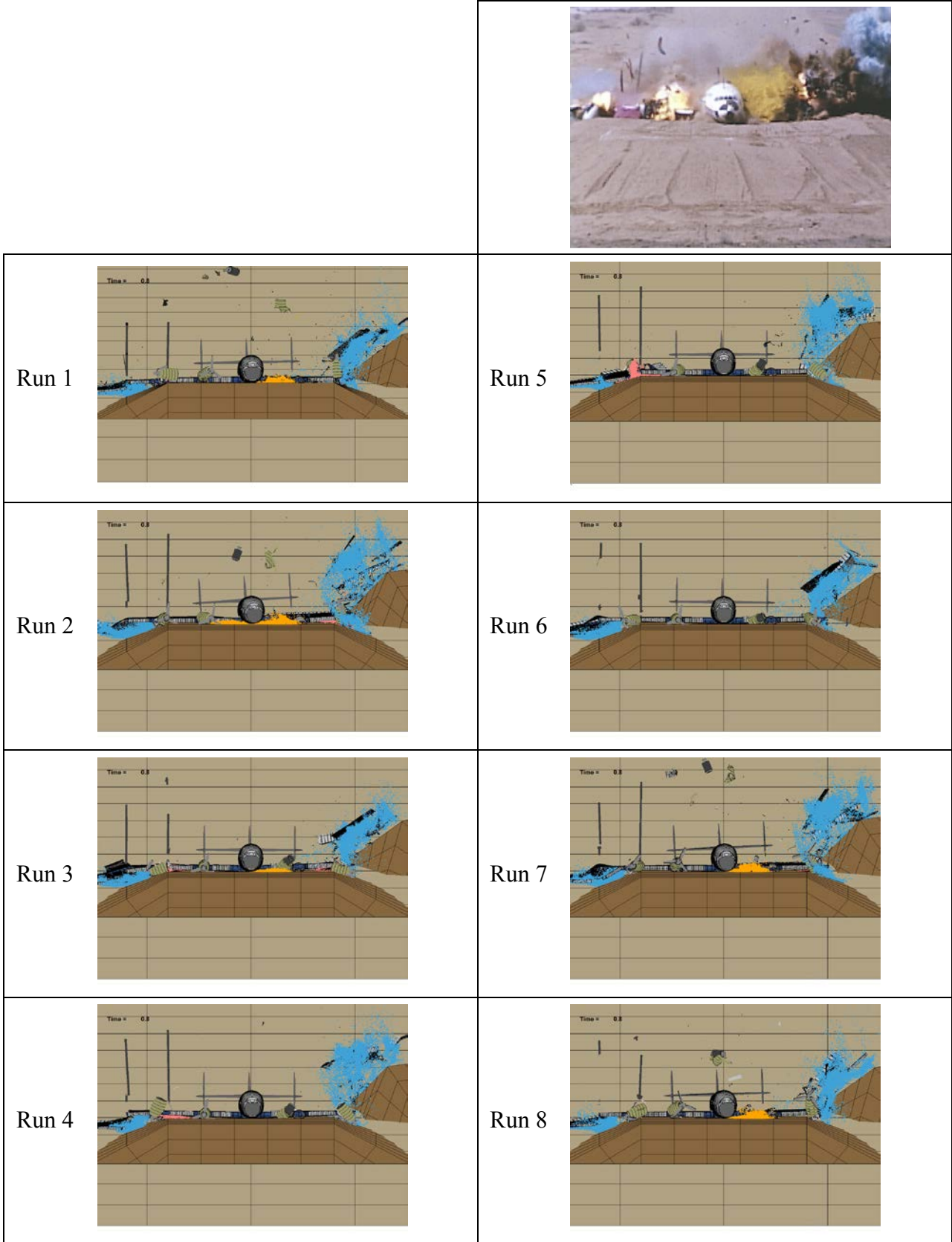


Figure 37. Crash Test Comparison (front view)—Time = 1.589 s



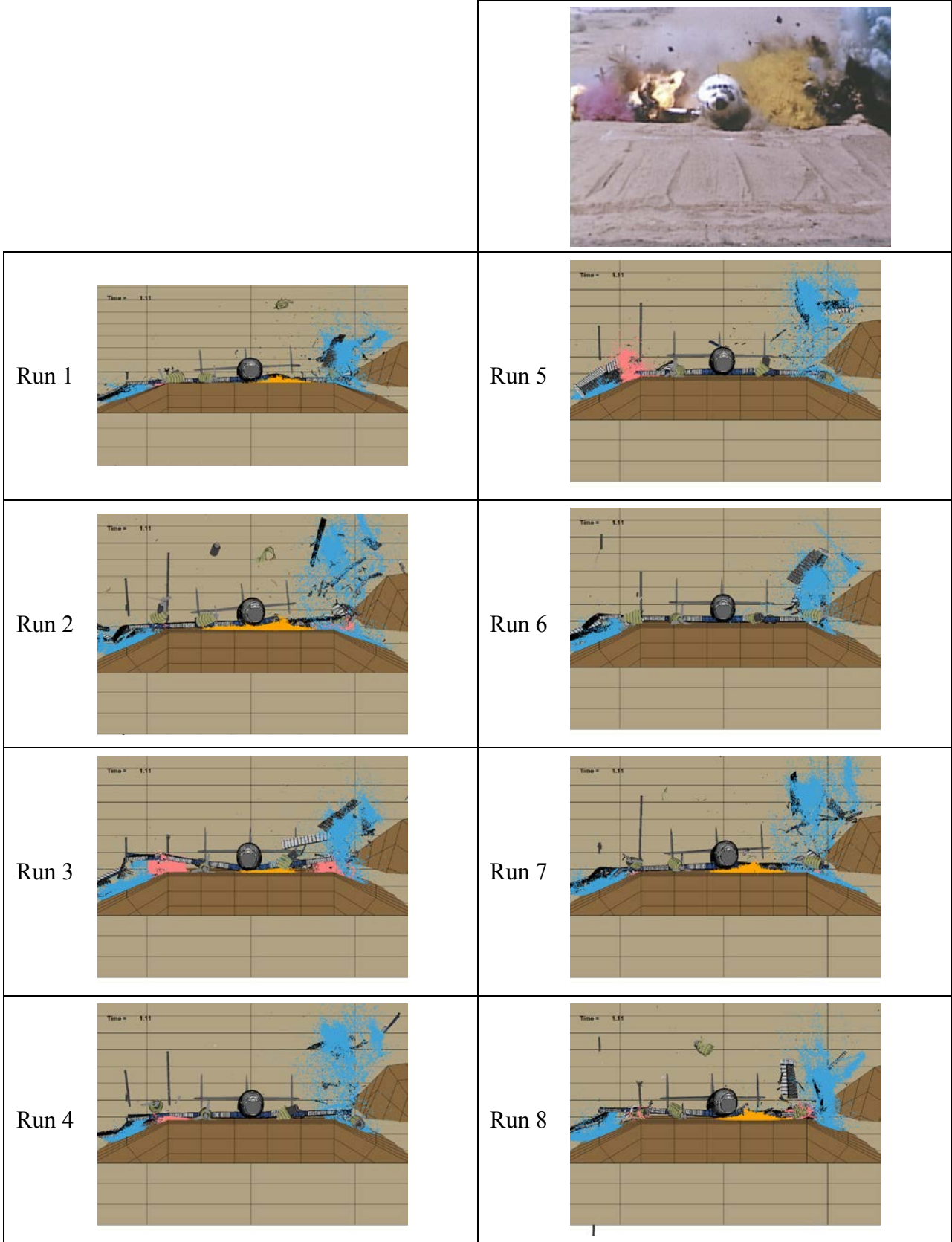


Figure 38. Crash Test Comparison (front view)—Time = 1.904 s

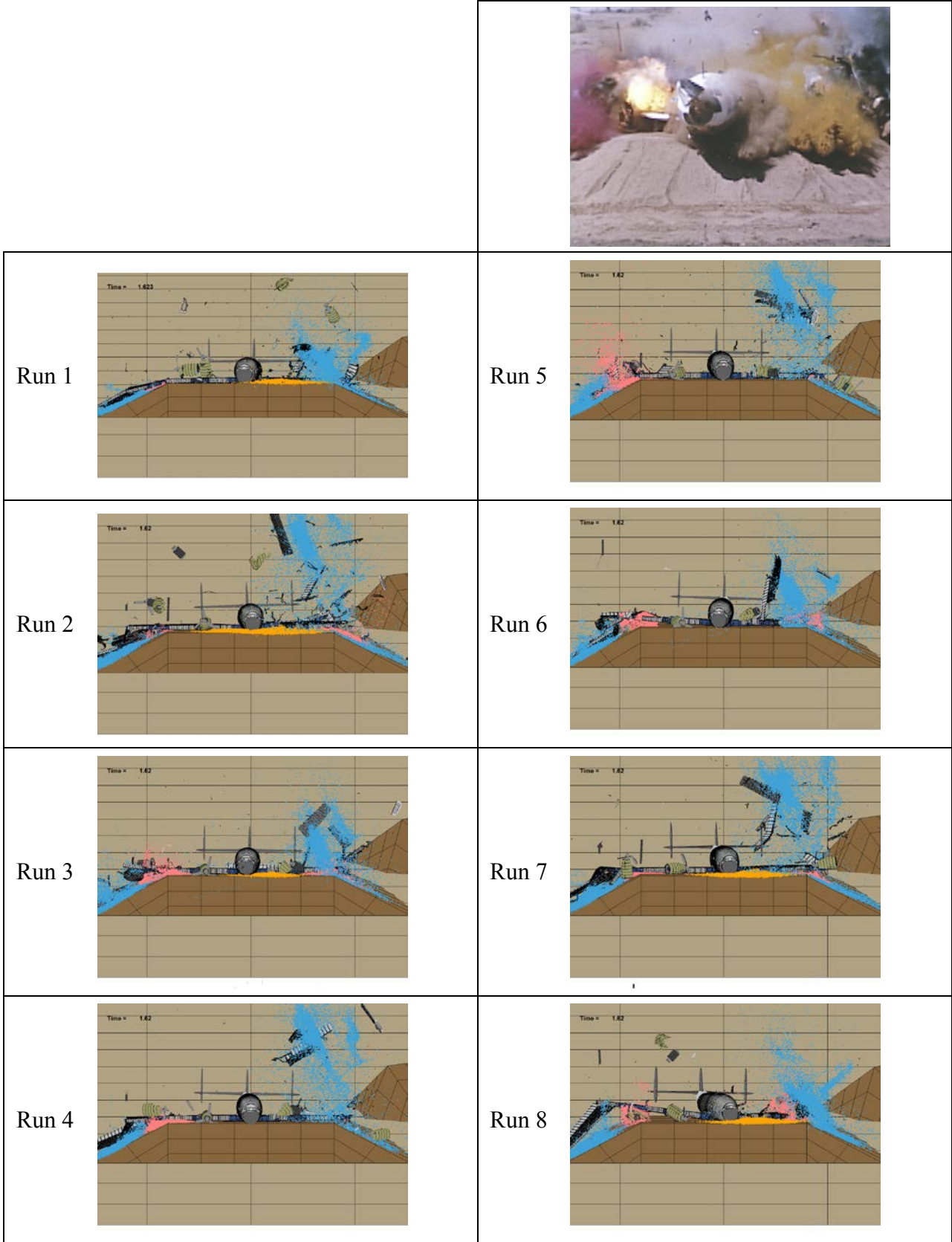


Figure 39. Crash Test Comparison (front view)—Time = 2.417 s

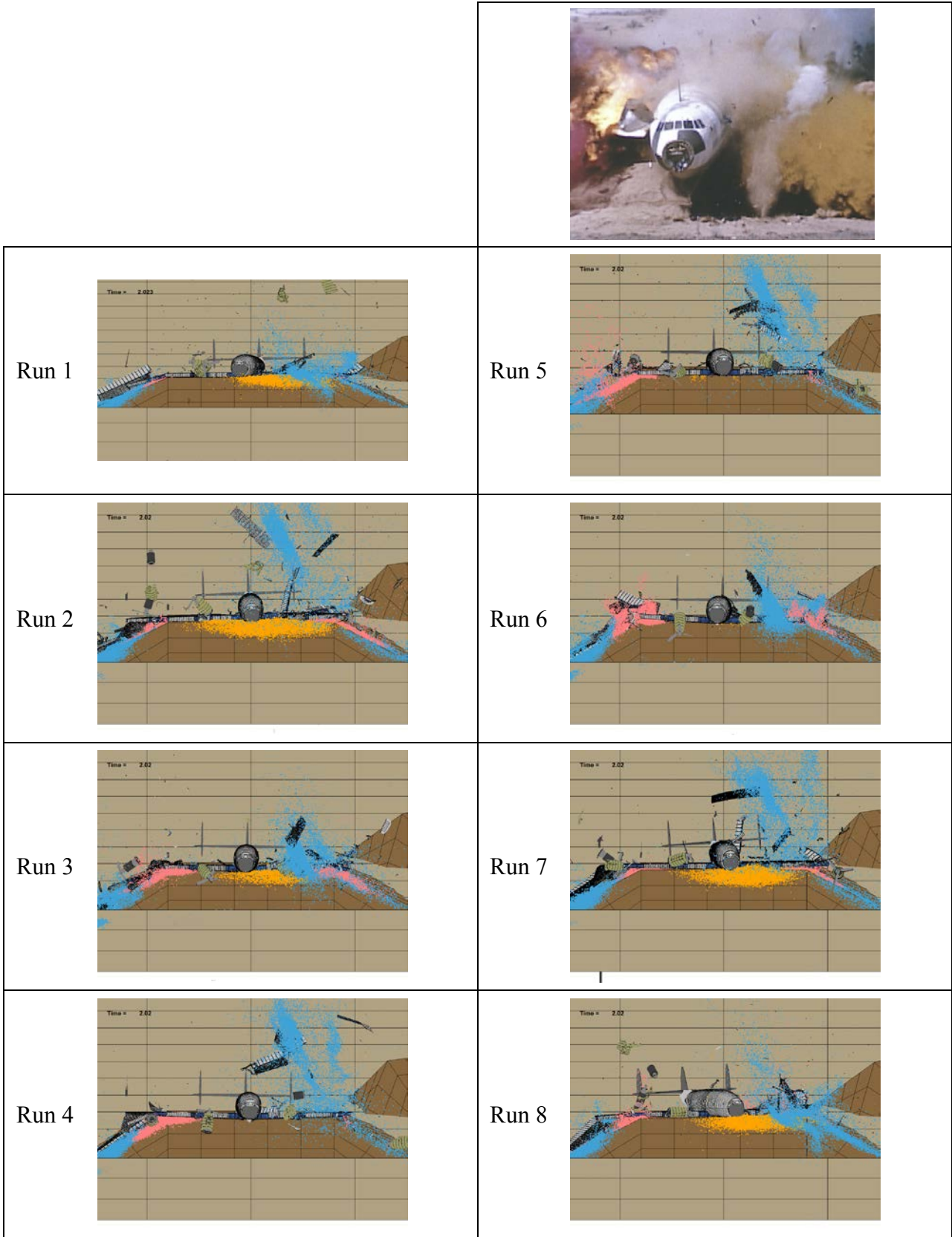


Figure 40. Crash Test Comparison (front view)—Time = 2.808 s

Acceleration data from the onboard instrumentation were also compared. Figure 41 shows a comparison of the velocity-time history at the aircraft's center of gravity. Experimental data from an accelerometer placed on the fuselage floor at the center of gravity were digitized and integrated. Only certain time periods were available from the test report [5] so the velocity was linearly extrapolated as shown in figure 41. Also shown are the times at which each significant event occurred in the crash sequence.

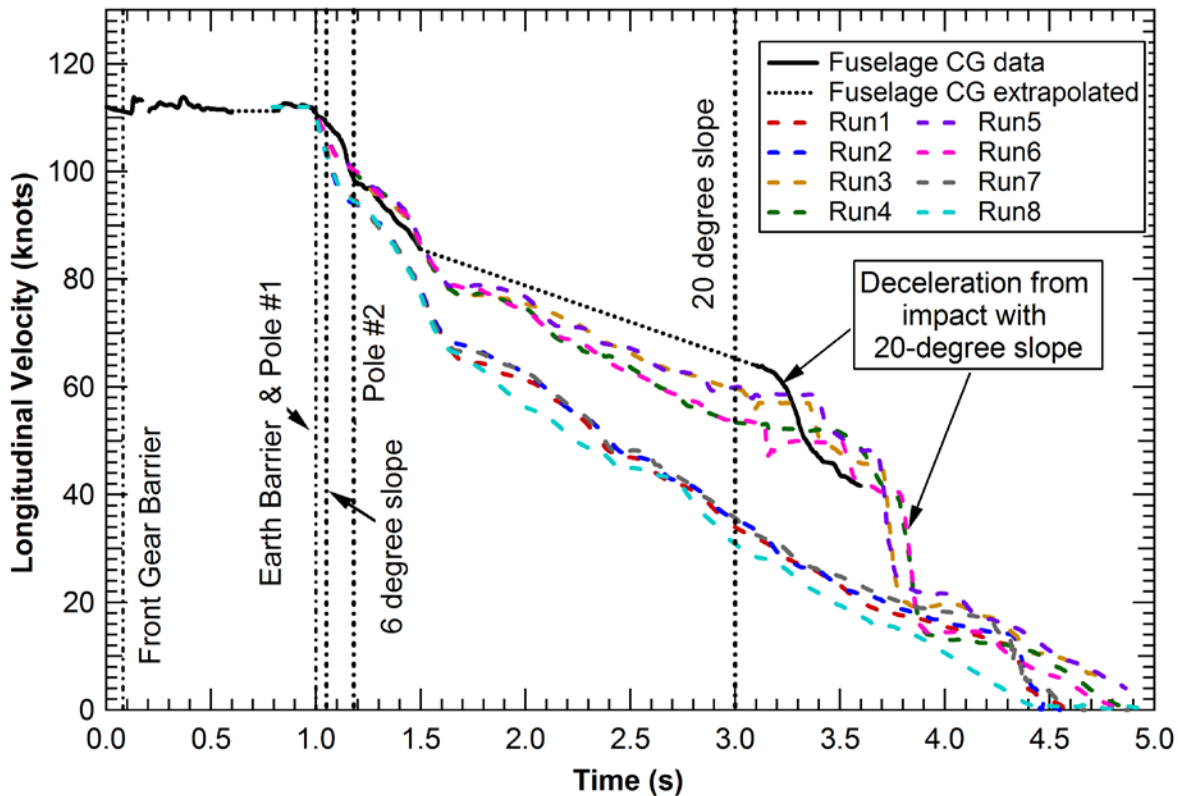


Figure 41. Comparison of the Velocity-Time History at the Aircraft's Center of Gravity

The fuselage deceleration around the time of the initial impact events, 1.0 to 1.5 s, with telephone poles and earth barriers was, generally, in good agreement. The best agreement was for Runs 3 through 6, which all have the lower bound for the ground friction coefficient. The sharp deceleration observed at approximately 3.2 s in the experiment and 3.7 s in Runs 3 through 6 was from impact with the 20° slope. The runs with the upper bound for friction with the ground do not fully reach the 20° slope, as shown in figure 42. In fact, the lower bound still appears to be too high since the aircraft engages with the 20° slope roughly 0.5 s sooner in the test, indicating that it was traveling at a greater average speed while sliding up the 6° slope. A value 10%-15% lower would likely yield the best comparison.



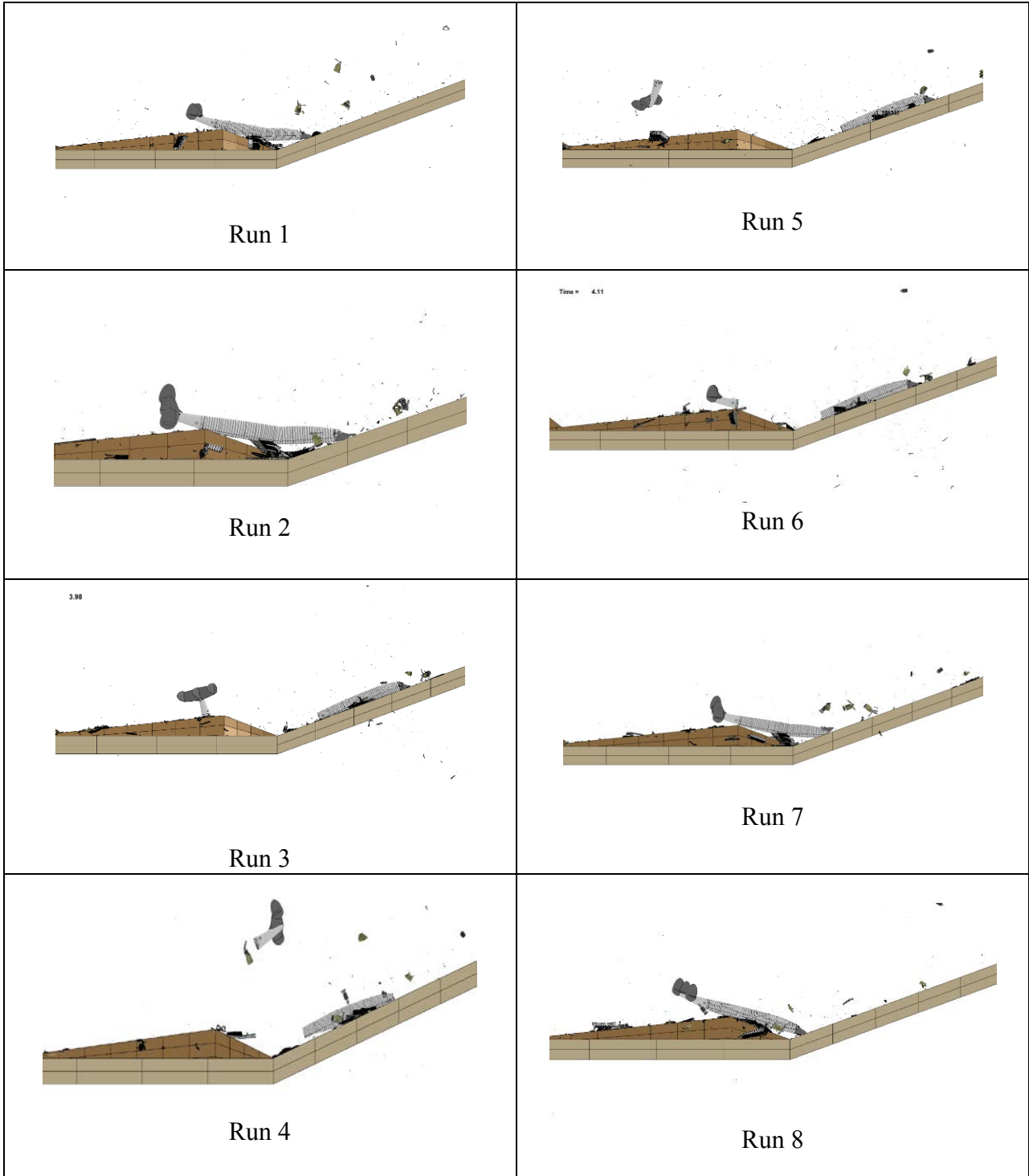


Figure 42. The L-1649 Final Resting State

Of particular interest was the liquid expelled from the tanks during the crash event. If this were fuel, some of it would burn as it aerosolized during release. Fuel left in the integral tanks, but with damage to the tanks, would leak out into the fuselage area when it came to rest, feeding a pool fire around the aircraft.

Figures 43 through 51 show a comparison of liquid dispersed during the crash. The sketches in these figures are from the test report [5]. It should be noted that the times indicated in the sketches have been modified from the test report [5]. The first image, figure 43(a), shows fuel spillage due to impacts with both telephone poles and was labeled with a test time of 1.0 s in the test report [5]. This cannot be accurate since impact with the second telephone pole does not occur until sometime after 1.09 s, as shown in figure 19 of the test report [5]. It was estimated that the first sketch occurred at 1.25 s. At this time, the first evidence of the red gelled water was observed in the high-speed photography. The times for all subsequent sketches were, therefore, increased by the same 0.25 s from that listed in the test report [5].

Liquid was expelled from the wing and extended backward in a plume from the impact loads (in the simulation) in addition to the aerodynamic drag in the test. The drag was not included in the simulation. Therefore, in general, the plume was observed to extend further back behind the wing in the sketches. The plume from Tank 1, which was dominated by the impact with the earthen barrier, looks very similar until the plume is significantly spread out by aerodynamic drag. Except at 2.90 s, where the liquid trailing behind the aircraft was observed to extend out further than in the sketches. This was because some of the liquid that was visible in these images had been stopped by hitting the ground. It is unlikely that this fuel was part of what was included in the sketch.

Liquid was also observed to extend out in front of the wing due to wing damage and the aircraft's deceleration. The liquid was ejected forward due to its momentum that was no longer contained by the decelerating tank. There are many similarities in the sketches, depending on the run. As the crash event progressed, the liquid progressively extended further out from the wing than in the sketches for many simulations. This was likely caused by the greater deceleration in the simulations.

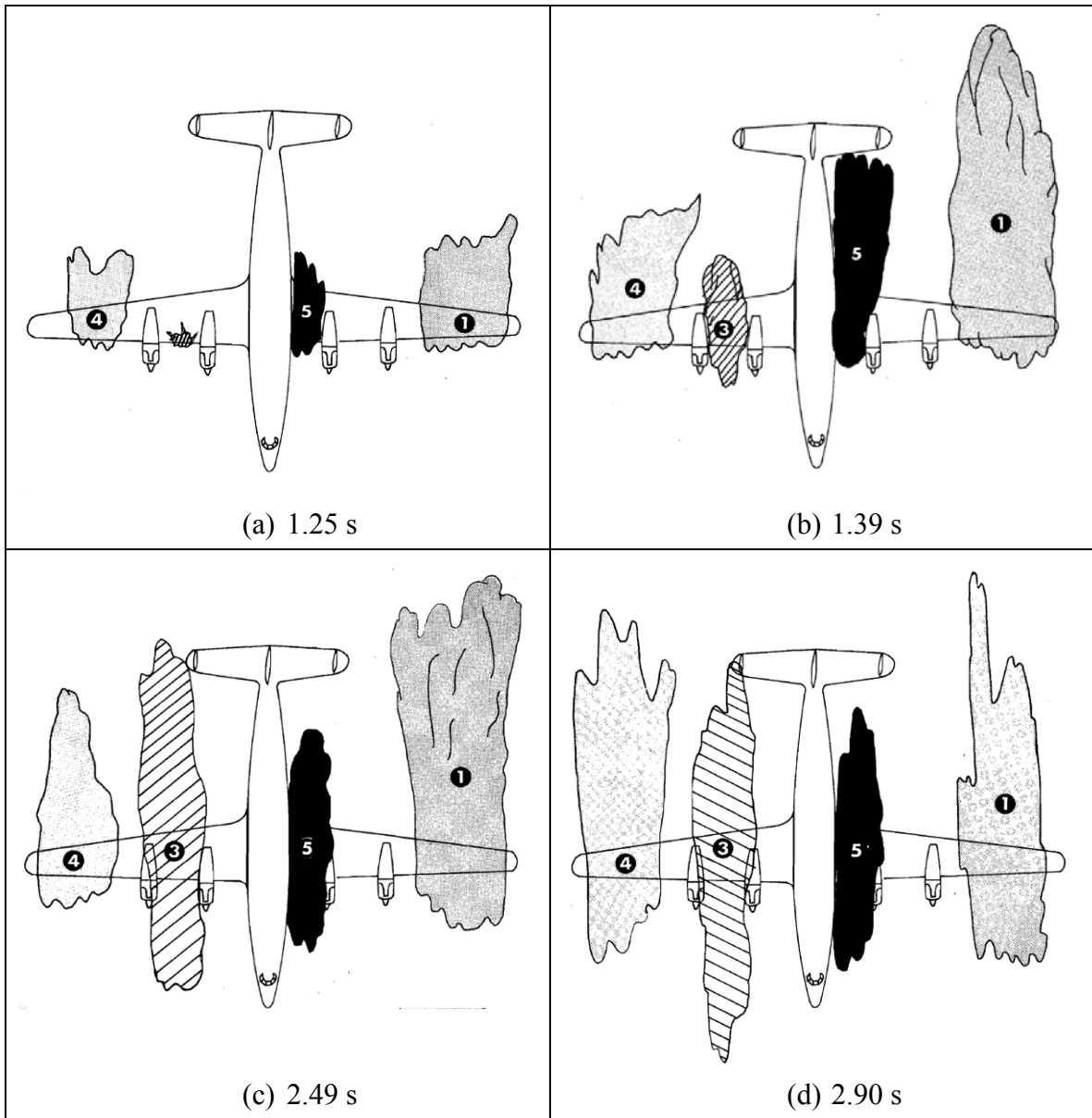


Figure 43. Sketches of Fuel Spillage Documented From High-Speed Photography of the L-1649 Full-Scale Crash Test [5] (Times shown are after main gear impact.)

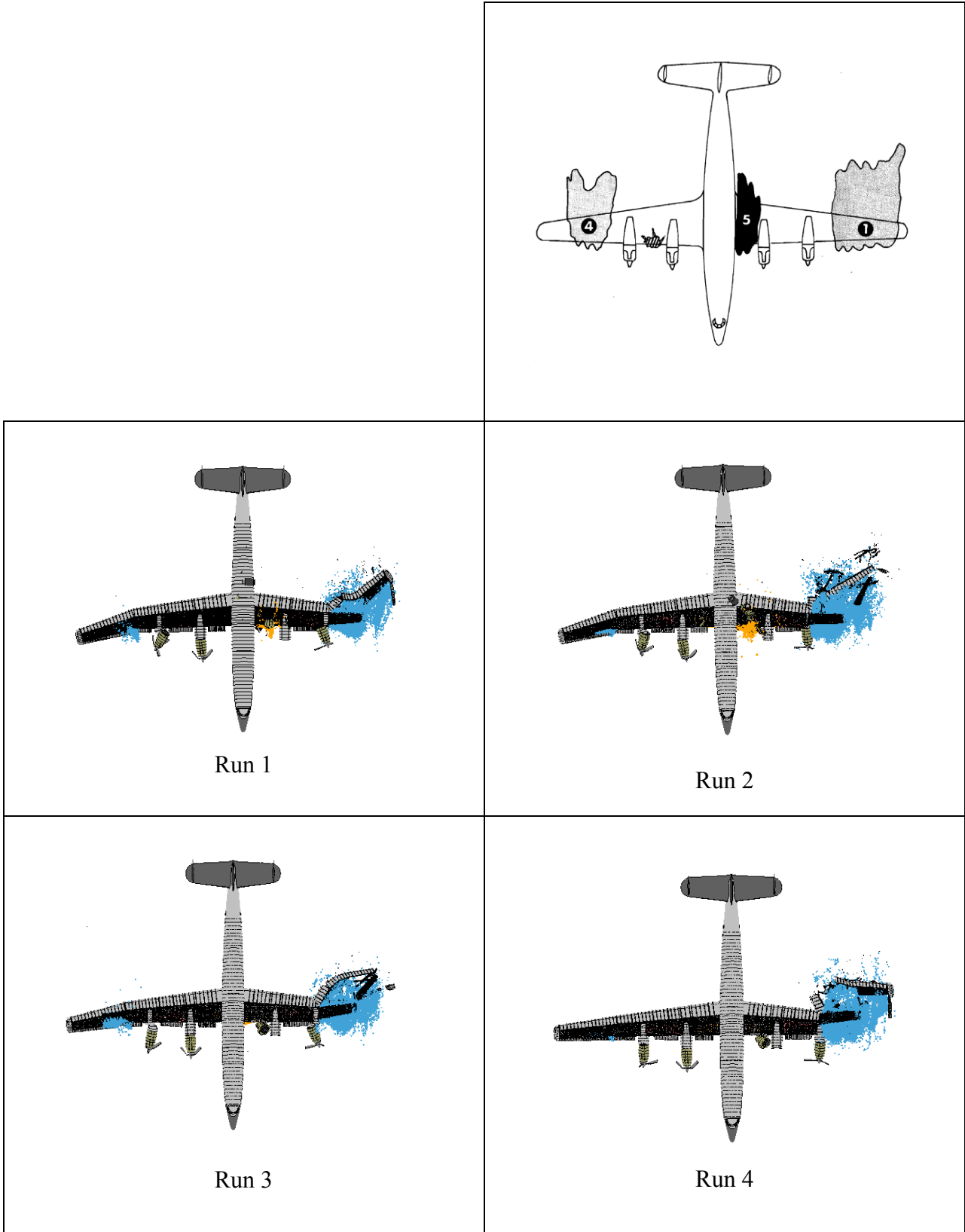


Figure 44. Fuel Spillage—Time = 1.25 s (Runs 1-4)

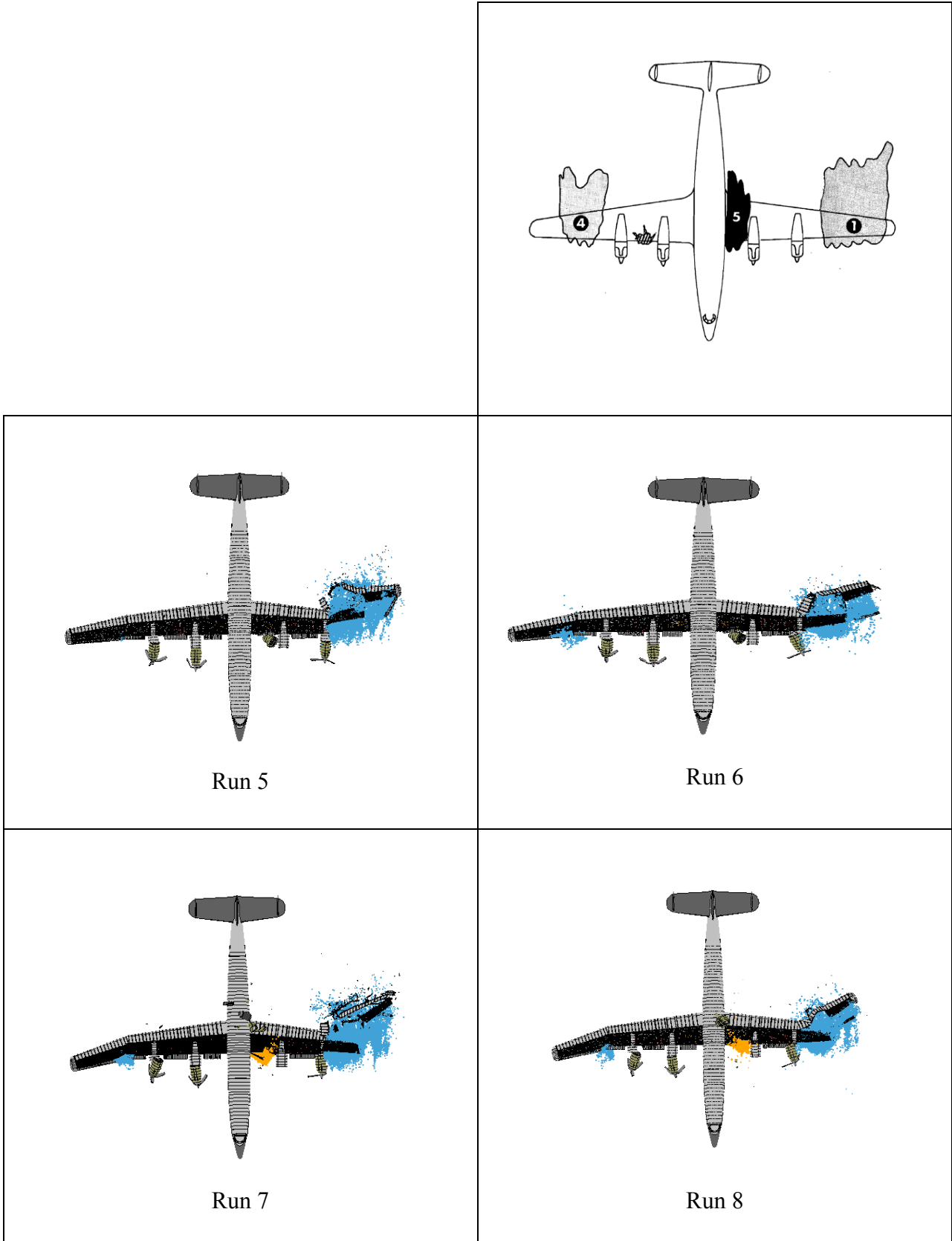


Figure 45. Fuel Spillage—Time = 1.25 s (Runs 5-8)

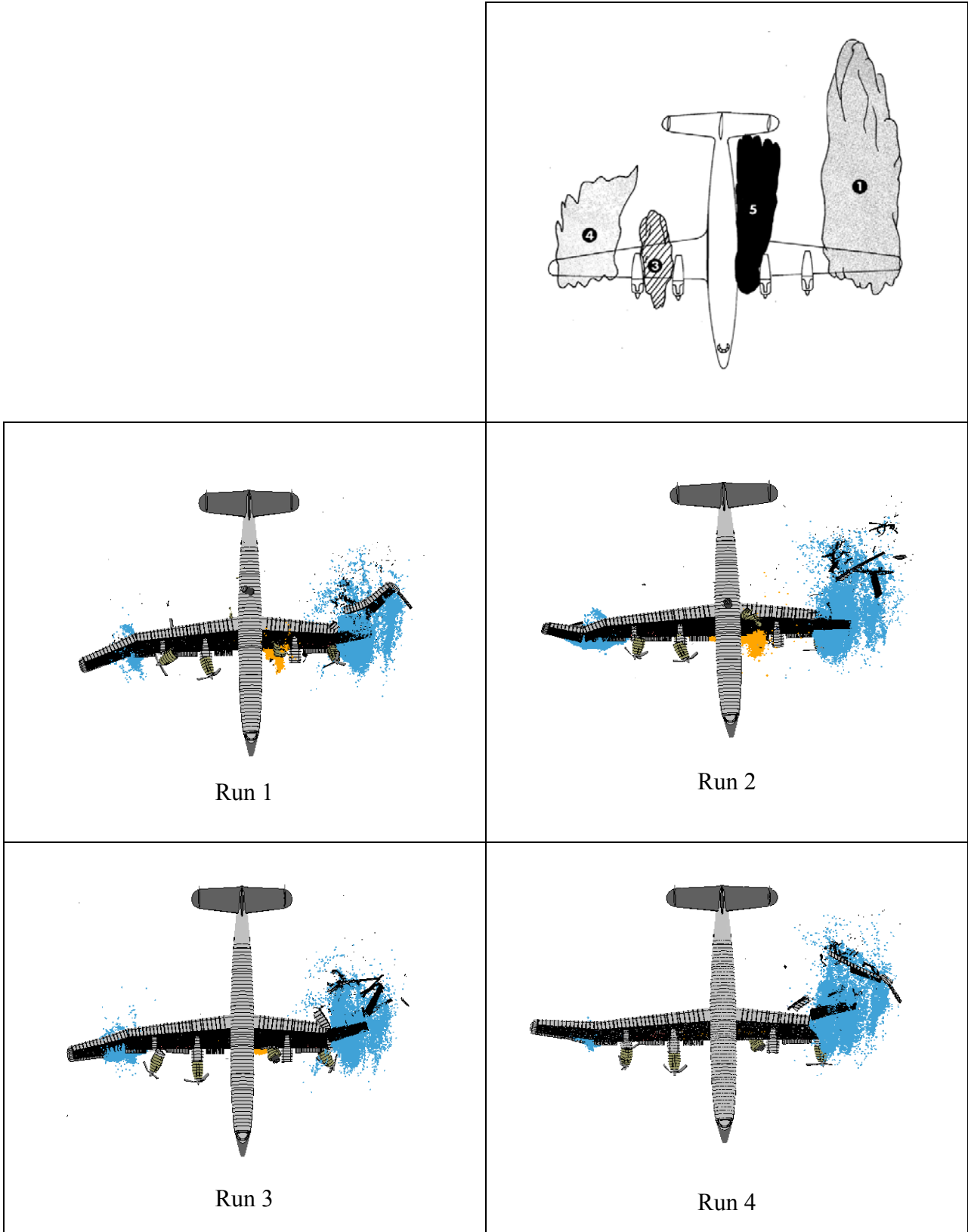
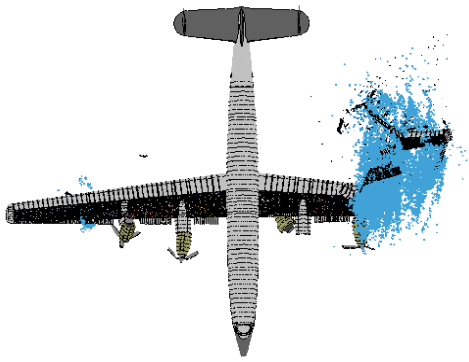
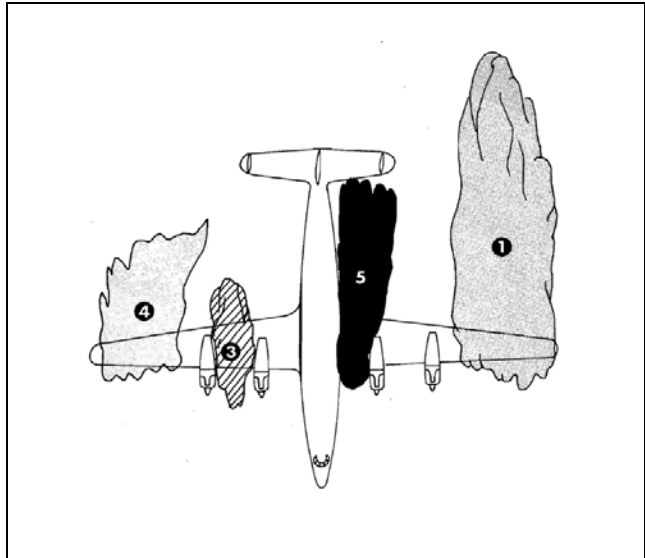
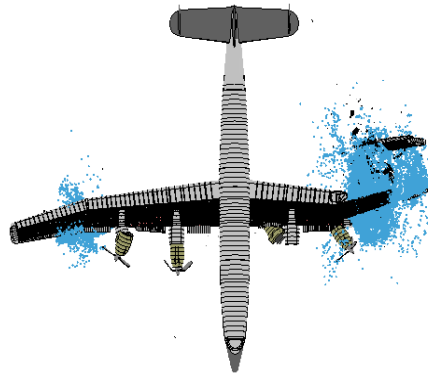


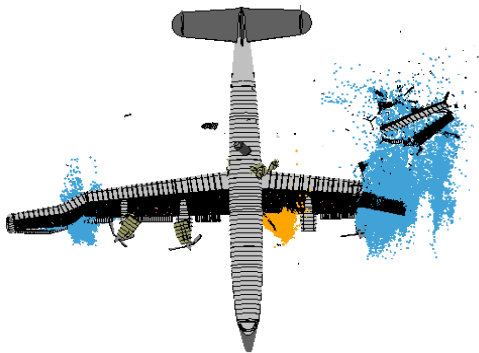
Figure 46. Fuel Spillage—Time = 1.39 s (Runs 1-4)



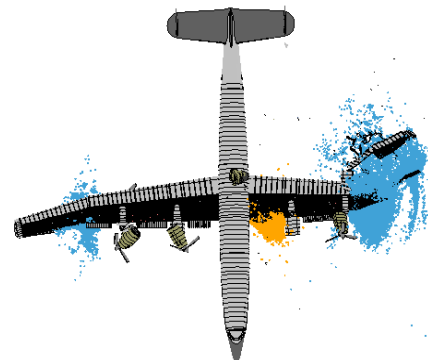
Run 5



Run 6



Run 7



Run 8

Figure 47. Fuel Spillage—Time = 1.39 s (Runs 5-8)

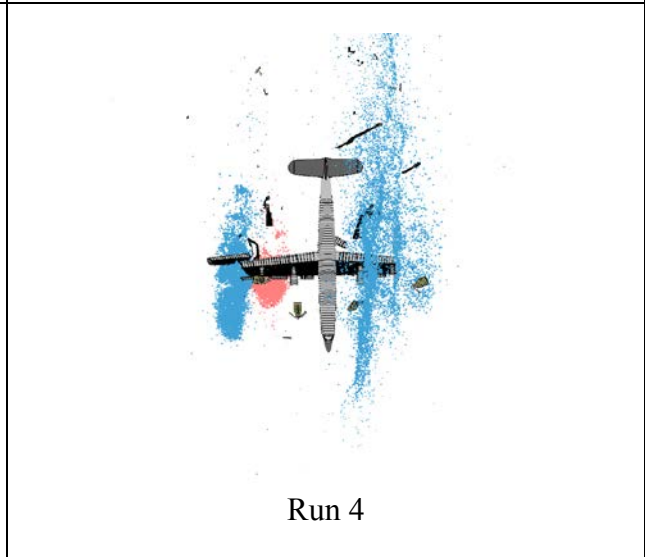
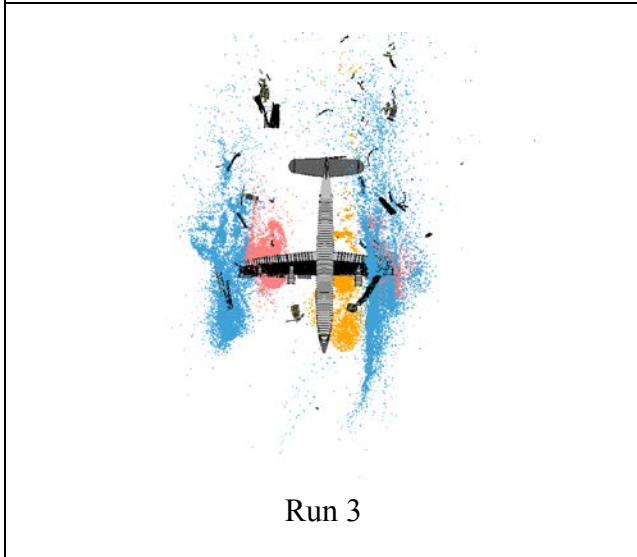
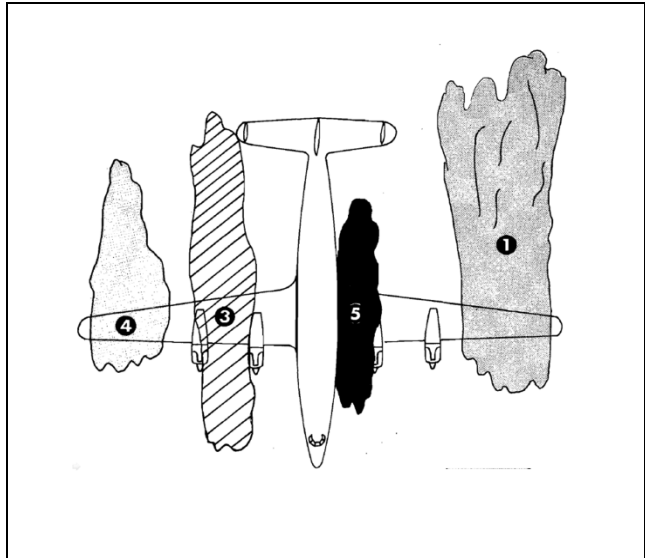


Figure 48. Fuel Spillage—Time = 2.49 s (Runs 1-4)



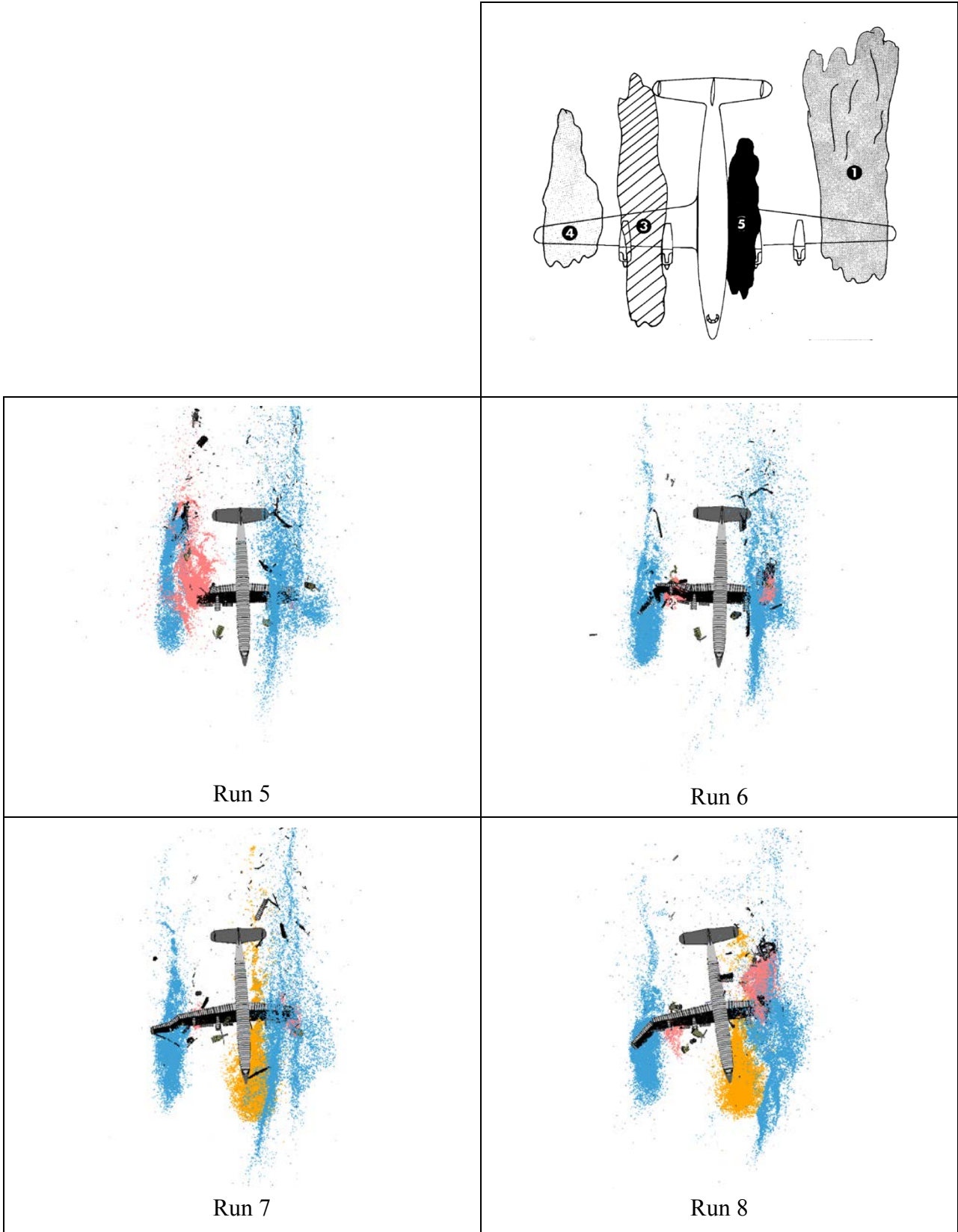


Figure 49. Fuel Spillage—Time = 2.49 s (Runs 5-8)

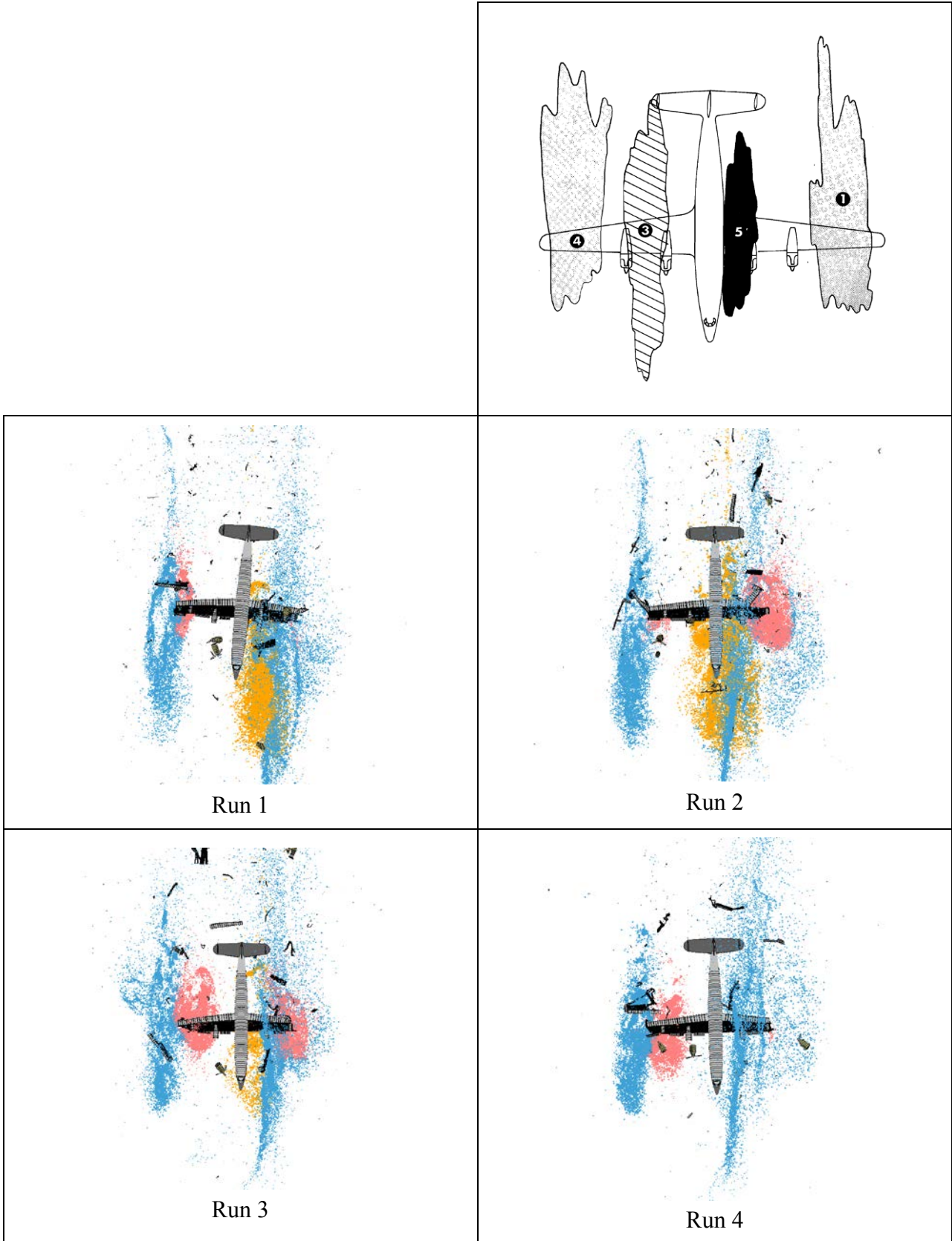


Figure 50. Fuel Spillage—Time = 2.90 s (Runs 1-4)

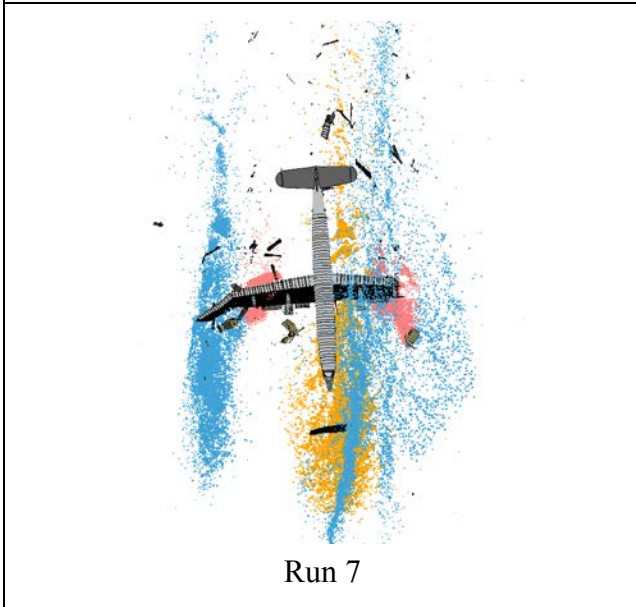
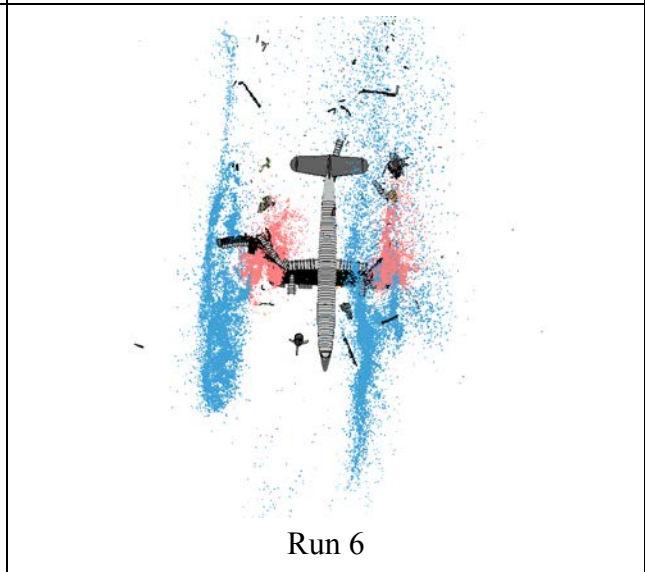
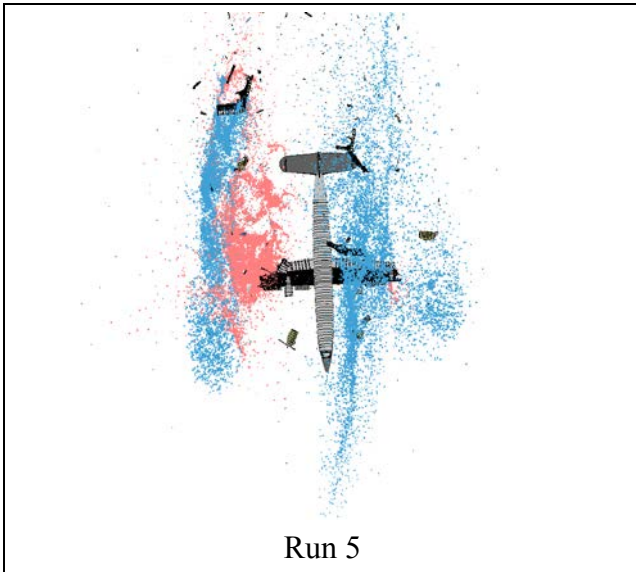
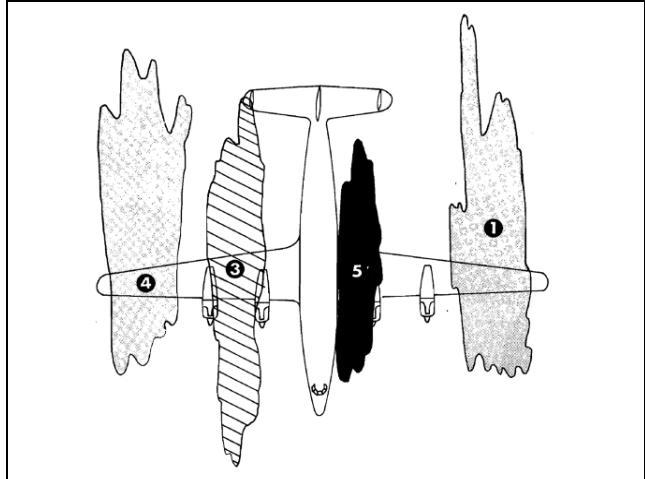


Figure 51. Fuel Spillage—Time = 2.90 s (Runs 5-8)

### 5.3 STRUCTURAL DAMAGE.

Figures 52 and 53 show the L-1649 wreckage in its final resting place on the 20° slope. All four engines detached from the wing. The left (port) wing was detached at the root, showing the compromised fore and aft spars. The wing was also broken off just outboard of the outboard engine nacelle. There appears to be a wing section extending out further than this, but it is actually just a wing fragment in that location.



Figure 52. The L-1649 Wreckage (aerial view) [5]

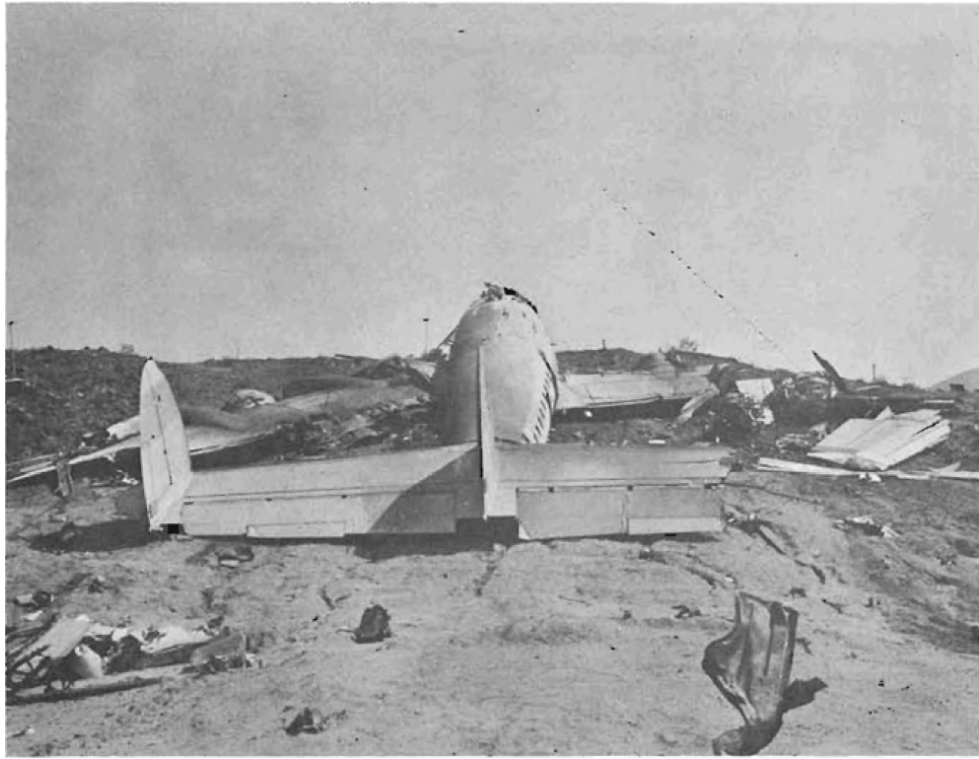


Figure 53. The L-1649 Wreckage (rear view) [5]

Tables 9 and 10 show the simulated damage to the left wing at the time the aircraft came to rest in the simulation. Keeping in mind that the impact conditions with the 20° slope were significantly different for half the runs, the similarities are quite good. For various runs, the wing was broken off at the root, as in the wreckage. This only occurred in the simulations when the inboard engine impacted the wing catastrophically. The portion of the wing outboard of the outboard engine nacelle was similarly completely removed. In some runs, the wing was compromised between the two engine nacelles, which was inconsistent with the test. However, this only occurred again from a large engine impact to the wing between the engines.

The right (starboard) wing in the wreckage was still attached at the root, but was compromised roughly halfway between the engine nacelles. A wing portion outboard of the impact point with telephone pole 1 appeared to be largely intact. Simulated damage to the right wing is shown in tables 11 and 12. In all runs, the wing root remained attached to the fuselage, albeit with varying levels of damage. The wing was also completely compromised or severely damaged between the two engine nacelles. Most runs also had a severed outboard wing segment with varying levels of damage.



Table 9. Damage to Left (port) Wing—Runs 1-4

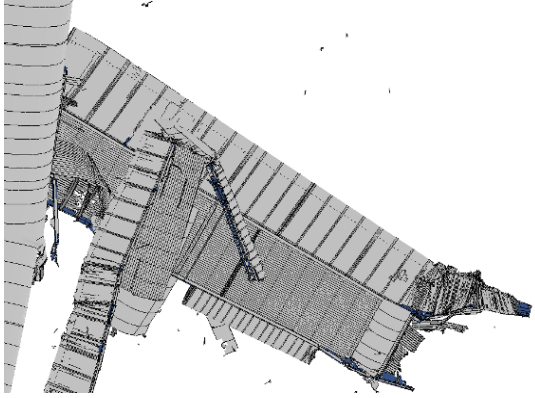
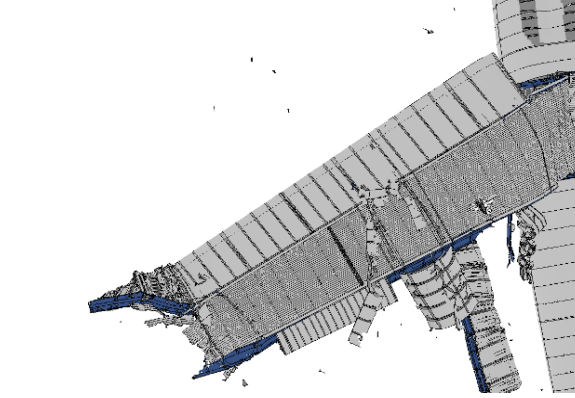
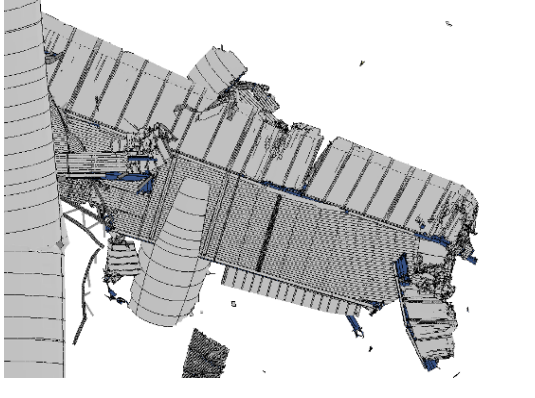
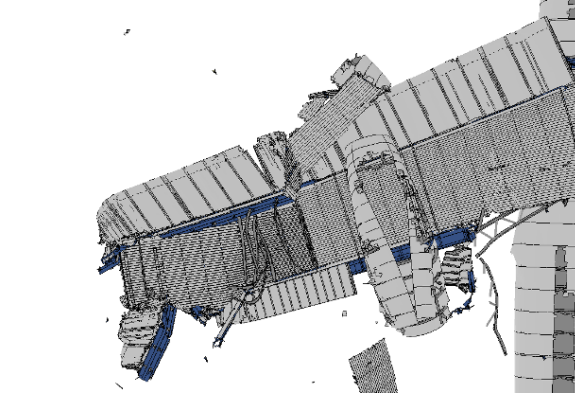
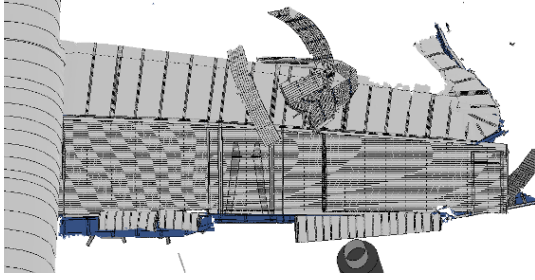
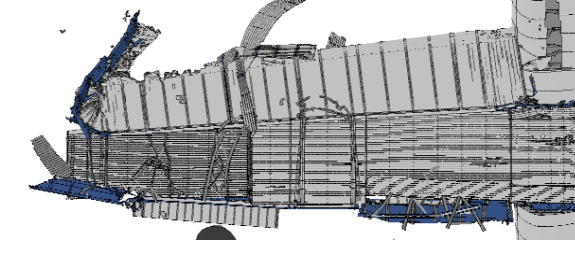
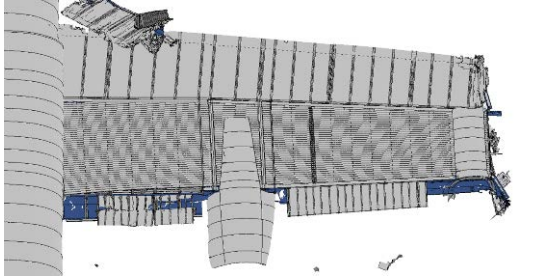
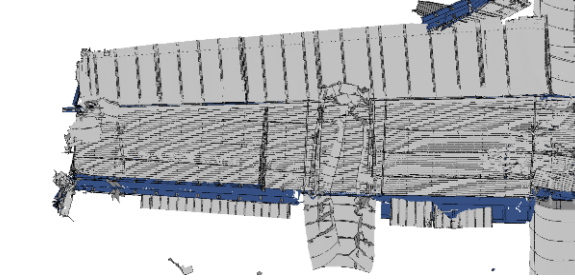
Run	Top	Bottom
1	 A top-down perspective view of the left wing showing initial damage. The leading edge is jagged and broken, with some internal structure exposed. The wing is oriented diagonally from the top-left towards the bottom-right.	 A bottom-up perspective view of the left wing showing initial damage. The underside of the wing is visible, with significant tearing and loss of material at the leading edge.
2	 A top-down perspective view of the left wing showing more extensive damage than Run 1. The leading edge is severely fragmented, and more of the internal structure is visible.	 A bottom-up perspective view of the left wing showing more extensive damage than Run 1. The underside shows significant structural failure and debris.
3	 A top-down perspective view of the left wing showing severe damage. Large sections of the leading edge and upper surface are missing or severely deformed.	 A bottom-up perspective view of the left wing showing severe damage. The underside is heavily damaged, with large areas of missing material and exposed internal structure.
4	 A top-down perspective view of the left wing showing the most severe damage. The wing is largely destroyed, with only a few fragments remaining.	 A bottom-up perspective view of the left wing showing the most severe damage. The wing is almost entirely destroyed, with minimal structure left.

Table 10. Damage to Left (port) Wing—Runs 5-8

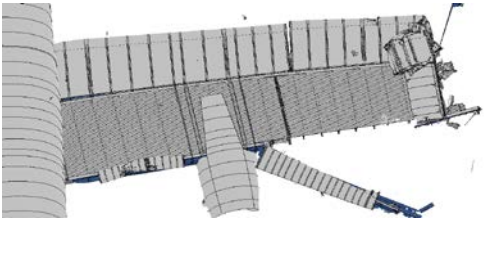
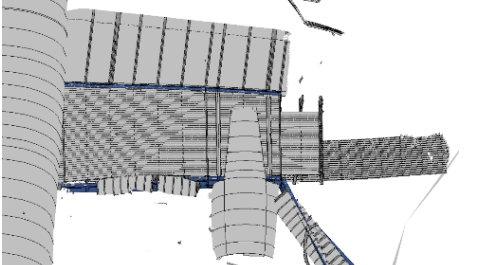
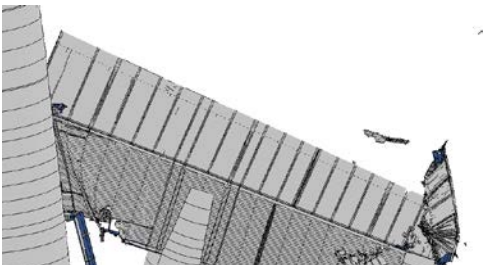
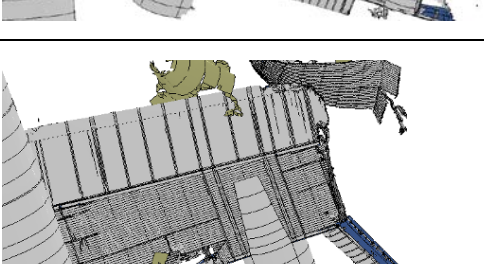
Run	Top	Bottom	
5	 A top-down perspective view of the left wing showing significant damage to the leading edge and upper surface. The wing is oriented horizontally, and the damage is concentrated towards the tip and the root area.		
6	 A top-down perspective view of the left wing showing damage to the upper surface and leading edge. The wing is oriented horizontally, and the damage is more extensive than in Run 5.		
7	 A top-down perspective view of the left wing showing damage to the upper surface and leading edge. The wing is oriented horizontally, and the damage is more extensive than in Run 6.		
8	 A top-down perspective view of the left wing showing damage to the upper surface and leading edge. The wing is oriented horizontally, and the damage is more extensive than in Run 7. Some areas are highlighted in yellow.		

Table 11. Damage to Right (starboard) Wing—Runs 1-4

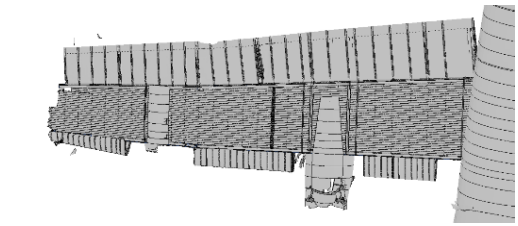
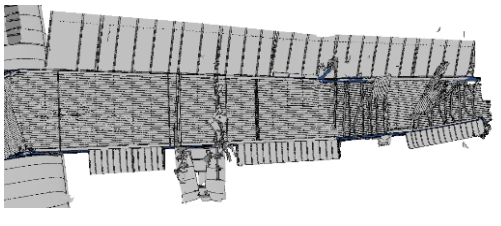
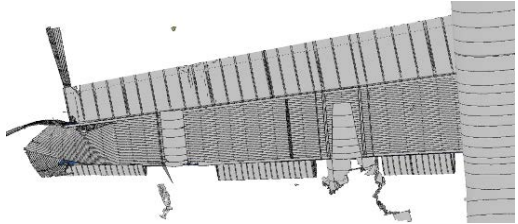
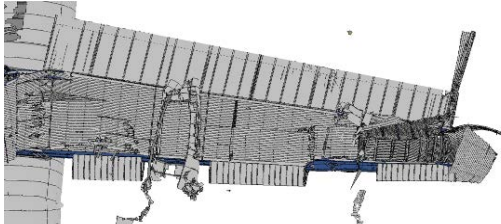
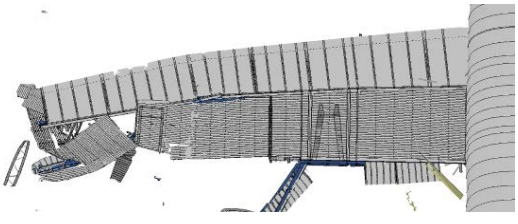
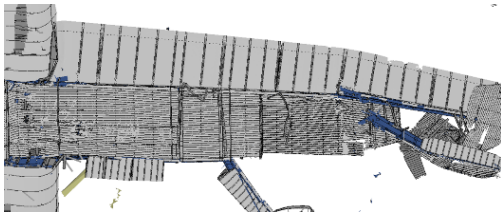
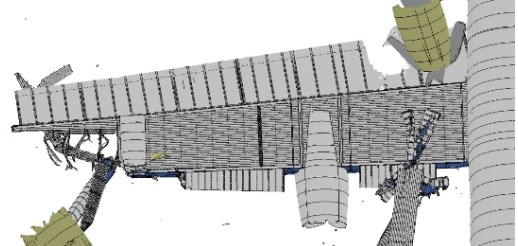
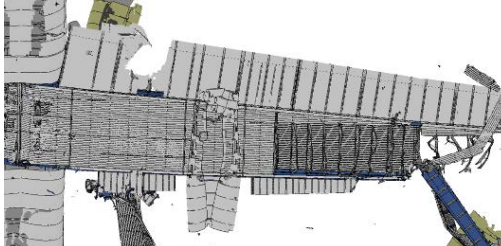
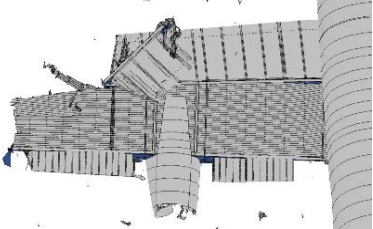
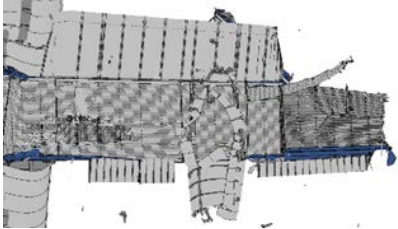
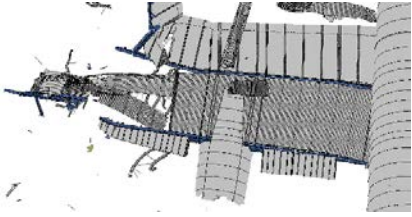
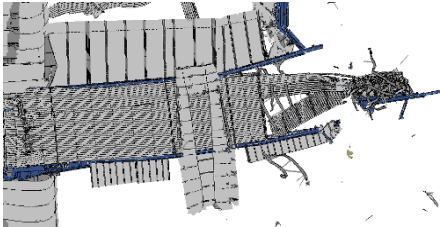
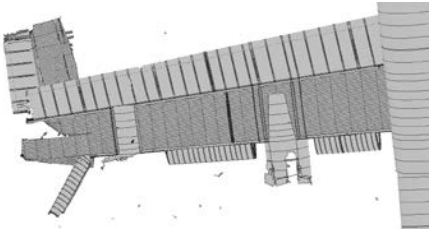
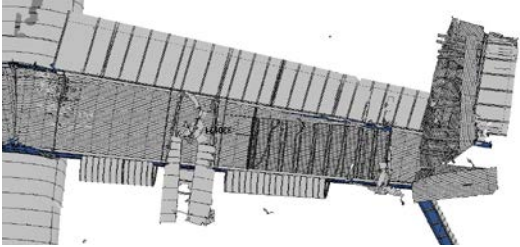
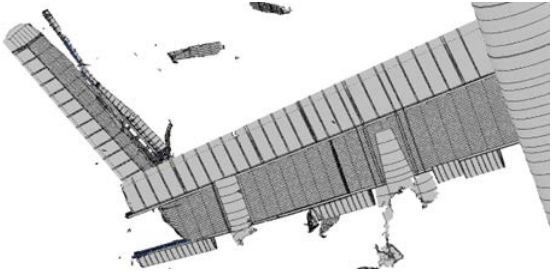
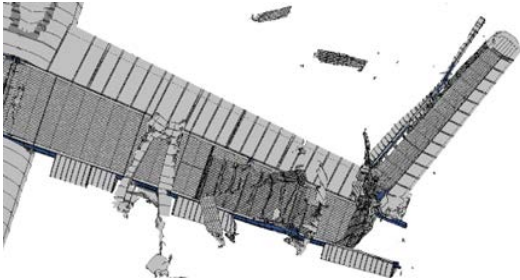
Run	Top	Bottom
1		
2		
3		
4		



Table 12. Damage to Right (starboard) Wing—Runs 5-8

Run	Top	Bottom
5		
6		
7		
8		

### 5.3.1 Liquid Release—Tank 1 (Outboard Port Tank).

The crash test report [5] describes the damage to Tank 1 as “The No. 1 fuel tank was ruptured when the outer portion of the left wing impacted against the earthen barrier. The complete destruction of the tank caused the entire volume of simulated fuel to be released in a heavy mist.”

The observed simulated behavior was consistent with the crash test for all runs, as shown in figures 35 through 51. Impact with the earth barrier completely overwhelmed the wing structure. A more detailed evaluation of the aircraft characteristics’ effect on this release of water was, therefore, not meaningful. A detailed evaluation was made, however, for all other tanks.

### 5.3.2 Liquid Release—Tank 2 (Mid-Wing Port Tank).

The crash test report [5] describes the damage to Tank 2 as “During the crash sequence, the No.2 fuel tank, which contained gelled water, was ruptured. The top aft-portion of the tank was torn and raised several inches in a 4- by 4-ft section and the bottom of the tank had cracked spanwise in several places. The gelled water was partially released during the crash and remainder of the liquid drained from the tank during two hours following the crash.”

No release of liquid was documented in the high-speed photography or in the fuel release sketches during the crash sequence. This damage may have occurred at the time the fuselage impacted the 20° slope. Since the simulated impact condition with the 20° slope was similar only for low-ground friction runs, it was difficult to make a comparison with simulated damage. Even for the low-friction runs, the extent of damage to the tank before impact with the 20° slope varied, depending on the damage from the engine impact. Therefore, a good comparison could not be made.

A review of the full-scale crash simulations revealed that the damage to Tank 2 was caused by a sequence of impact events. The first was typically some form of engine impact with the wing’s leading edge followed by nacelle impact with the 6° slope. The calculated damage from each of these events is described in table 13.

In Runs 6 and 8, the engine model impacts the wing catastrophically, completely releasing the liquid gel at approximately 2.28 and 1.8 s, respectively. Prior to this event and in all other runs, there are some differences in the way the engine impacts the wing, but in general, the damage was small or negligible. This appears to be an artifact of the crude modeling of the engines and is not realistic. Therefore, the fuel release evaluation after the engine impact was not meaningful. When the liquid was released, it was predominately from the bottom skin panel stripping off as the wing and nacelle impacted the 6° slope.

Table 13. Evolution of Damage to Tank 2

Run	Tank 2
1	<ul style="list-style-type: none"> <li>• Engine impact (1.25 s): Small damage to front spar top cap and web.</li> <li>• Nacelle impact with ground: Nacelle strips off on ground without much damage to bottom skin.</li> <li>• Nose at end 6° slope (2.49 s): Spanwise crack along top skin leading edge at outboard end tank over three ribs.</li> </ul>
2	<ul style="list-style-type: none"> <li>• Engine impact (1.25 s): Damage to front spar and creates spanwise crack at spar over two ribs. Leading-edge tank rib damaged.</li> <li>• Nacelle impact with ground (1.79s): Nacelle strips off on ground stripping away the bottom skin panel.</li> <li>• Nose at end 6° slope (2.49s): Underside skin panel almost completely compromised.</li> </ul>
3	<ul style="list-style-type: none"> <li>• Engine impact (1.40 s): Minor damage to front spar, web failed, caps intact.</li> <li>• Nacelle impact with ground (1.46 s): Nacelle strips off on ground, stripping away the bottom skin panel.</li> <li>• Nose at end 6° slope (2.25 s): Underside skin panel almost completely compromised.</li> </ul>
4	<ul style="list-style-type: none"> <li>• Engine impact (1.57 s): No apparent damage.</li> <li>• Nacelle impact with ground: Nacelle does not strip away bottom skin panel.</li> <li>• Nose at end 6° slope (2.26 s): Small crack in bottom skin at front spar at outboard edge of tank.</li> </ul>
5	<ul style="list-style-type: none"> <li>• Engine impact (1.48 s): Some damage to front spar. Hole in web between two ribs. Top cap cracked. Small release of gelled water.</li> <li>• Nacelle impact with ground (1.49 s): Spanwise crack over three ribs on bottom skin panel.</li> <li>• Nose at end 6° slope (2.24 s): Top skin cracked spanwise along front spar over three ribs. Bottom skin cracked spanwise mid-chord over three ribs.</li> </ul>
6	<ul style="list-style-type: none"> <li>• Engine impact (1.64 s): Small damage to front spar web.</li> <li>• Nacelle impact with ground (1.40 s): No damage.</li> <li>• Engine impact (2.28 s): Completely fails Tank 2.</li> <li>• Nose at end 6° slope (2.28 s): Tank 2 in process of second engine impact.</li> </ul>
7	<ul style="list-style-type: none"> <li>• Engine impact (1.64 s): No apparent damage.</li> <li>• Nacelle impact with ground (1.41 s): Nacelle strips off on ground, stripping away a significant portion of the bottom skin panel.</li> <li>• Nose at end 6° slope (2.48 s): Bottom skin split spanwise over all but two ribs, 0.48-m aft of front spar.</li> </ul>
8	<ul style="list-style-type: none"> <li>• Engine impact (1.84 s): Wing removed outboard of last two ribs of Tank 2.</li> <li>• Nacelle impact with ground (1.42 s): None</li> <li>• Nose at end 6° slope (2.57 s): Wing removed outboard of last two ribs of Tank 2.</li> </ul>

To evaluate the relative effect of the various characteristics of the aircraft structure and impact conditions, a main effects plot was generated for the liquid released from Tank 2 at 1.79 s, as shown in figure 54. This time was selected because it preceded the catastrophic engine impact at 1.84 s in Run 8 so the release would not be affected by this unrealistic response. The strength and ductility of the connections have the largest effect on the gelled water release. As would be expected, the quantity of liquid released decreased as the strength and ductility were increased. The impact conditions and ground friction had a negligible effect on the liquid release, and material yield stress and strength had a small effect.

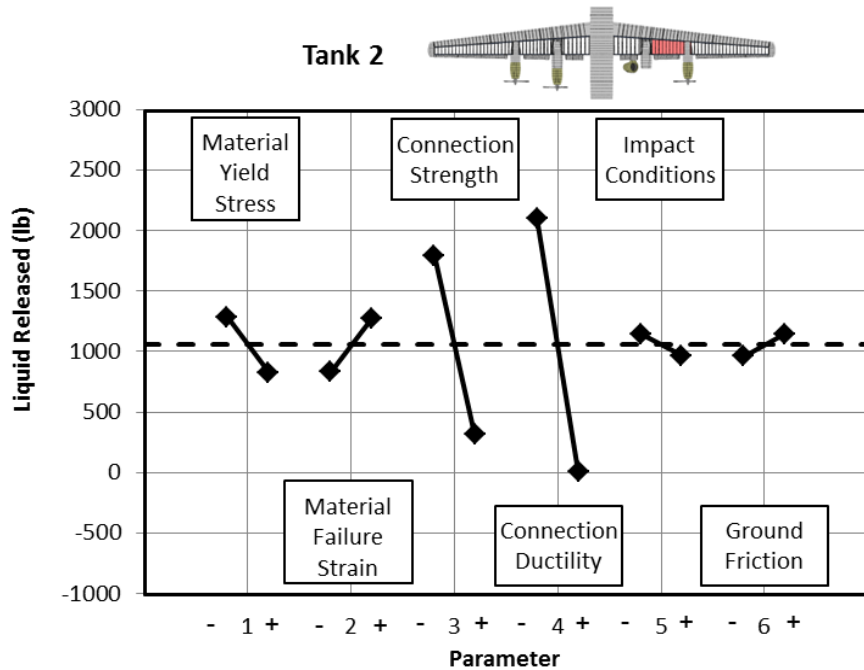


Figure 54. Main Effects Plot—Tank 2 Liquid Release at 1.79 s

### 5.3.3 Liquid Release—Tank 5 (Inboard Port Tank).

The crash test report [5] describes the damage to Tank 5 as “At impact, both main landing gears were broken off. The left gear pulled the No. 2 engine nacelle downward as it failed, causing that engine to roll under the left wing.”

“As the aircraft contacted and slid forward up the 6-degree slope, the wing was partially separated from the fuselage at the root. This failure opened up the No.5 fuel tank allowing its simulated fuel to be completely expelled in a mist cloud by the time the aircraft came to rest on the 20-degree slope. Traces of the simulated fuel were found 15 feet ahead of the aircraft.”

The report does not mention the engine impacting the wing at Tank 5. There was mention of it rolling under the wing, and the high-speed photography clearly shows this event occurring just as the nose of the aircraft first touches the 6° slope, as shown in figure 55.



Figure 55. Video Footage of Engine Impact With the Wing Leading Edge at Tank 5 (close up)

The main effects for liquid release in Tank 5 are shown in figure 56 at the time the aircraft nose reached the end of the 6° slope. The dominant effect was friction with the ground. The reason this parameter had such an effect was that, for the high-friction runs, the engine was propelled back towards the wing at a much higher relative speed. The front spar and, frequently, the top skin were completely compromised, and fuel was released rapidly. This does not occur in any low-friction runs. Since the actual engine impact conditions are unknown because the impact event was obscured by debris in the high-speed photography, this event could not be simulated with any less uncertainty. Therefore, no further information can be gained.

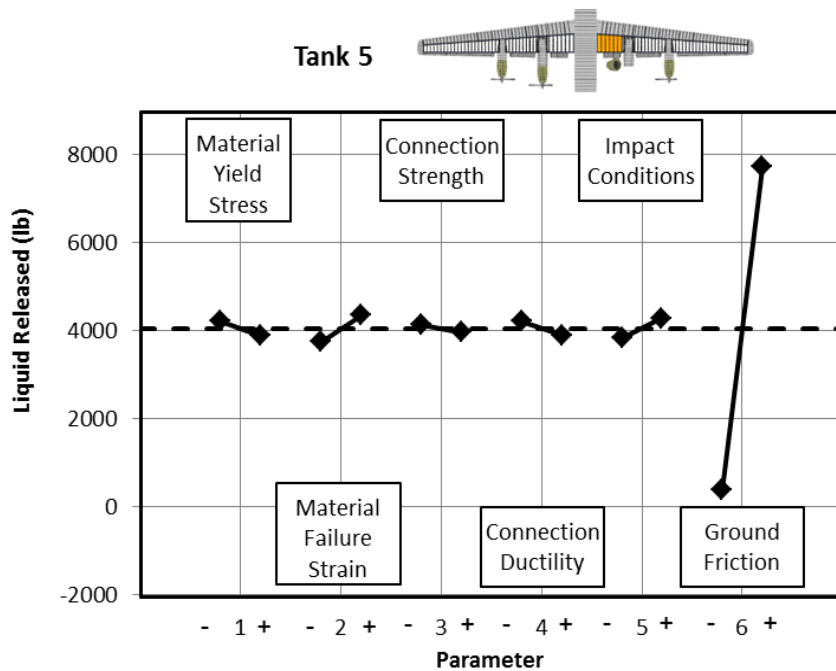


Figure 56. Main Effects Plot—Tank 5 Liquid Release at end of 6° Slope

#### 5.3.4 Liquid Release—Tank 6 (Inboard Starboard Tank).

The crash test report [5] describes the damage to Tank 6 as “The portion of the right wing inboard of the No. 3 engine nacelle remained attached to the fuselage throughout the crash. During the crash sequence, the simulated fuel was partially expelled from the fuel tank located in

this area through a split along the tank bottom just behind the forward spar. The remaining liquid drained from the tank within several minutes after the crash.”

Simulated damage to Tank 6 resulted in little or no release of water in all but Run 2, where the bottom skin panel split spanwise at the front spar. No water release was consistent with the high-speed photography. However the simulation showed a small release of liquid in runs 3 and 7 (less than 85 lbs.) via damage into tank 7, the empty center fuselage tank.

The main effects for liquid release in Tank 6 are shown in figure 57 at the time the aircraft nose reached the end of the 6° slope. Since only one run had any significant release of water outside the wing, this plot provides little information. However, if the water that was released into Tank 7 was considered, those main effects are shown in figure 58. The impact conditions and friction with the ground have a significant effect on the release of water from the tank, second to the connection ductility. It is noteworthy that the release of water was reduced as the strength and ductility of the connections were increased.

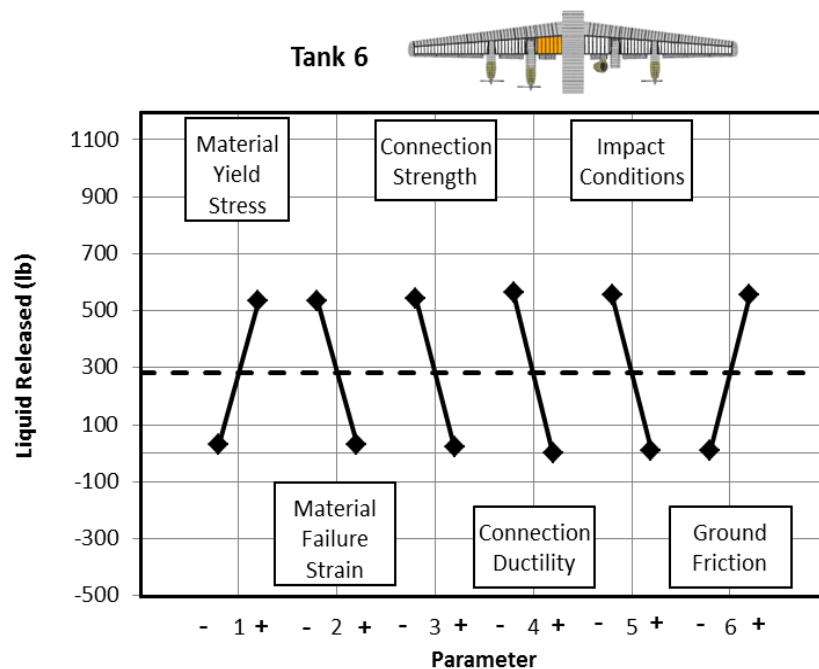


Figure 57. Main Effects Plot—Tank 6 Liquid Release at end of 6° Slope

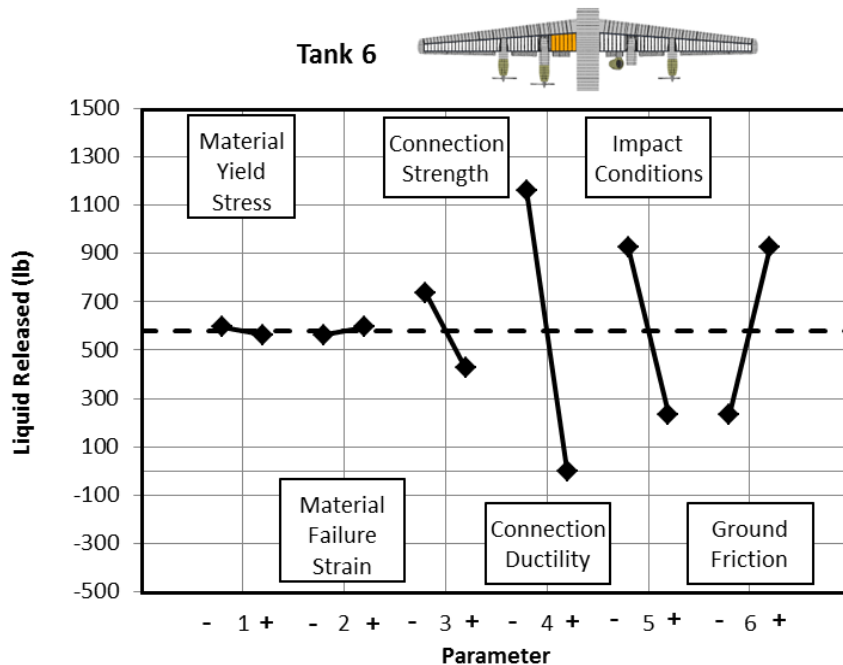


Figure 58. Main Effects Plot—Tank 6 Liquid Release at end of 6° Slope, Including Release Into Tank 7

### 5.3.5 Liquid Release—Tank 3 (Mid-Wing Starboard Tank).

The crash test report [5] describes the damage to Tank 3 as “The second pole cut into the wing and the No. 3 fuel tank between the No. 3 and 4 engine nacelles. The fuselage contacted the ground at approximately the same time and as it slid along this partially severed wing section, finally became separated, and came to rest upside down. The gelled water from the No. 3 fuel tank was released and streamed from the wing and had spread 23 feet ahead of the nose when the airplane came to rest.”

A review of the full-scale crash simulations revealed that the damage to Tank 3 was caused by a sequence of impact events. First, the engine nacelles impacting the ground followed by the inboard telephone pole, the nacelle impacting the 6° slope, and in some cases, impact from the outboard engine. Damage from each of these events is described in tables 14 and 15.

The main effects for liquid release in Tank 3 are shown in figure 59 at the time the aircraft nose reached the end of the 6° slope. In several runs, Runs 3-6 and 8, the impact of the engine with the front spar dominated the release of liquid from this tank. In the other runs, there was either a small amount of damage or no impact at all. Because the impact conditions on this tank were not consistent between runs, the main effects plot provides little meaningful information.

It is not clear from the high-speed photography or from the test report [5] whether there was a significant impact of the outboard engine with Tank 3. It is very possible, as the engine was tumbling in the high-speed photography ahead of the wing, see figures 36 and 37, but it quickly became shielded from view in a cloud of debris, see figure 38. The gelled water’s initial release was caused by some combination of the telephone pole impact and/or the engine nacelle and

wing with the ground. The red fluid is visible in the high-speed photography at the same time the engine is visible but not impacting the wing. This release was consistent with the results of many of the simulations performed prior to engine impact.

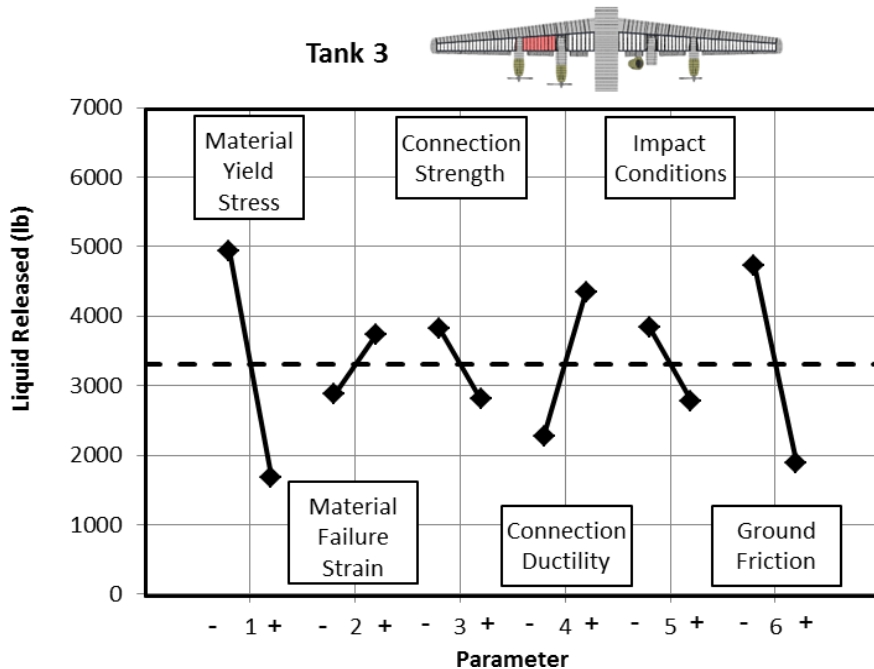


Figure 59. Main Effects Plot—Tank 3 Liquid Release at end of 6° Slope

An engine impact was also consistent with the degree of reported damage to the wing, as shown in figure 52 in which the wing outboard of the inboard engine nacelle is completely failed. Simulated results also show this type of damage for runs in which there was significant engine impact with the wing, as shown in tables 9 and 10.

Figure 60 shows the simulated damage to the front spar shortly after impact with the inboard telephone pole. Note that there is a crack in the front spar in Runs 3, 5, 6, 7, and 8. Although such a crack would certainly release a small amount of liquid, consistent with the crash test, none is observed in the images because the crack size is too small to release the larger fluid particles used in the model. In no case is the spar severely damaged. And, as detailed in tables 14 and 15, there is no significant damage to the internal structures from the telephone pole impact. This result is consistent with that observed in the high-speed photography in which no liquid release is observed during the telephone pole impact, but it is observed once the wing hits the ground.

It is noteworthy that the runs in figure 60 that display spar damage are not the same set of runs with the lower bound for the strength of the telephone pole (Runs 2, 4, 5, and 7). This shows that the damage to the spar is significantly affected by more than just the telephone pole strength. Likewise, these runs are not the set for the lower bound on material strength or ductility. There is clearly a combination of factors affecting this result that may be compounded by varied damage to the internal structures that develops during the nacelle impact with the ground, which



occurs prior to the telephone pole impact. These effects on release of liquid cannot be quantified because of the overwhelming effect of the engine impact in many runs.

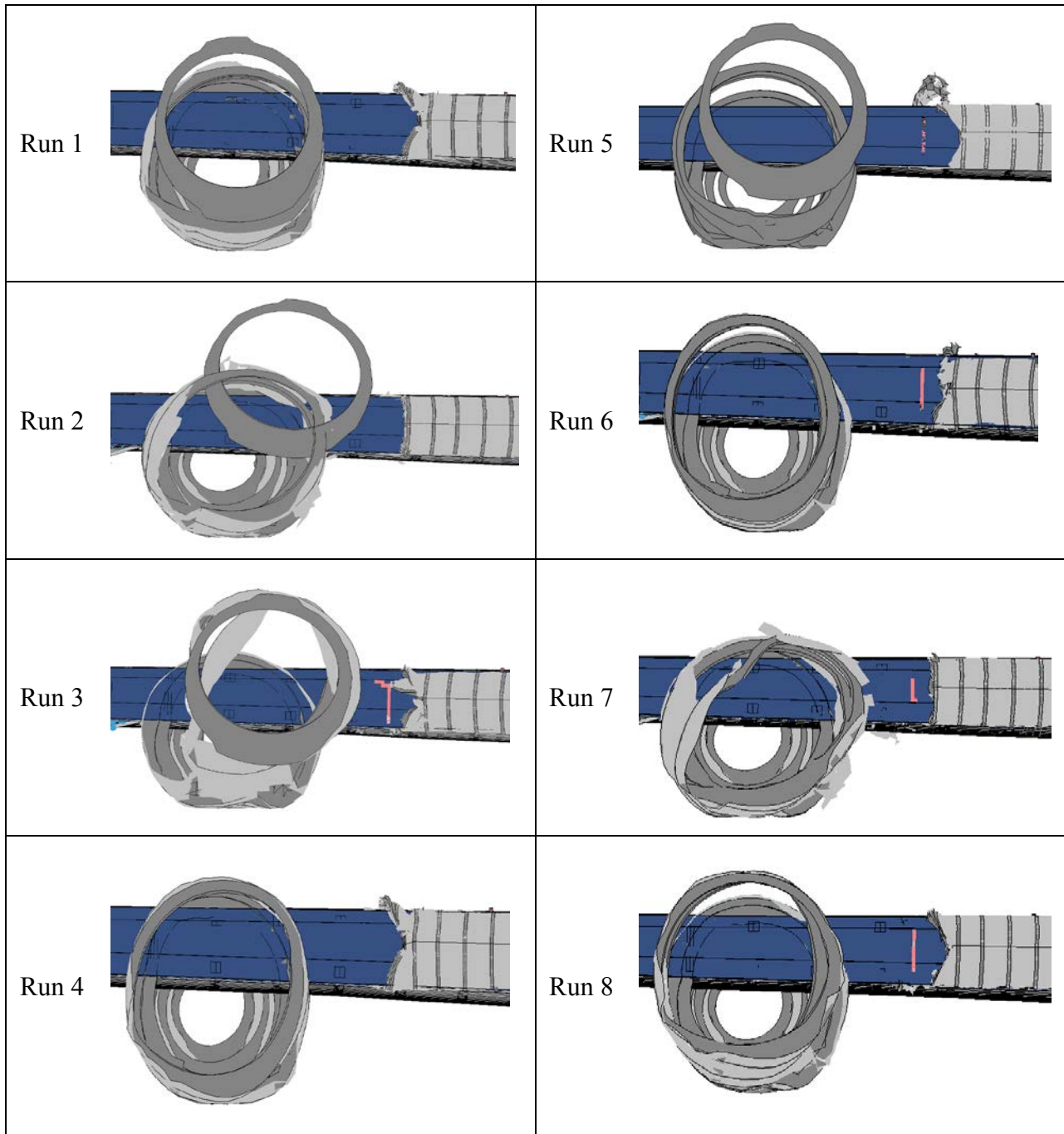


Figure 60. Simulated Damage From Inboard Telephone Pole Impact—Time = 1.250 s (view of wing leading edge with engine removed from view)

Table 14. Evolution of Damage to Tank 3—Runs 1-4

Run	Time (s)	Damage Evolution and Leakage
1	1.05 to 1.19	Nacelle impact with the ground: The truss rib-to-rear spar connection failed over four ribs.
	1.19	Inboard telephone pole impact: The center and bottom front spar webs failed and spread spanwise over 1 ft. There was some buckling of truss ribs at the impact point with the telephone pole, and a small number of tab-to-H-clip connections failed.
	1.43 to 2.49	Wing impact with 6° slope edge: The front spar failed. The bottom skin split chordwise along the 6° slope edge. The bottom panel split off outboard of the edge. The rear spar failed at 1.23 s.
	2.49	Nose at end of 6° slope: The bottom skin was removed from the outboard No. 4 tank. The front and back spars failed at the edge.
2	1.05 to 1.19	Nacelle impact with the ground: The truss rib-to-rear spar connection failed over four ribs. There was widespread truss rib tab detachment from the H-clips at the top and bottom skin panels. There was significant truss rib buckling. There was a failure or partial failure of the truss rib front spar connections.
	1.19	Inboard telephone pole impact: There were additional truss rib-to-rear spar connection failures. Note, the tab-to-H-clip connections already failed in the ribs at the impact point with telephone pole.
	1.30	Engine impact with the front spar: There was a small crack in the front spar web and skin at the cap. There was plastic buckling of truss ribs, and tab-to-H-clip connections failed at the impact point. Truss rib-to-front spar connections failed in the impact area.
	1.39 to 2.01	Nacelle impact with the 6° slope: The front spar crack spread spanwise about 8 in. Outboard tank rib web detached from the cap.
	2.02 to 2.49	Wing impact with the 6° slope edge: The front spar and bottom skin panels cracked chordwise. There was small damage to the bottom chord front spar.
	2.49	Nose at end of the 6° slope: There was small damage to the front spar. There was a large chordwise tear at the bottom skin, four ribs inboard of the tank end (as a result of the 6° slope impact). The outboard tank rib failed and leaked. Most of the leakage occurred up to 1.7 s and came from the compromised outboard tank rib and bottom skin panel.
3	1.05 to 1.19	Nacelle impact with the ground: Many truss rib tabs detached from the H-clips (less than in Run 2). Two truss connections failed.
	1.19	Inboard telephone pole impact: The spar web completely cracked vertically, propagating spanwise. Significantly more tab-to-H-clip connections failed and truss ribs buckled.
	1.47	Engine impact with front spar: The front spar completely failed. The engine went up under wing and removed the bottom skin panel. There was no leakage prior to this.
	2.25	Nose at end of the 6° slope: The bottom skin panel was removed at all but two inboard ribs. The front spar failed. The top skin split along the leading-edge spar.
4	1.05 to 1.19	Nacelle impact with the ground: There was no damage to the truss ribs or connections.
	1.19	Inboard telephone pole impact: Some small plastic buckling of truss ribs at telephone pole, small number of tab-to-H-clip connection partial failure. The spar did not fail.
	1.46 to 1.52	Nacelle impact with the 6° slope: Stripped the bottom skin panel spanwise along the front spar. The tab-to-H-clip connections failed. There was a little leakage at this point.
	1.52	Engine impact with the front spar: The spar completely failed.
	2.26	Nose at the end of the 6° slope: The bottom skin at the front spar split. The ground peeled back the bottom skin.

Table 15. Evolution of Damage to Tank 3—Runs 5-8

Run	Time (s)	Damage Evolution and Leakage
5	1.05 to 1.19	Nacelle impact with the ground: The truss rib-to-rear spar connection failed over four ribs.
	1.19	Inboard telephone pole impact: The center web of the front spar failed. There was some small plastic buckling of the truss ribs at the impact point with the telephone pole and partial failure of a small number of tab-to-H-clip connections.
	1.38	Engine impact with the front spar: The rear spars and the top wing panel completely failed. No leakage before this point.
	2.24	Nose at the end of the 6° slope: The bottom skin was removed, and the rear spar was gone over all but two inboard ribs.
6	1.05 to 1.19	Nacelle impact with the ground: The truss rib-to-rear spar connections failed over six ribs.
	1.19	Inboard telephone pole impact: The front spar center web and the bottom web partially failed. There was some small plastic buckling of truss ribs at the impact point with the telephone pole. The front 1/4 chord of the tab-to-H-clip connections failed on four ribs in the impact area.
	1.39 to 1.79	Nacelle impact with 6° slope: The bottom skin panel had widespread tab-to-H-clip connection failures.
	1.79 to 1.99	Engine impact with the front spar: This occurred just outboard of the Tank 3 tank rib, but the front spar completely failed and caused the bottom skin panel to separate along the front spar over five ribs in Tank 3. The outboard tank rib connection failed along the bottom skin. There was no leakage before this event.
	2.25	Nose at the end of the 6° slope: The outboard tank rib failed and the top, and the bottom skins cracked at the front spar.
7	1.05 to 1.19	Nacelle impact with the ground: The truss rib-to-bottom front spar connection failed at one rib, and there were widespread tab-to-H-clip connection failures to the bottom skin panel. The truss rib-to-rear spar connections failed over four ribs.
	1.19	Inboard telephone pole impact: The front spar center web failed. There was some small plastic buckling of truss ribs at the impact point with the telephone pole, and a small number of additional tab-to-H-clip connections failed in the impact area.
	1.31	Engine impact with the front spar: There were small cracks at the top spar cap. There was no leakage.
	1.32 to 1.89	Nacelle impact with the 6° slope: The bottom skin panel had additional tab-to-H-clip connection failures. Nacelle stripping caused some chordwise cracking at the bottom skin. There was some leakage.
	1.89 to 2.48	Wing impact with the 6° slope edge: The bottom skin panel had some chordwise splitting at the 6° slope edge. The skin split spanwise, causing the panels to strip off.
	2.48	Nose at the end of the 6° slope: The ground impact caused the bottom skin panel to come off from the tank over all but two inboard ribs. A small split occurred, initially, from the propeller.
8	1.05 to 1.19	Nacelle impact with the ground: The truss rib-to-rear spar connection failed over four ribs.
	1.19	Inboard telephone pole impact: The front spar center web and the bottom web partially failed. There were some small plastic buckling of two truss ribs at the impact point with the telephone pole. A few top tab-to-H-clip connections failed at two ribs.
	1.39 to 2.64	Nacelle impact with the 6° slope: The bottom skin panel was stripped spanwise along the front spar over four ribs. There were tab-to-H-clip connection failures along the outboard three truss ribs, located three tabs in from the front.
	2.64	Engine impact with the front spar: The front spar failed at all but the top cap. The bottom skin panel stripped off at the outboard two ribs. The outboard tank rib cracked along the bottom skin cap.
	2.57	Nose at the end of the 6° slope: The top skin split along the front spar. The bottom skin split along the front spar and in two other places over the width of the tank.

### 5.3.6 Liquid Release—Tank 4 (Outboard Starboard Tank).

The crash test report [5] describes the damage to Tank 4 as “The right wing impacted the two telephone poles. The first telephone pole nearly sheared off the outer wing panel opening up to No. 4 fuel tank permitting the simulated fuel to stream from the tank for remainder of the crash sequence. During the periods of high deceleration, the fuel blossomed out ahead of the aircraft and spread 20 feet forward of the nose as it came to rest.”

Postcrash simulation analysis showed that damage to this tank occurred due to the initial impact of the outboard telephone pole followed by the inboard engine nacelle impacting the ground, the outboard nacelle impacting the ground a bit later, and then the fuselage riding up the 6° slope, causing the wing to flex downward and Tank 4 to impact the ground. Up to this point (approximately 1.3 s), this sequence is approximately the same for all runs and a good assessment of the main effects can be made. After this sequence in several runs, a severe engine impact drastically affects the response of Tank 4, similar to Tank 3.

Liquid release was measured at 1.10 s and 1.30 s, as shown in figure 61. At 1.10 s, the damage and water release was predominantly from the telephone pole impact. A top view of the wing damage and water release for each run is shown in figure 62 at 1.10s. At 1.30 s, the damage to the wing and subsequent water release was due to the flexing of the damaged wing. The main effects plots for liquid release in Tank 4 are shown in figures 63 and 64 at 1.10 s and 1.30 s, respectively. There are very different main effects shown.

At 1.10 s, the impact conditions are the most dominant parameter due primarily to loading from the wing impact with the outboard starboard telephone pole. The significant difference in potential wood strength had a larger effect than any aircraft characteristics. The ductility of the connections, however, had a similar effect showing a reduction in quantity released with more ductile connections. The failure strain of the materials had the third most significant effect.

At 1.30 s, shown in figure 64, the connection ductility has by far the most significant effect. Apparently, having more ductility in the wing where the connections do not fail greatly reduces the quantity released.

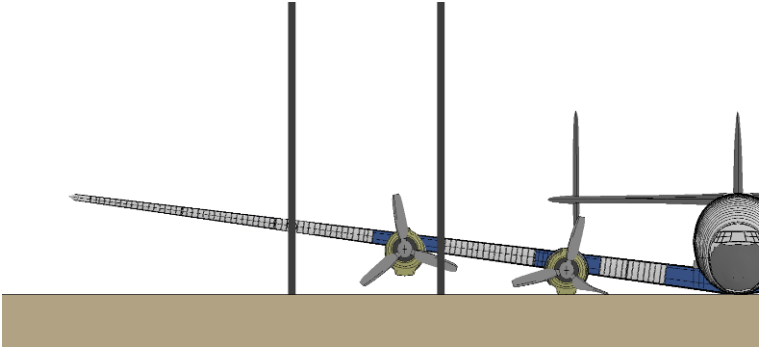
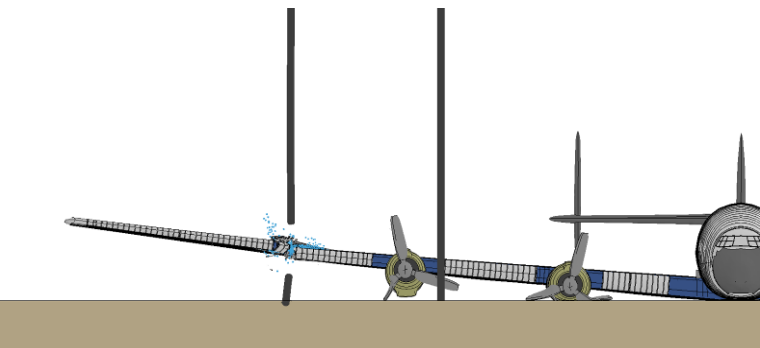
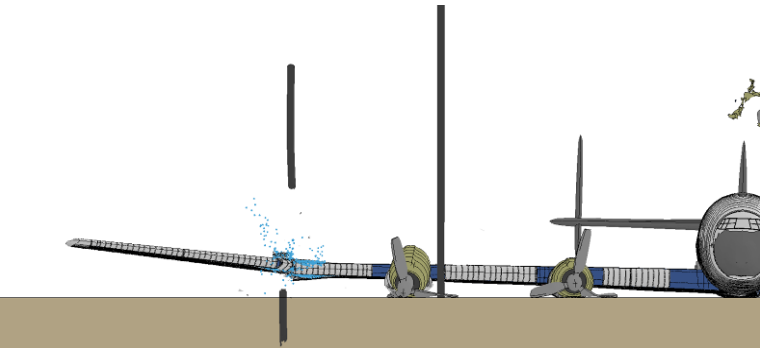
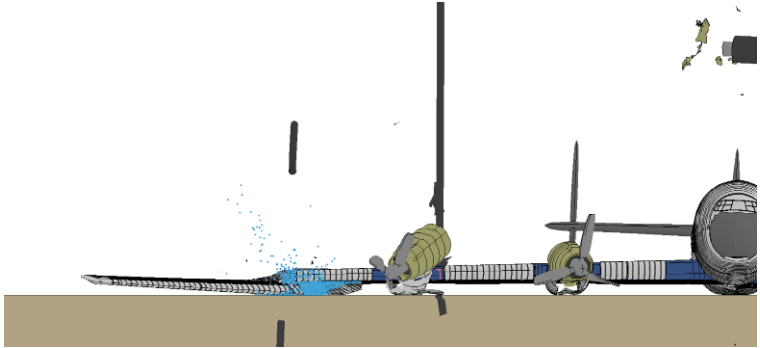
<p>1.00 s</p> <p>Just prior to telephone pole impact.</p>	
<p>1.10 s</p> <p>Telephone pole impacts Tank 4. Inboard nacelle impacts the ground. Fuselage nose begins to ride up the 6° slope.</p>	
<p>1.19 s</p> <p>Outboard nacelle impacts the ground. Fuselage rides up the 6° slope. Wing begins to flex downward.</p>	
<p>1.30 s</p> <p>Fuselage rides further up the 6° slope, lifting the wing. Wing flexes downward, causing Tank 4 to impact the ground.</p>	

Figure 61. Impact of Telephone Pole 1 With Tank 4 (Run 1)—  
the 6° Slope was Hidden From View

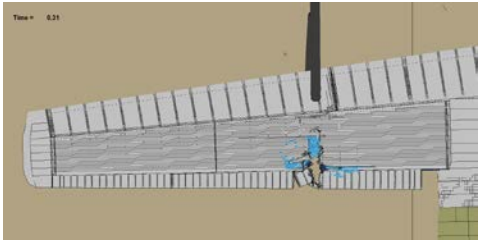
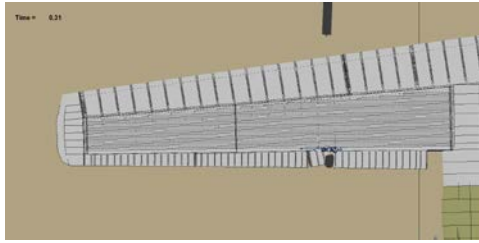
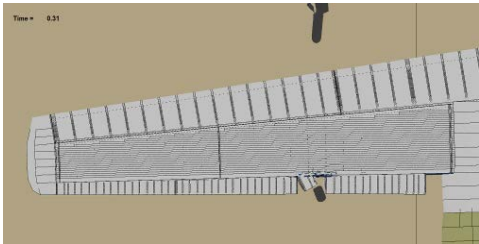
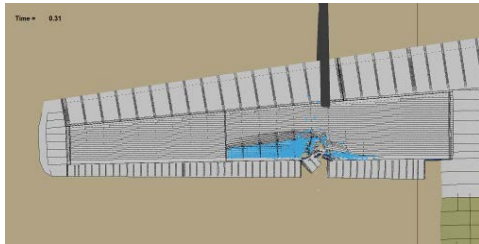
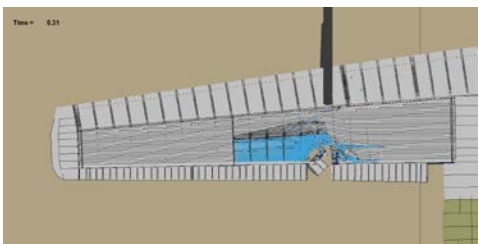
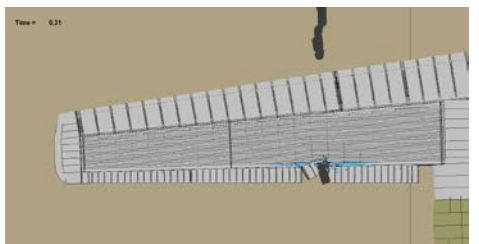
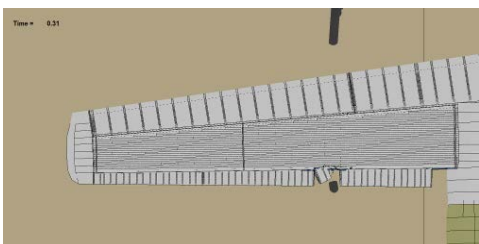
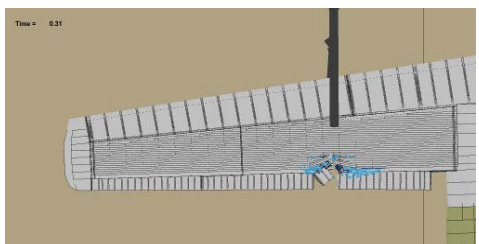
Run		Run	
1		5	
2		6	
3		7	
4		8	

Figure 62. Impact of Telephone Pole 1 With Tank 4 (top view) at 1.10 s

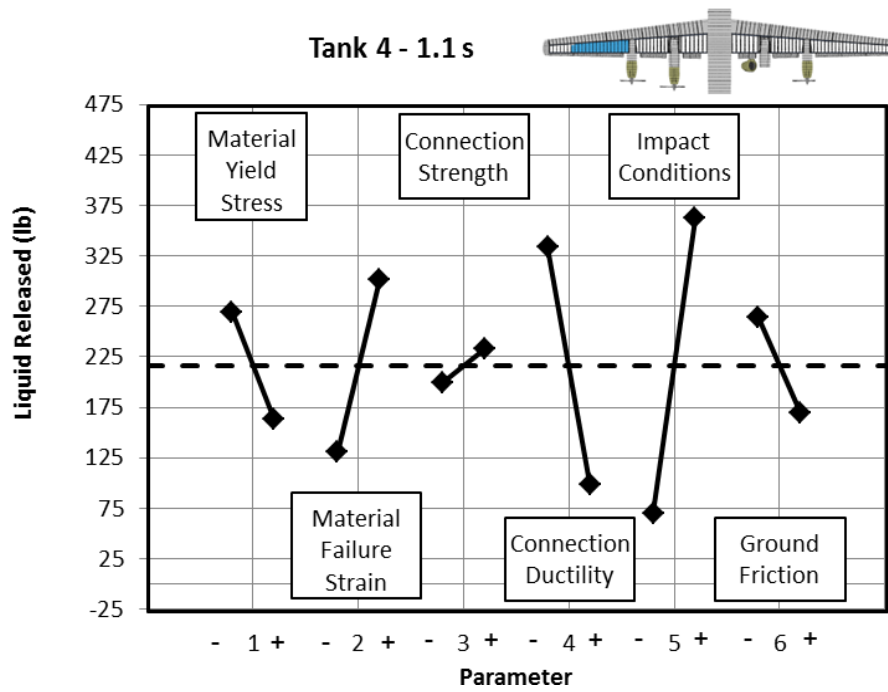


Figure 63. Main Effects Plot—Tank 4 at 1.10 s

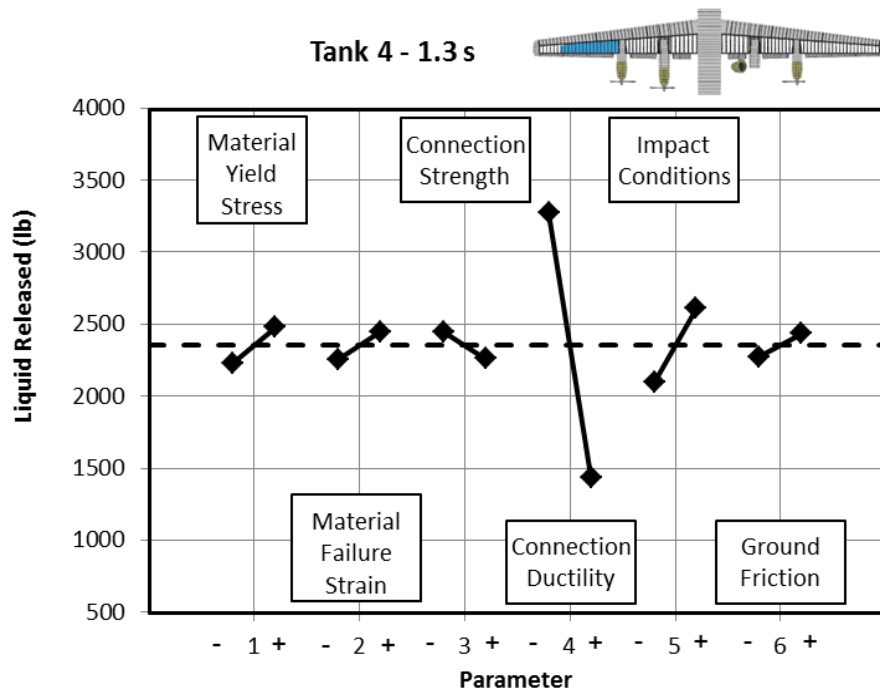


Figure 64. Main Effects Plot—Tank 4 at 1.30 s



## 6. SUMMARY.

The objective of the first phase of this research was to validate a modeling methodology to simulate full-scale transport aircraft crashes for predicting fuel release in survivable events. This was accomplished by comparing experimental and simulated full-scale crash events. This objective was met and significant insight into the important aspects of modeling these types of events was gained.

The range of simulated responses of the Lockheed Constellation Model L-1649 crash test in terms of overall aircraft motion, structural breakup of the wings, and release of liquid from the integral tanks bound the measured response from the crash test. The most significant variances appear to occur due to the unknown severity of various engine impacts with the wings. The simulated responses varied from no damage to complete destruction of the wing at the point of impact, depending on the relative velocity of the engine. This appears to be an artifact of the crude engine modeling and is not realistic. For this reason, high-fidelity engine models will be constructed for subsequent phases of the program when modeling modern transport aircraft crashes.

Another difference noted between the simulations and the crash test was that the simulated aircraft deceleration was slightly higher than the test, even for the lower bound for ground friction used. Interaction with the ground was important because the aircraft's deceleration affected the release of uncontained liquid from any compromised fuel tanks. Also, the engines' interaction with the ground had a large effect on how severe the engines' impact was on the wings.

The front view of the telephone pole impacts on the right wing showed an overall good agreement between the eight simulation runs and the video data. In the simulation, the liquid release appears to be visually smaller than in the high-speed photography due to the effect of aerosolization not included in the modeling.

In the side view of the telephone pole impacts, the telephone pole's bending and failure closely resembled the test footage just after impact. Best agreement was observed for the overall telephone pole deformation, failure, and kinematics for the runs with the higher bound for strength, indicating that the actual telephone pole strength was likely closer to the upper bound. The wing outboard kinematics of the telephone pole impact compared well during the impact event. The wing rotation and timing for when the wing tip impacted the ground varied by run after that.

The following summarizes the evolution of damage, release of liquid, and the main parameters that affect the liquid release from each tank shown in figure 65.

- Tank 1 (Outboard Port Tank): Impact with the soil barrier completely overwhelms the structure of Tank 1. A more detailed evaluation of the effect of the aircraft characteristics on this release of liquid is therefore not meaningful.

- Tank 2 (Mid-Wing Port Tank): Simulated damage to Tank 2 was caused by a sequence of impact events. The first was typically some form of engine impact with the wing leading edge followed by nacelle impact with the 6° slope. Damage from each of these events varied between runs, mostly due to the inconsistent severity of the engine impact, which in some cases, caused catastrophic wing failure and in others it imparted negligible damage.

Prior to the catastrophic engine impacts, however, the strength and ductility of the connections have the largest effect on release of the gelled water. As would be expected, the quantity of liquid released decreased as the strength and ductility increased. The impact conditions and ground friction had a negligible effect on liquid release and material yield stress and strength had a small effect.

- Tank 5 (Inboard Port Tank): Damage to this tank appears to have been dominated by a catastrophic impact of the inboard port engine with the wing. In the simulations, catastrophic impact occurred only with high ground friction. Since the actual engine impact conditions were unknown because the impact event was obscured by debris in the high-speed photography, this event could not be simulated with any less uncertainty. Therefore, no further understanding of liquid released from this tank was gained.
- Tank 6 (Inboard Starboard Tank): Simulated damage to Tank 6 was predominantly from impact with the ground. Dyed water was not visibly released during the crash test, but leaked out once the aircraft was stationary. Simulated results closely match this degree of damage with liquid released into the empty center wing tank in several runs and only released externally in one run. Uncertainty in the ductility of the connections had the greatest effect on this release of liquid. The severity of the impact conditions and friction with the ground were also significant.
- Tank 3 (Mid-Wing Starboard Tank): Simulated damage to Tank 3 was caused by a sequence of impact events. The first was the impact of the engine nacelles with the ground followed by impact of the inboard telephone pole, engine nacelle impact with the 6° slope, and in some runs, impact from the outboard engine. This complex sequence of impact events was further obscured by the inconsistent severity of the engine impact on the wing where it varied from no damage to catastrophic release of liquid from the tank. Because of this, quantitative evaluation of the main effects, unfortunately, provided little meaningful information for this tank.

In the test, initial release of the gelled water was caused by some combination of the telephone pole impact and the nacelle and wing impact with the ground. This release was consistent with the results of many of the simulations prior to engine impact. An engine impact was also consistent with the degree of damage reported to the wing.

It is worth noting that the runs that displayed spar damage are not the set of runs with exclusively the upper bound for the strength of the telephone pole. This shows that the damage to the spar was significantly affected by more than just the telephone pole strength. Likewise, these runs were not the runs for the lower bound on material strength

or ductility. There was clearly a combination of factors affecting this result that may be compounded by varied damage to the internal structures that develops during the nacelle impact with the ground, which occurred prior to the telephone pole impact.

- Tank 4 (Outboard Starboard Tank): Simulated damage to this tank occurred due to the initial impact of the outboard telephone pole followed by the inboard nacelle impacting the ground, the outboard nacelle impacting the ground a bit later, and then the fuselage riding up the 6° slope causing the wing to flex downward and Tank 4 to impact the ground. After this sequence in several runs, a severe engine impact completely compromised this tank. Prior to this event, this sequence was approximately the same for all runs and a good assessment of the main effects was made.

Liquid release was measured twice during the impact event: (1) water release predominantly from the telephone pole impact and (2) subsequent release due to the flexing of the damaged wing. There were very different main effects. Release of liquid from the telephone pole impact was most affected by the wood strength of the telephone pole. The ductility of the connections, however, had a similar effect showing a reduction in quantity released with more ductile connections. The failure strain of the materials had the third most significant effect. Later when there was flexing of the damaged wing, the connection ductility had by far the most significant effect.

- Refinement of modeling methods: Several key aspects of the aircraft model methodology were identified to improve the performance of the crash simulations to be performed for current transport aircraft and reduce the uncertainty in the results:
  - Modeling the ductility of connections in the wing structure is important to achieve a realistic response. The degree of ductility has a significant effect on liquid release for several fuel tanks in the L-1649 crash test. Reducing the uncertainty in this behavior will tighten the bounds on predicted fuel release.
  - Reducing the uncertainty in actual connection strength will tighten the bounds on predicted fuel release in subsequent phases.
  - Incorporation of structural embrittlement of the perforated plates from connections is essential in simulating realistic degrees of damage.
  - Interaction of the aircraft and its components with the ground needs to be carefully modeled for the crash scenarios selected in subsequent work. This will affect how severely aircraft components are stripped away from the wing, the severity of engine impact with the wing and the deceleration of the aircraft.
  - High-fidelity modeling of the engines is needed to achieve realistic impact response when hitting the wings and the ground.

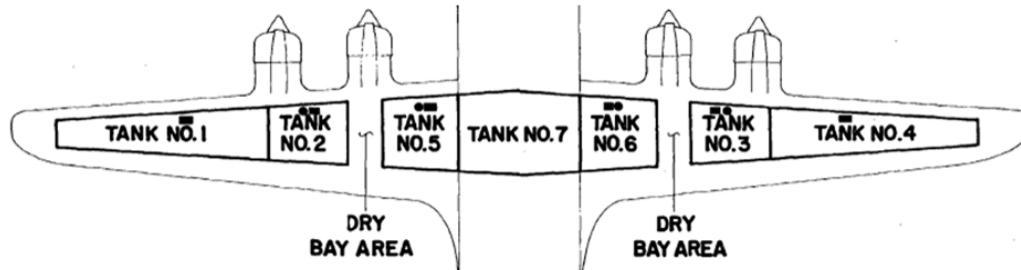


Figure 65. Wing Tank Diagram [5]

## 7. REFERENCES.

1. Hall, G.F., Partin, B.R., and Storm, J.H., "Large Frame Aircraft (LFA) Fire Fighting Validation: TCA/PCA Methodology Evaluation," Air Force Wright Laboratory Final Report WL-TR-95-3071, January 1995.
2. Kirkpatrick, S.W., Bocchieri, R.T., Sadek, F., MacNeill, R.A., Holmes, S., Peterson, B.D., Cilke, R.W., and Navarro, C., "Federal Building and Fire Safety Investigation of the World Trade Center Disaster: Analysis of Aircraft Impacts Into the World Trade Center Towers," NIST NCSTAR 1-2B, National Institute of Standards and Technology, Gaithersburg, MD, September 2005.
3. Dierdorf, D.S., "Performance-Based Standard for Firefighting Apparatus," *2005 Fire Suppression & Detection Research Application Symposium*, Orlando, FL, March 2005.
4. McDonald, M.J., Dierdorf, D.S., Kalberer, J., and Barrett, K.D., "Fire Extinguishing Effectiveness Tests," AFRL-ML-TY-TR-2004-4554, 2004.
5. Reed, W.H., Robertson, S.H., Weinberg, L.W.T., and Tyndall, L.H., "Full-Scale Dynamic Crash Test of a Lockheed Constellation Model 1649 Aircraft," FAA-ADS-38, October 1965.
6. Jones, L., Robertson, S.H., Johnson, N.B., Hall, D.S., and Rimson, I.J., "A Study of Transport Airplane Crash-Resistant Fuel Systems," FAA report DOT/FAA/AR-01/82, NASA/CR-2002-211437, March 2002.
7. Digimation Online Model Library, Lockheed Constellation Model MB27895, <http://www.digimation.com/home/ViewModel.aspx?c=MB27895>, date last visited 7/20/12.
8. "Structural Repair Manual for the Model 1649 Series Airplanes," Lockheed Report Number 11885, March 1, 1957, revised June 1, 1959.
9. Curtiss-Wright Corporation, Wright Aeronautical Division, Wright TC 18 EA Series Cutaway and Schematic Views, Woodridge NJ, Date Unknown, <http://www.aircraft-manuals.com/wrcy18.html>, date last visited 9/20/12.

10. Wright Aeronautical Corporation, Wright Cyclone Engines: Series 18 BA Installation Data, Part 855623, 1944, obtained via <http://www.aircraft-manuals.com/wrrcy18.html>, date last visited 7/20/12.
11. Roskam, J., "Airplane Design, Part V: Component Weight Estimation," Roskam Aviation and Engineering Corporation, Ottawa, KS, 1985.
12. "Department of Defense Handbook – Metallic Materials and Elements for Aerospace Vehicle Structures," MIL-HDBK-5J, January 31, 2003.
13. *Atlas of Stress-Strain Curves, 2<sup>nd</sup> Edition*, ASM International, Materials Park, OH, December 2002.
14. "LS-DYNA Keyword User's Manual" Livermore Software Technology Corporation, Version 971, May 2007.
15. Langrand, B., Deletombe, E., Markiewicz, E., and Drazetic, P., "Riveted Joint Modeling for Numerical Analysis of Airframe Crashworthiness," *Finite Elements in Analysis and Design*, 38, 2001.
16. Prevatali, F., Anghileri, M., Castelletti, L.-M.L., and Milanese, A., "Combined Numerical/Experimental Approach for Rivet Strength Assessment," *7<sup>th</sup> European LS-DYNA User's Conference*, Salzburg, Austria, May 14-15, 2009.
17. Kulak, G.L., Fisher, J.W., and Struik, J.H.A., *Guide to Design Criteria for Bolted and Riveted Joints, Second Edition*, American Institute of Steel Construction, Inc., John Wiley & Sons, Inc., Chicago, IL, 2001.
18. Gottlieb, R., "Test Data on the Shear Strength of Machine Countersunk-Riveted Joints Assembled by an NACA Flush-Riveting Procedure," National Advisory Committee for Aeronautics, 1942.
19. Fatemi, B.L.A., "An Experimental Investigation of Deformation and Fatigue Behavior of Coach Peel Riveted Joints," *International Journal of Fatigue*, 28, 2006, pp. 9-18.
20. Lemmen, P., Meijer, G., and Rasmussen, E.A., "Dynamic Behavior of Composite Ship Structures (DYCOSS) Failure Prediction Tool," TNO Report 2000-CMC-R0018, 2001.
21. "FAA/NASA International Symposium on Advanced Structural Integrity Methods for Airframe Durability and Damage Tolerance", NASA Conference Publication 3274 Part 1 and 2, Harris, C., ed., September 1994.
22. Chen, C., Wawrzynek, P.A., and Ingraffea, A.R., "Crack Growth Simulation and Residual Strength Prediction in Airplane Fuselages," NASA/CR-1999-209115, March 1999.

23. Ciliato, G.D. and Carneiro, S.H.S., "Analysis of the Residual Strength and Link-Up Stress of Aluminum Plates With Multi-Site Damage," 11<sup>th</sup> *International Conference on Fracture*, Turin, Italy, March 20-25, 2005, pp. 4691.
24. Harris, C., Newman, J.C., Jr., Piascik, R.S., and Starnes, J.H., Jr., "Analytical Methodology for Predicting the Onset of Widespread Fatigue Damage in Fuselage Structure," NASA Technical Memorandum 110293, November 1996.
25. Ingram, J.E., Kwon, Y., and Fawaz, S.A., *3D Finite Element Modeling of MSD-Cracked Structural Joints*, Netherlands: Delft University Press, 1997.
26. Patronelli, L., Lagrand, B., Deletombe, E., Markiewicz, E., and Drazetic, P., "Structural Embrittlement due to Riveted Joints – Evolution to a Macroscopic Model for Crash Analysis," *5th International Conference on Computational Structures Technology*, Louvain, Belgium, September 6-8, 2000.
27. Cherry, M.C. and Grandt, A.F., Jr., "Residual Strength of Unstiffened Aluminum Panels With Multiple Site Damage," *Engineering Fracture Mechanics*, Vol. 57, No. 6, 1997, pp. 701-713.
28. Murray, Y.D., "Manual for LS-DYNA Wood Material Model 143," Publication No. FHWA-HRT-0R-097, August 2007.
29. EngineersHandbook.com, date last visited 7/20/12.
30. Montgomery, D.C., *Design and Analysis of Experiments, 5th Edition*, John Wiley & Sons, Inc., 2001.